UNIVERSIDAD NACIONAL AUTÓNOMA DE MÉXICO

Programa de Posgrado en Astrofísica

Instituto de Radioastronomía y Astrofísica

THE EFFECT OF THE EXTENDED EMISSION AROUND Sgr A* ON THE PHASING EFFICIENCY OF ALMA DURING EHT OBSERVATIONS

Tesis para optar por el grado de
Maestro en Ciencias (Astrofísica)

Presenta:
Brissa Gómez Miller

Tutor:
Dr. Laurent Loinard
Instituto de Radioastronomía y Astrofísica

Morelia, Michoacán. Mayo, 2023

Agradecimientos

A mi madre, quien siempre me alentó a llegar tan lejos como yo quisiera y confió incondicionalmente en los sueños de su pequeña niña. Mi mejor guía de vida, y siempre la mejor.

Al Dr. Laurent Loinard y la Dra. Rosa Amelia González por su guía, paciencia y apoyo incondicional que me brindaron en lo académico y en lo personal durante todo el proceso. Especialmente al Dr. Laurent por confiar en mí y alentarme a dar todo de mi parte cuando sentía que ya no podía más, porque siempre me motivó, me ayudó a salir adelante y me devolvió la confianza en mí. Me abrió muchas puertas y su mentoría ha sido altamente significativa en mi formación. Nuevamente, gracias por confiar en mí y no soltarme.

A Karin Hollenberg, porque siempre me acompañó, estuvo conmigo dándome fuerzas y usaba las palabras correctas para mantenerme de pie. Ha sido mi confidente durante todo el posgrado, una gran amiga en la que siempre encuentro cobijo en sus palabras y que nunca me dejó caer.

A todos mis amigos y compañeros del posgrado de los que aprendí mucho, compartimos aventuras y me acompañaron durante todo el proceso, que nunca me soltaron. Especialmente a Janis, Sandino y Esmeralda.

A los docentes y toda la comunidad del IRyA.

A mi comité tutor y mi comité sinodal.

Al Consejo Nacional de Ciencia y Tecnología (CONACYT) y al proyecto IN112820 del Programa de Apoyo a Proyectos de Investigación e Innovación Tecnológica (PAPIIT) de la UNAM, por el apoyo económico otorgado durante la realización de esta tesis.

Resumen

Es casi universalmente aceptado que al centro de las galaxias más masivas se encuentra un agujero negro supermasivo (SMBH, por sus siglas en inglés, con M $\geq 10^6 M_\odot$) y que la fuente de energía de las galaxias de núcleo activo (AGNs) es debida a la acreción de materia por el SMBH. Los ambientes de los SMBH son realmente extremos, y cerca del horizonte de eventos (i.e. dentro de 10 veces el radio de Shwarzschild), los efectos de la relatividad general comienzan a volverse más evidentes (Ho, 2008). Es importante estudiar dichos ambientes extremos a escalas comparables con el radio de Schwarzschild, precisamente porque permiten poner a prueba la relatividad general en el régimen de campos fuertes. Sin embargo, incluso para los SMBHs más cercanos, obtener imágenes resueltas a la escala del horizonte de eventos requiere de instrumentación más especializada.

El Event Horizon Telescope (EHT) es una colaboración internacional que tiene el objetivo principal de capturar las primeras imágenes de SMBHs con una resolución angular suficiente para alcanzar escalas del horizonte de eventos. El EHT está conformado por un arreglo de telescopios distribuidos en diferentes partes del mundo, desde el Groenlandia hasta el Polo Sur, conectados por largas líneas de base que en conjunto simulan un telescopio virtual del tamaño del planeta Tierra. El principio con el que opera el EHT es una técnica de radioastronomía llamada interferometría de muy larga base (VLBI), con la cual observa a longitudes de onda submilimétricas alcanzando $\lambda = 1.3$ mm (230 GHz). Entre los telescopios que forman parte de este arreglo, se encuentran de un plato simple o interferómetros, como es el caso del Atacama Large Millimeter/submillimeter Array (ALMA). Durante la campaña de observaciones de 2017, el EHT observó diferentes fuentes de radio incluyendo dos SMBHs, uno localizado al centro de la galaxia M87 (M87*) y el otro al centro de la Vía Láctea (SgrA*) (Event Horizon Telescope Collaboration et al., 2019a).

Como se mencionó antes, algunas estaciones del EHT son interferómetros, por lo que tienen que operar como arreglos faseados (*phased array*), es decir, que el interferómetro opera como una estación de plato simple dentro de un interferómetro aún más grande. Un arreglo faseado consiste en la suma de todas las señales a la salida de cada antena que conforma el arreglo y se almacenan como si fueran de una sola antena. Este requiere de correciones en los retrasos de las señales que llegan a las antenas. ALMA es un interferómetro conformado por 66 antenas de diferentes tamaños; para este proyecto, ALMA opera con una configuración de antenas más compacta de ~ 37 antenas de 12 m en un arreglo faseado que incrementa la sensitividad de las observaciones. Observar con ALMA como un arreglo faseado implica realizar correcciones de fase a las antenas individuales relativas a una antena de referencia. Las señales faseadas se suman dentro del correlador de ALMA en donde las correcciones se aplican. Este arreglo faseado de ALMA resulta en una antena virtual de ~ 84 m (Goddi et al., 2019a). El ALMA Phasing Project (APP) fue un proyecto internacional para producir un sistema faseado para ALMA que permita incrementar el área de colección para aplicaciones de VLBI (Matthews et al., 2017a).

Un arreglo faseado ideal de N antenas o elementos es equivalente a tener una apertura de N veces el área colectiva de cada antena, pero en un arreglo faseado real existen algunas pérdidas en la eficiencia que decrece el área efectiva de colección. Esta eficiencia de faseo, η_p, se puede definir como el cociente de la correlación cruzada entre las señales sumadas y la antena de comparación, y la sección transversal promediada entre la antena de comparación y los elementos individuales faseados.

Para una eficiencia de faseo perfecta el valor de η_p es 1, y la amplitud correlacionada se espera que crezca como la raíz cuadrada del número de antenas usadas para construir la suma (Matthews et al., 2017a).

El objeto de estudio de este trabajo fue SgrA*, un objeto en radio que tiene una masa de $4 \times 10^6\ M_\odot$, que localizado a $\sim$ 8 kpc, es el candidato al agujero negro al Centro Galáctico. Observaciones con VLBI han revelado una fuente ultra compacta que presenta una variabilidad a escalas de tiempo corto, y complementado con observaciones a altas resoluciones se ha revelado la presencia de una estructura de emisión extendida alrededor del núcleo, conformada por gas ionizado y a la cual se le conoce como mini espiral. SgrA* puede ser estudiado a escalas de su radio de Schwarzschild con el VLBI. (Fish et al., 2011a) observaron esta fuente usando esta técnica con 1.3 mm y fueron capaces de obtener información de la fase de la fuente y la variabilidad en la densidad de flujo a escalas del radio de Schearszchild. Durante la campaña de observaciones de 2017 del EHT, ALMA observó durante varias noches SgrA*.

Existen estimaciones de la eficiencia de faseo de ALMA considerando que la SgrA* es una fuente puntual (i.e. no resuelta por ALMA). Sin embargo, como se mencionó anteriormente, tiene una componente de emisión extendida alrededor y esta componente no muestra variabilidad en el tiempo. La presencia de emisión extendida tiene un efecto sobre la eficiencia de faseo que no se ha tomado en cuenta para las estimaciones que se han hecho hasta ahora. Nuestra meta aquí es calcular el efecto que tiene la presencia de la mini espiral en Sgr A* sobre la eficiencia de faseo en ALMA. Gracias a la alta sensitividad de ALMA, con las observaciones obtenidas durante 2017 hice imágenes de alta resolución angular de la componente de emisión compacta de SgrA* para medir el flujo de la fuente en el tiempo, y con ello obtener las curvas de luz de 21.5 horas en promedio. También medir el efecto de la emisión extendida en la eficiencia de faseo de ALMA, utilizando la técnica de autocalibración para corregir las fases de las senales de la fuente.

Contents

List of Figures

Chapter 1

Introduction

It is almost universally accepted that a supermassive black hole (SMBH; with $M \geq 10^6$ $M_\odot$) resides at the center of most massive galaxies, and that the energy fueling the activity of active galactic nuclei (AGNs) is due to the accretion of matter onto a SBMH. The environments of SMBHs are truly extreme; for instance, close to the event horizon (i.e. within about 10 Schwarzschild radii), general relativistic strong-field effects, such as gravitational lensing and redshifts, are expected to become evident (e.g. Ho, 2008). Even for the nearest SMBHs, however, obtaining resolved images at event horizon scales requires the development of specialized instrumentation.

The Event Horizon Telescope (EHT) is an international consortium created in 2017 with the specific goal of capturing the first ever images of SMBHs with an angular resolution sufficient to access event horizon scales. It uses an array of distributed radio telescopes linked together to simulate a virtual Earth-sized telescope. The EHT operates using the radio astronomy technique known as very long baseline interferometry (VLBI), which pushes far into the millimeter/sub-millimeter regime – currently up to 1.3 mm (230 GHz), with the plan to reach 0.85 mm (345 GHz) in the future. At the moment, the EHT array includes telescopes distributed from Greenland to the South Pole, and from Hawaii to western Europe. Some of its elements are single dish telescopes, such as the Large Millimeter Telescope Alfonso Serrano (LMT) in Mexico, while others are interferometers, such as the Atacama Large Millimeter/submillimeter Array (ALMA) in Chile.

During its inaugural campaign of observations in April of 2017, the EHT observed a total of about half a dozen well-known SMBHs, but focused particularly on two targets. One is located at the center of the elliptical galaxy M 87 and is called M 87*, while the other is at the center of our Milky Way Galaxy (Sgr A*). These are the two known black holes with the largest Schartzschild radii as seen from the Earth, and the only two that can be observed at horizon scales with the EHT. The first results obtained from EHT observations were published by Event Horizon Telescope Collaboration et al. (2019a,b,c,d,e,f); they correspond to the first image of M 87* obtained at an angular resolution comparable with its event horizon. More recently, EHT images of M 87* in polarized light were also published (Event Horizon Telescope Collaboration et al., 2021a,b) and provided very valuable information on the magnetic field just outside of the event horizon. Finally, the first EHT images of Sgr A* were published earlier this year (Event Horizon Telescope Collaboration et al., 2022a,b,c,d,e,f). Together, these early EHT results provide a direct validation of general relativity (GR) in the strong field regime.

In this thesis, we will make use of observations of Sgr A* obtained with ALMA during the 2017 EHT campaign to characterize a specific aspect of the performance of ALMA as an EHT element. In this opening chapter, our aim is to present briefly the key concepts that will be useful for the rest of the manuscript. First, we will present in more details the EHT as a VLBI array. Second, we will explain how interferometers such as ALMA or the Sub-Millimeter Array (SMA) can be used as individual elements of a larger VLBI array, and present the required data handling (known as *array phasing*). Third, we will present the target of our study, Sgr A*. Finally, we will close the chapter by defining the exact goal of the thesis.

1.1 The Event Horizon Telescope

The EHT is a VLBI array that measures complex visibilities which, after proper calibration, can be Fourier-transformed into an image –i.e. a distribution of the brightness distribution on the sky. The angular resolution of a VLBI array is given by Equation (1.1), where θ is the angular resolution, λ is the observed wavelength and B is the maximum baseline length between the telescopes in the array (Thompson et al., 2017).

$$\theta = \frac{\lambda}{B}. \tag{1.1}$$

As any VLBI array, the EHT makes use of the technique called *aperture synthesis* (Thompson et al., 2017). From the perspective of the target source, and due to the diurnal rotation of the Earth, the antennas conforming the array appear to rotate on elliptical paths. After many hours, their changing positions slowly fill the aperture of an imaginary telescope with a size that corresponds to the area subtended by the array on Earth as seen from the target (See Figure 1.1). In the case of the EHT, the small number of antennas and the large separation between the individual antennas implies that the aperture is very sparsely filled (Event Horizon Telescope Collaboration et al., 2019a,b,c). Observing at $\lambda \simeq 1.3$ mm, and including baseline projected lengths as large as 10,700 km (Event Horizon Telescope Collaboration et al., 2019a), the EHT has an angular resolution of $\simeq 25$ μas.

For the EHT, the scientific goal is to resolve and detect the signatures produced by general relativistic effects around the black hole at scales of the event horizon. We first need to define better what we mean by that. The black hole has an inner boundary that is called photon orbit, a bright ring of luminous plasma that is optically thin. This ring has a crescent shape, and its size and shape depends mainly on the mass of the black hole, and very weakly on its spin and observing orientation. Inside this ring is a dark region called the shadow of the black hole; its size for a non spinning black hole can be written in terms of the Schwarzschild radius, R_S like:

$$D_{shadow} = \sqrt{27} R_S, \quad R_S = \frac{2GM}{c^2},$$

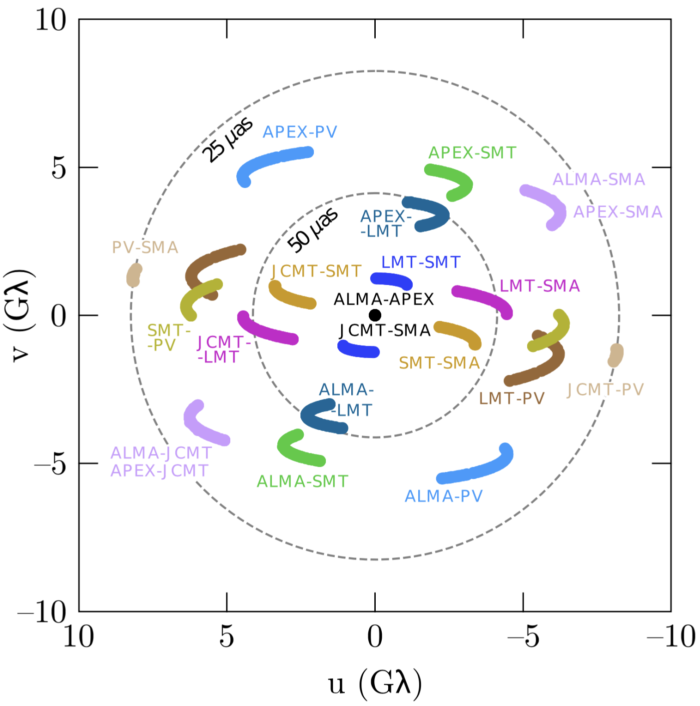

Figure 1.1: *EHT baselines coverage for M87 with the array used in 2017 (Event Horizon Telescope Collaboration et al., 2019b)*

.

where D_{shadow} is the diameter of the shadow, G is the gravitational constant, M the mass of the object and c the light speed. For a spinning black hole. the range of this diameter is $4.8\ R_S < D_{shadow} < 5.2\ R_S$.

Past observations using VLBI at 1.3 mm for both targets, M87* and SgrA*, confirmed the existence of structure at shadow scales in both objects.The scale of structure comparable with the event horizon of SgrA* was analysed using VLBI observations, increasing the angular resolution using long baselines (Doeleman et al., 2008). Before this observations, other observations at 7 mm and 3.5 mm were dominated by interstellar scattering effects. More recent studies revealed time-variable magnetic fields within SgrA* (Johnson et al., 2015).

In April of 2019, the first results of the EHT presented for the first time an image at the scale of the shadow of a black hole. This was the image of M87* (Figure 1.2) that presents a crescent shape with an asymmetric bright emission ring with a diameter of $42 \pm 3\ \mu$as corresponding to mass of $M = (6.5 \pm 0.7) \times 10^9\ M_\odot$.

1.1.1 The EHT array

As mentioned before, the EHT uses a technique called VLBI (Chapter 3). For this purpose, and considering the Earth-sized telescope needed, it was required to develop high-bandwidth VLBI systems that compensate the small aperture of each millimeter and submillimeter telescope that comprise the EHT array. A very important key in this project was also the use of high capacity hard drives to store

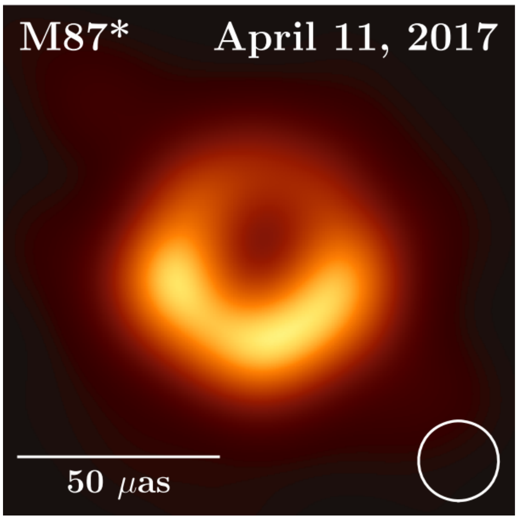

Figure 1.2: *First image of the shadow of a black hole obtained using the Event Horizon Telescope. This black hole, M87*, is located at the center of the giant elliptic galaxy M87 and has a mass of the order of 6.5* $\times 10^9$ $M_\odot$. *Credit: Event Horizon Telescope (`https://eventhorizontelescope.org/`)*

.

the data from each station at high speed. This large data recording increases the sensitivity of the array (Event Horizon Telescope Collaboration et al., 2019b).

It is very important to resolve not only spatially but also temporally the sources observed because they are time variable. SgrA* is a particularly good example of this as it varies on timescales on minutes. For this we can study the variability through light curves analysis. Resolving a source temporally means that at an increased resolution, sensitivity and baseline coverage, the EHT could resolve this time-variable structures.

To resolve SgrA* the angular resolution required was the resolution corresponding to the scale of the shadow diameter, that is of the order of $\sim 47-50$ μas. Taking advantage of the aperture given by the Earth rotation and the baselines of different stations, the EHT does have a sufficient sampling. Another thing to consider in the observations of SgrA* with the EHT is that the data present interstellar scattering by free electrons along the line of sight that blurred the images of this source. The blurring decreases with λ^2, and it is less dominant at wavelengths shorter than 1.3 mm (Doeleman et al., 2008), so it is possible to image the black hole structure near its event horizon using the VLBI technique at 1.3 mm.

Every telescope that participate as a station in the EHT already existed before the observations, and most of them required some modifications or upgrades to operate like VLBI stations. Incorporating ALMA to the EHT project greatly increased its sensitivity, and the resulting sensitivity matched well with the science goal. Figure 1.3 shows the full EHT array used in the observations of 2017 and 2018.

In april of 2017 the EHT carried out observations with an array of eight telescopes that included ALMA and APEX in Chile. Table 1.1 presents the participating tele-

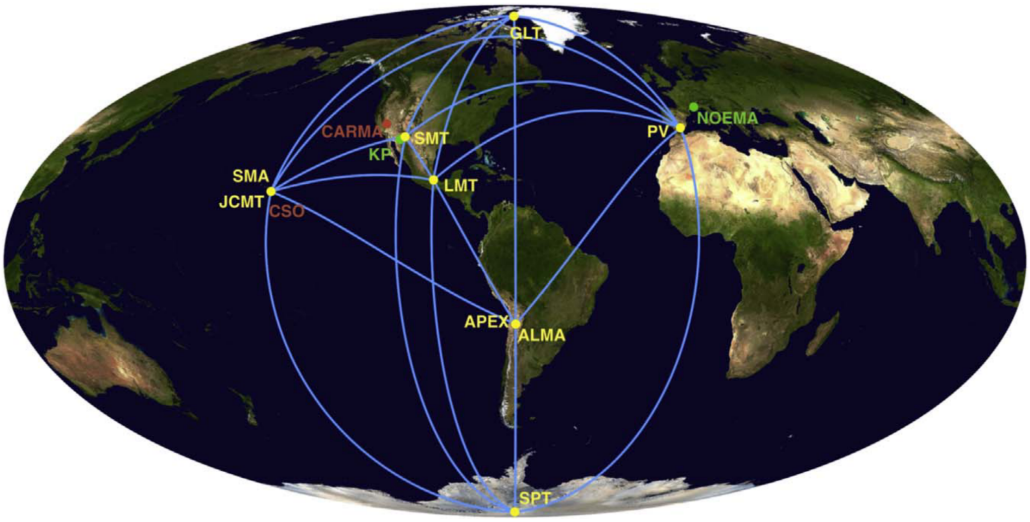

Figure 1.3: *Distribution of telescopes participating in the EHT for observations of 2017 and 2018, the active stations are labelled in yellow, sites in commission are labeled in green and legacy sites are labeled in red (EHT Collaboration et al. 2019b).*

.

scopes, their sizes and locations.

1.2 Phased arrays: ALMA as a single element

ALMA is an interferometer located in the desert of Atacama in Chile. It is comprised of 66 antennas of different sizes, 54 of them have a diameter of 12 m and the other 12 antennas have a diameter 7 m. This interferometer operates at high frequencies and observes at millimeter and submillimeter wavelengths. It is the most sensitive telescope in the EHT array. For this project, ALMA tends to be in a more compact configuration to facilitate calibration. Specifically, ~ 37 antennas of 12 m diameter participated during the 2017 EHT campaign.

Some stations of the EHT are interferometers, and have to operate like phased arrays. That means that the interferometer used as a station is incorporated as if it were a single dish in the bigger interferometric array (in this case, the EHT).

Phased arrays work by summing coherently the signals at the output of each single antenna that comprise the array. The signals are summed and recorded as if it was a single antenna. This requires a correction of the delays in the signals arriving to the dishes as well as corrections for the atmospheric delays due to the geometric path of the signals. Observing with ALMA as a phased array implies to perform phase corrections to the individual antennas relative to a reference antenna and then summing the phased signals within the ALMA correlator, where measurements are made and applied. This results in a virtual antenna of ~ 84 m diameter (Goddi et al., 2019b).

Table 1.1:

EHT stations

Telescope	Diameter (m)	Location	Year of operation
ALMA	12 (×54) and 7 (×12)	Chile	2017, 2018
APEX	12	Chile	2017, 2018
JCMT	15	Hawaii, USA	2017, 2018
LMT	50	Mexico	2017, 2018
PV, 30 m	30	Spain	2017, 2018
SMA	6 (×8)	Hawaii, USA	2017, 2018
SMT	10	Arizona, USA	2017, 2018
SPT	10	Antartica	2017, 2018
GLT	12	Greenland	2018
NOEMA	15 (×12)	France	2018
GLT	12	Greenland	2018
KP 12 m	12	Arizona, USA	2018

The ALMA Phasing Project (APP) was an international effort to produce a phasing system for ALMA enabling a large collecting area for VLBI applications (Matthews et al., 2017b).

1.2.1 Phasing efficiency

An ideal phased array of N elements or antennas is equivalent to having a single aperture of N times the collecting area of each antenna. However in a real phased array, some losses in the efficiency exist, decreasing the effective collecting area. The phasing efficiency, η_p (Equation 1.2), can be defined as the ratio between the cross correlation between summed signals and the comparison antenna, and the averaged cross correlation between the comparison antenna and the individual phased elements. The equation can be written in terms of the voltages of the comparison antenna (V_c), the summed signals (V_{sum}) and the individual antennas or elements (V_i).

$$\eta_p = \frac{\langle V_{sum} V_c \rangle}{\sqrt{N} \langle V_i V_c \rangle}. \tag{1.2}$$

The term $\langle V_i V_c \rangle$ is the mean of the correlated amplitude between each one of the N antennas. For a perfect phasing efficiency the value of η_p is 1, and the correlated amplitude is expected to grow as the square root of the number of antennas used to construct the sum (Matthews et al., 2017b).

For the Submillimeter Array (SMA) and ALMA, phasing systems were developed to be used as part of the observations of the EHT. For the SMA the phasing efficiency estimated over the course of several scans during a night of observation campaign is above 0.9 for most of the scans (Figure 1.3).

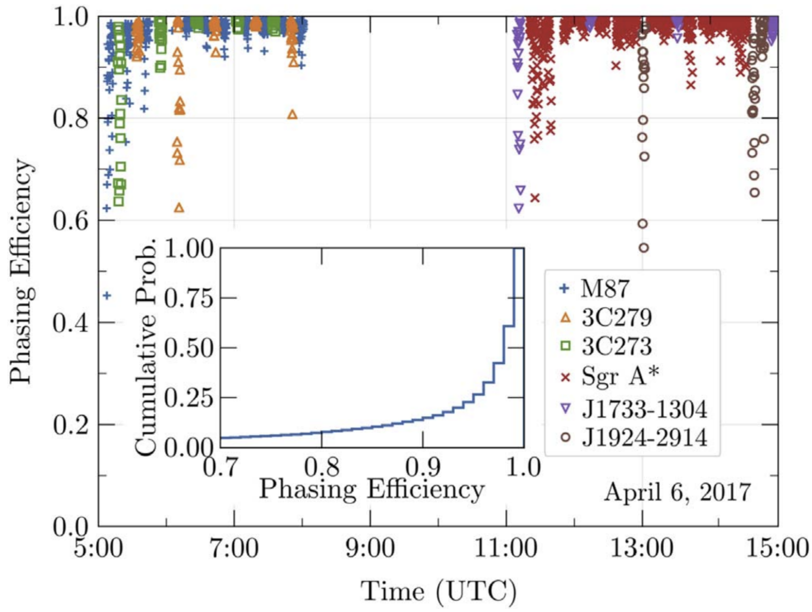

Figure 1.4: *Phasing efficiency of SMA for different sources during the EHT campaign in 2017 (Event Horizon Telescope Collaboration et al., 2019b)*

.

This efficiency was estimated using equation 1.3, where w_i is the complex-valued weight applied to antenna i.

$$\eta_p = \frac{\left|\sum_i w_i\right|^2}{\left(\sum_i |w_i|\right)^2}. \tag{1.3}$$

Phased arrays are capable of observing unresolved sources. Then, corrective beamformer weights can be computed from the output of the correlator extracting the contribution associated to a point-like source.

The phasing efficiency of ALMA was measured using "step scan" sequences considering a bright and compact source (Matthews et al., 2017a). In the "step scan" tests, the number of antennas that are part of the phased array vary. Some antennas are added or removed sequentially to evaluate how the correlated amplitude (that is related to the number of antennas) and the phasing efficiency scales with N. In this process, some antennas are phase corrected, while others are designated as comparison antennas. These ones are not part of the phased sum. When the phased sum signal is correlated with the comparison antenna (which is identical), the equation 1.4 is obtained:

$$\langle V_{sum} V_c \rangle = \left(\frac{V_0^2}{2} \right) \cos(2\pi\nu t), \tag{1.4}$$

where the term $V_0^2/2$ is the correlated amplitude, ν is the observing frequency and t is the integration time. The plot of the correlated amplitud as a function of the number of phased antennas is presented in Figure 1.4 (Matthews et al., 2017b), for Band 6 of ALMA during 10 minutes of observations obtained in March 2015. The filled dots are points of data of 16 seconds each one, and represent the correlated amplitude as function of the number of antennas obtained between the baselines of the phased sum and the unphased comparison antenna. The solid line represents the fit to the data with $N > 1$, and the asterisk represents the correlated amplitude comparable to a phased array of one antenna. The dotted line is the predicted result based on N = 1, and the dashed line represents an ideal phased array.

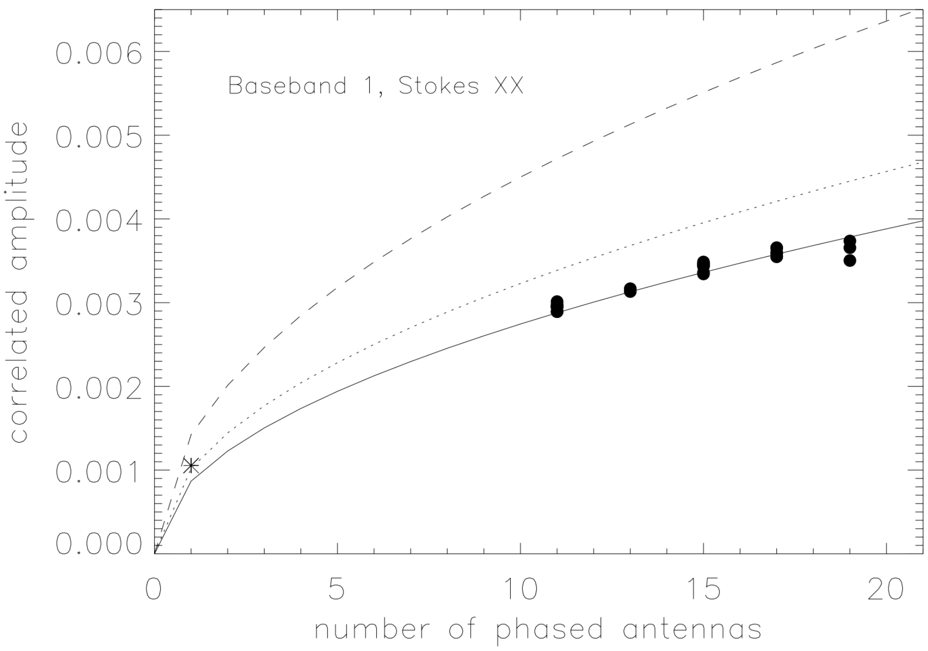

Figure 1.5: *Correlated amplitude as function of the number of phased antennas to evaluate the phasing efficiency.*

.

As one can see with the behaviour of the filled dots, the correlated amplitude is increasing with the number of phased antennas. For an ideal phased array the correlated amplitude could reach almost twice the value for a real phased array with these conditions. The fit matches really well the data so at the beginning the correlated amplitude for 1 phased antenna is almost the same for the 3 models. This test was made with 22 antennas, where three of them were assigned as unphased comparison antennas and the maximum number of phased antennas was 19. The phasing efficiency obtained during the observation was $\sim 61\%$.

1.3 The target: SgrA*

Sagittarius A* (SgrA*) is a radio object associated with a black hole candidate of 4×10^6 $M_\odot$ at the Galactic Center. Radio and infrared observations of SgrA* trace gas and dust heated up to very high temperatures when the material falls to the center of the black hole. At a distance of 8 kpc, the Schwarzschild radius subtends $R_{Sch} \sim 10$ μas.

VLBI observations revealed an ultracompact source and short time-scale variability is observed from radio to X-rays. Also, high resolution observations revealed a complex and extended structure around the core of SgrA*. This extended emission is made of ionized gas and is called "The mini spiral". In 1983, a team led by Ron Ekers used the Very Large Array (VLA) to make an image of the Galactic Center that revealed for the first time this spiral (Figure 1.6). This structure has components called the Northern Arm and Western Arm. Observations made with the VLA in band C with a field of view of 13 arcmins (30 pc) cover the center of the radio bright zone of the Galactic Center and allowed to image SgrA* with an angular resolution of 1 arcsec (Zhao et al., 2016).

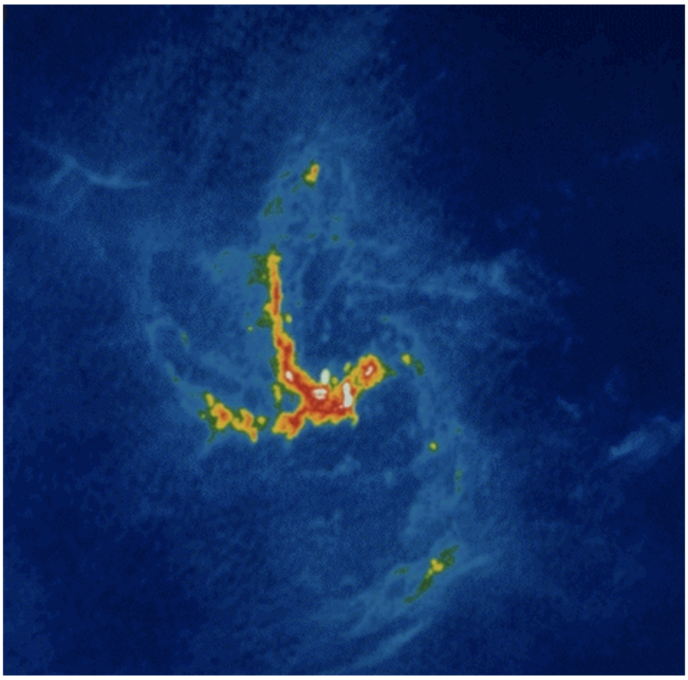

Figure 1.6: *Image with observations of VLA at 6 cm of the mini spiral at the Galactic Center, SgrA* (Killeen & Lo, 1989).*

.

In Figure 1.6, we can see the extended emission of the mini spiral that has a contribution to the flux of the whole object. A variable, compact source near the center of the image is associated with SgrA* itself.

SgrA* can be studied at the scale of its Schwarzschild radius with VLBI. SgrA* was observed using this technique at 1.3 mm and was obtained interferometric phase information of the object (Fish et al., 2011b). They observed a variability in the flux density at scales of the Schwarzschild radii as the flux during their third night of observation increased compared to the first two nights.

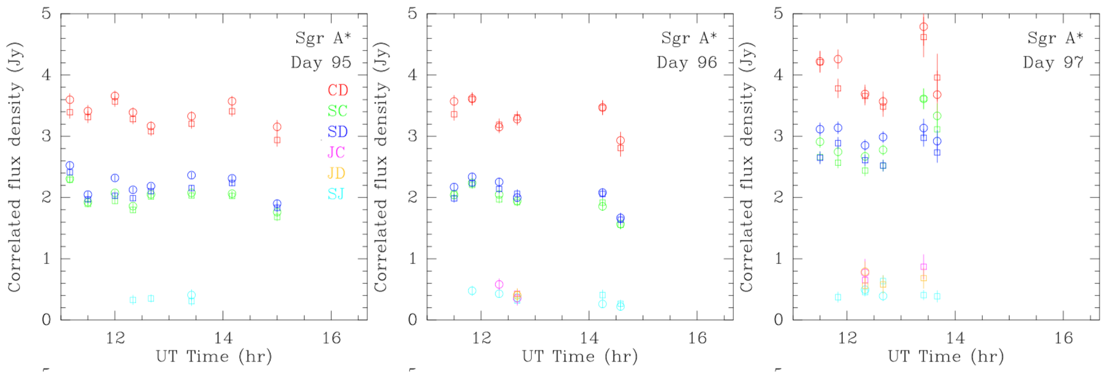

Figure 1.7: *Observations during 2009 April 5-7 (days 95, 96, and 97 respectively), detections are color-code by baseline: James Clerk Maxwell Telescope (J), Arizona Radio Observatory's Submillimeter Telescope (S), two telescopes of the Combined Array for Research in Millimeter-wave Astronomy (C and D, located* $\sim$ *60 m apart). Variability in SgrA*, on day 95 and 96 the flux density is the same within the uncertainties, but on the day 97 the flux density was* $\sim$ 17% *higher (Fish et al., 2011b).*

1.4 Motivation

ALMA is an interferometer that plays a very important role in the EHT thanks to the high sensitivity that it brings to the observations. However, as was discussed before, ALMA needs to be phased to be incorporated in the project. In Section 1.2.1 we mentioned that there exist measurements of the phasing efficiency of ALMA as a phased array considering a compact source as target – in this case, the Galactic Center, SgrA*. But we know that SgrA* is not comprised by only a compact component, it also has an extended component produced by ionized gas (the mini-spiral). With the high sensitivity of ALMA during the EHT campaigns, enough data is available to create an ALMA image of SgrA* and separate the mini-spiral from the compact emission. The goal of this thesis is to measure the effect of this extended emission around SgrA* on the phasing efficiency of ALMA as an EHT element. As a by-product, we also obtain light curves of the Galactic Center.

Chapter 2

The Galactic Center: SgrA*

As mentioned in the Introduction, it is well accepted that galaxies have at their centers a SMBH. Indeed, black holes have become an important component of the big picture of the Universe. In this chapter, we present a general description of black holes and describe how a SMBH was discovered at the center of the Milky Way: Sagittarius A* (Sgr A*). This is the object of study in this work.

2.1 General properties of Black Holes

Black holes are objects which produce a gravitational field so strong that any matter that approaches sufficiently cannot escape. They are particularly interesting to test theories of gravity. The only known way to form a black hole is through the gravitational collapse of a very massive star.

To understand more about the concept of a black hole it is useful to see what happens when a huge amount of matter collapses. In 1795, Laplace considered what would happen if one reduced the radius r of a celestial body of mass M. Since the escape velocity υ_{esc} at its surface is given by:

$$\upsilon_{esc} = \sqrt{\frac{2GM}{r}}, \tag{2.1}$$

if the radius is made smaller and smaller, then the escape velocity will increase and eventually reach the speed of light c. This happens when the radius decreases to:

$$R_S = \frac{2GM}{c^2} = 2.95 \times 10^5 \mathrm{cm} \left(\frac{\mathrm{M}}{\mathrm{M}_\odot}\right) \tag{2.2}$$

The remnant created in the collapse of a supermassive star that had exhausted all its sources for nuclear fusion, could have a mass above the limit (about 3 $\mathrm{M}_\odot$) for neutron stars (Oppenheimer & Snyder, 1939). Remnants more massive than this limit must collapse and form a black hole. (Schneider, 2016). Non-rotating black holes generate a perturbation of their surrounding space-time described by the Schwarzschild metric (Equation 2.3), named after Karl Schwarzschild (1873-1916), who discovered the solution to the Einstein's field equations that describes the gravitational field of a non-rotating point mass in 1916. In Equation 2.2, R_S is the Schwarchzschild radius. In carthesian coordinates, the Schwarzschild metric is written:

$$(ds)^2 = \left(cdt\sqrt{1-2GM/rc^2}\right)^2 - \left(\frac{dr}{\sqrt{1-2GM/rc^2}}\right)^2 - (rd\theta)^2 - (r\sin\theta d\phi)^2. \quad (2.3)$$

If we have two different observers, one on the collapsed star and the second one at a distance far away, then for the first observer the speed of light must be always c. For the second one, the light is delayed as it moves through the curved spacetime (Taylor, 2005). Let us see what happens with a photon that is travelling radially inwards.

The coordinate speed of light is the rate at which a photon changes its coordinates. We can calculate it using Equation 2.3 with $ds = 0$, and considering a photon travelling radially (only along the r spherical coordinate) we have $d\theta = d\phi = 0$, then, the coordinate speed of light in radial direction is:

$$\frac{dr}{dt} = c\left(1 - \frac{2GM}{rc^2}\right) = c\left(1 - \frac{R_S}{r}\right). \quad (2.4)$$

If we analyse the case for a position r at the Schwarzschild radius, $r = R_S$, then $dr/dt = 0$. That means that light is "frozen" at the Schwarzschild radius, so this radius acts like an spherical barrier that doesn't allows us to see beyond it. This is the event horizon. This element of the black hole is a mathematical surface but there is no material surface associated with it. It is enclosing the singularity (at $r = 0$ in the Schwarzschild solution). The singularity is the location where all the matter of the black hole is concentrated; its volume is zero and the density there is infinite. For these reasons, space-time is infinitely curved at the singularity. In back holes, the singularity is hidden behind the event horizon.

In summary, a black hole is formed when the size of a gravitating object of mass M becomes smaller than its Schwarzschild radius r_S. Its boundary surface is called Event Horizon which defines a region inaccessible to an outside observer; at the center resides a singularity.

A Schwarzschild black hole is entirely defined by its mass. For a rotating (or spinning) black hole, a second quantity must be taken into account: the angular momentum

$$s \sim I\Omega \simeq Mr_g^2\left(\frac{v}{r}\right) \simeq Mr_g c. \quad (2.5)$$

It is useful to also define the specific angular momentum, i.e. the angular momentum per unit mass.

$$\frac{s}{M} \equiv \alpha c. \quad (2.6)$$

In the previous two equations, Ω is the angular velocity at the horizon, $r_g = R_S/2$ and $\alpha = ar_g$ is a specific angular diameter with $a \in [-1, 1]$, the sign of a refers to the direction of rotation. For a non-rotating black hole, the event horizon is located at the Schwarzschild radius: $R_S = 2r_g$. For a rotating black hole, there in an inner and an outer horizon located respectively at

$$r_{\pm} = \frac{R_S \pm \sqrt{R_S^2 - 4a^2}}{2}.$$

Note that for $a = 0$, $r_+ = 2r_g = R_S$: we recover the Schwarzschild radius of the event horizon as appropriate for the non-rotating black hole.

The solution of the field equations for a rotating black hole (i.e. the equivalent of the Schwarzschild metric for a non-rotating black hole) is the Kerr metric. The Kerr metric also defines another surface outside of the two event horizons. This region is the static limit. Beyond this boundary any particle remains at the same coordinate as the effect of frame dragging diminishes. When a massive object in the Universe is rotating it induces a rotation of the surrounding spacetime, this effect is called frame dragging. The region between the static limit and r_+ is called the ergosphere.

The ergosphere is a non spherical surface that is outside the black hole. Within the ergosphere, the frame dragging is so severe that any particle must move in the same black hole rotation direction. Also because the black hole is rotating, something else happens with the shape of the singularity and the event horizon. The singularity goes from a point to a flat ring, while the event horizon becomes an ellipsoid (Carroll & Ostlie, 2014). The overall structure of a rotating black hole is shown in Figure 2.1.

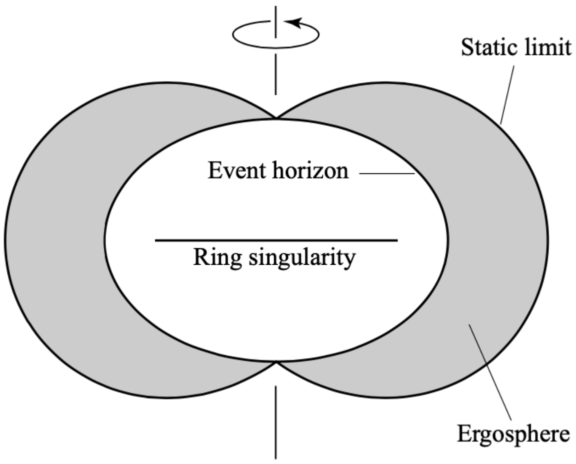

Figure 2.1: *Structure of a rotating black hole, with the singularity seen edge on (Carroll & Ostlie, 2014).*

.

2.2 Mass ranges of Black Holes

The mass M of a black hole is the only dimensional parameter that defines its size scale. Observations have revealed the existence of two classes of black holes called stellar and supermassive black holes. There seems to be a paucity of black holes between these two types.

2.2.1 Stellar Black Holes

Stellar black holes are the final stage in the life or stellar evolution of a very massive star – above 20-30 $M_\odot$. They are the remnants of core collapse supernovae of massive progenitors. Stellar black holes were first described by Oppenheimer and Snyder.

The best candidates to stellar black holes are in X-ray compact binary systems. These systems are composed of a black hole and a normal star moving around their common center of mass. In these systems, the normal star is acting as a source of matter for the black hole. The matter is falling into the black hole with an angular momentum as it moves in the plane of the rotation of the system, and it forms an accretion disk around the black hole. Matter does not fall until it loses the angular momentum.

An example of this type of black holes in binary systems is Cygnus X-1 (Figure 2.2), which is a bright high-mass X-ray binary composed by a confirmed black hole (Bolton (1972);Webster & Murdin (1972)). Its companion is the supergiant star HDE 226868 (Walborn, 1973). The mass of the black hole in this system was estimated as $M_{BH} = 14.8 \pm 1.0$ $M_\odot$ (Orosz et al., 2011). Using radio astrometry combined with archival optical data, a mass of $M_{BH} = 21.2 \pm 2.2$ $M_\odot$ was obtained for the mass of the black hole, which is significantly higher than previous measurements (Miller-Jones et al., 2021).

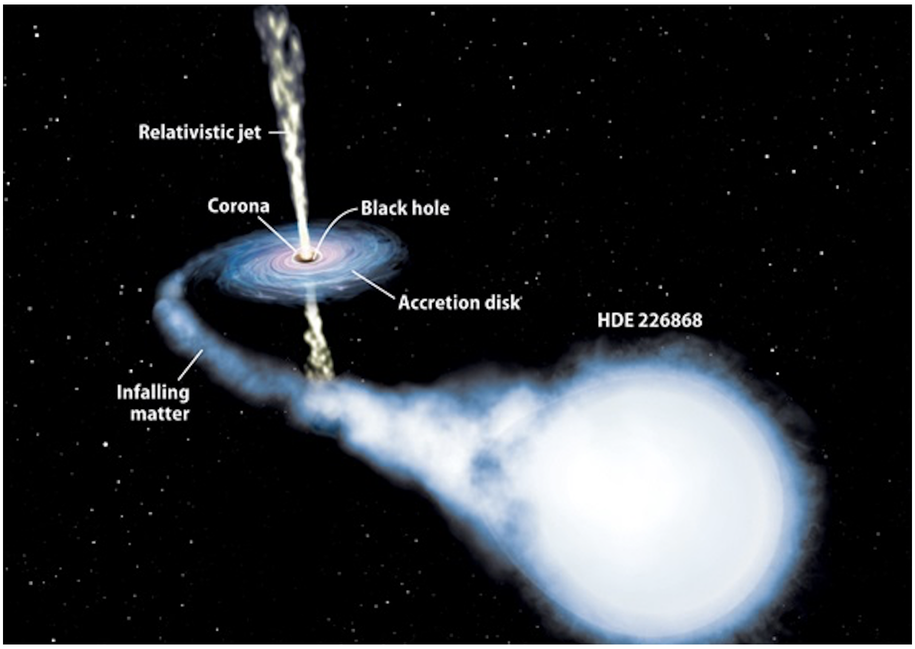

Figure 2.2: *Artistic representation of Cygnus X-1 and its companion. The matter from HDE 226868 is falling to the accretion disk around the black hole.*

.

2.2.2 Intermediate mass Black Holes

Black holes with masses between 100 $M_\odot$ and over 1000 $M_\odot$ are classified as intermediate mass black holes. Candidates to these objects known as ultraluminous X-ray sources were discovered with X-ray satellite telescopes as Chandra and XMM Newton. How they are formed is still an open question but it is suggested that these black holes are formed by mergers of stars that result in a supermassive star, or by merger of stellar black holes.

Interestingly, the gravitational-wave signal GW190521 detected in 2019 is attributed to the merger of a binary system of two black holes of masses 85^{+21}_{-14} $M_\odot$ and 66^{+17}_{-18} $M_\odot$. This resulted in the formation of a black hole with a final mass of 142^{+28}_{-16} $M_\odot$. This classifies as an intermediate mass black hole (Abbott et al., 2020).

2.2.3 Supermassive Black Holes (SMBH)

This type includes the most powerful black holes that were discovered in the centers of active galaxies. Such nuclei are seen in both spiral and elliptical galaxies. Supermassive black holes are present at the center of almost all the galaxies, but only a small fraction have an active nuclei. The most powerful source of radiation in the Universe are quasars, with a total luminosity of $10^{47} - 10^{48}$ erg/s. Their activity is powered by a central SMBH that acts as a central engine of radio emission. The mass of these black holes is in the range from 10^5 $M_\odot$ to 10^9 $M_\odot$.

The material that falls into a SMBH is gas and stars that surround it. There is still an open question about the formation of SMBH, and there are some models that try to explain it. One suggestion is that they are formed in galaxy collisions. Other models propose a collapse of a dense stellar cluster. It has also been proposed that they may form in a galaxy as a result of slow matter accretion into an original stellar black hole at the center of the galaxy.

A good example of a SMBH is Sagittarius A* (Sgr A*), located at the center of our Galaxy, the Milky Way, at a distance of 8.34 kpc (Reid et al., 2014). Stellar orbits around Sgr A* provide very strong indications of the presence of a SMBH with a mass of about 4.1 $\times 10^6$ $M_\odot$ (GRAVITY Collaboration et al., 2018).

2.3 Sagittarius A complex

Before we present the evidence for the presence of a SMBH at the center of the Milky Way, let us discuss the Galactic Center (GC) region in more general terms. Because it is located in the direction of the Sagittarius constellation, this region is usually referred to as Sagittarius. It is important to mention that there is gas and dust along the line of sight between us and the GC, that makes it impossible to see the GC in the optical and the UV. Therefore we must use other wavelengths to see the emission that comes from there.

Radio observations in the direction of Sagittarius show a relatively complex structure (Figure 2.3) including radio filaments perpendicular to the Galactic plane and a large number of supernova remnants. This region was divided into several sub-regions (Sgr A, Sgr B, Sgr C, etc.). Sgr A is the brightest sub-region at radio wavelengths and is the component associated with the Galactic center itself.

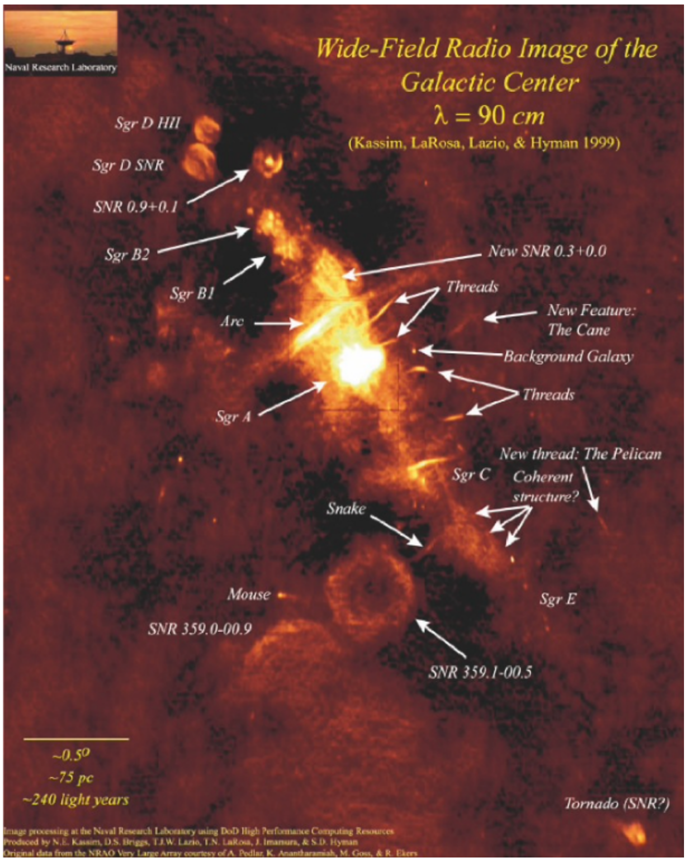

Figure 2.3: *90 cm VLA image of the region around the Galactic Center where several sources are distinguished.*

Zooming in on Sgr A, several sub-components have been identified in different observations. The so-called **circum-nuclear disk (CND)** is an elongated ring of dense material centered on the GC. Its diameter is about 2.5 pc, and it is associated with molecular clouds consisting of warm, neutral, dense and turbulent gas. The CND rotates around Sgr A* with a rotational velocity of 110 km/s. It has a sharp inner edge that encloses a cavity; its mass is estimated to be about 10^4 $M_\odot$. Inside the cavity resides a massive stellar cluster first detected in observations at $\lambda \sim 2\mu m$ (K-band; Becklin & Neugebauer (1975)). The velocity dispersion, σ, in this cluster is large, and increases with decreasing radius, from $\sigma \sim 55$ km/s at $r = 5$ pc to $\sigma \sim 180$ km/s at $r = 0.15$ pc. This strong dependence with the radii suggests that the gravitational potential where these stars are immersed is not originated by themselves. Rather, it suggests the presence of a large central mass in the stellar cluster.

Also inside the CND, there is the so-called **mini-spiral** that connects to the CND on the outside and the stellar on the inside. The mini-spiral is principally composed of ionized gas and dust streamers. All this material is organized in different components that can be distinguished in Figure 2.5. The Northern and Eastern arms represent the dominant portion of gas and dust in the structure. They are located in the main plane with an inclination angle of $\sim 25°$, and radii of 2 pc $\lesssim R \lesssim 8$ pc. The CO (7-6) emission from this region strongly suggests that warm molecular gas is flowing into the cavity. From this CO (7-6) emission, the total mass of the Northern arm can be estimated in the range of 5 - $50 M_{\odot}$. The two arms appear to connect near the very GC.

Finally, also present in Sgr A are two sub-structures called Sgr A East and West. The Sgr A East is a non-thermal (synchrotron) source with a shell-like structure, which is a possible supernova remnant. Sgr A West is a thermal source tracing an unusual HII region with an spiral structure.

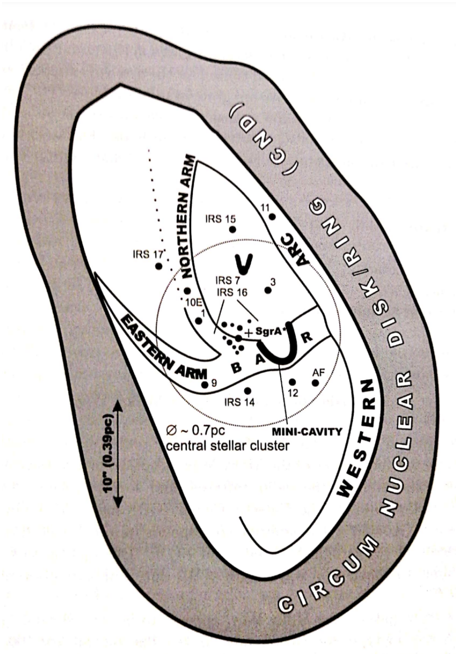

Figure 2.4: *Schematic pictures of the different structures in the Galactic Center, presenting the scales of each one (Eckart et al., 2005)*

.

2.4 Evidence for the existence of a SMBH at the center of the Galaxy

The proximity of our Galactic Center (GC), at 8.36 kpc (Reid et al., 2014), provides a good opportunity to study a SMBH and its environment.

The first detection of the region of Sgr A was in 1974 (Balick & Brown, 1974). An interferometer of three elements in Green Bank and a 45 feet antenna was used. It had sufficient sensitivity to resolve ~ 25 Jy of extended emission in this source, known as Sgr A West. This led to the detection of a compact source with fluxes of 0.6 Jy at 11 cm and 0.8 Jy at 3.7 cm. The angular resolutions at these wavelengths of $0.7''$ and $0.3''$, were obtained respectively. Brown (1982) first used the name Sgr A* to refer to the compact source, and distinguish it from the extended emission. The first detection of Sgr A* was obtained with Very Long Baseline Interferometer (VLBI), with a 242 km baseline between Owens Valley Radio Observatory (40 m antenna) and the NASA Goldstone 64 m antenna at 3.7 cm wavelength (Lo et al., 1975). The measured flux density of the compact source was 0.6 Jy. The comparison of measurements from different authors suggests that the emission of Sgr A* may be variable in time. Recent studies have confirmed this conclusion; the variability occurs on timescales from minutes to hours.

From observations with an angular resolution of $2.5''$, was also found that this compact radio source was nearly centered on the stellar cluster of Becklin and Neugebauer (1975) (Lo et al., 1975). Recent measurements of the proper motion of Sgr A* (Reid & Brunthaler, 2020) show that it is essentially at rest relative to the Galactic Center, with a residual velocity below 1 km s^{-1}. Sgr A* is close to the west in the Sgr A complex, and has a radio luminosity $L_{rad} \sim 2 \times 10^{34}$ erg/s.

2.4.1 Kinematic evidence

The presence of a SMBH at the Galactic Center was probed with kinematic measurements in the innermost parsecs. These measurements led to the conclusion of a compact mass centered at Sgr A*.

The first hint of a central concentration of mass came from radial velocity measurements of ionized gas located in the mini-spiral (Lacy et al., 1980). However, the kinematic of gas is not the best indicator of mass because it could be affected by magnetic fields. A better indicator is stellar kinematics.

In 1995 was initiated a high-resolution imaging program to observe the inner 5 pc $\times$ 5 pc at 2.2 μm of the central cluster of the Galaxy (Ghez et al., 1998). There was collected thousands of short exposure frames with an angular resolution of 0.05 arcsec. Using a sample of 90 stars, two-dimensional velocities were measured, with velocities reaching up to 1400 km/s. Out of these 90 stars, three have significant accelerations; they are the fastest stars in the sample and closest stars to the nominal position of Sgr A*. These stars were named as S0-1, S0-2 and S0-4 (Ghez et al., 2000). The table below (Table 2.1) lists the measurements for these three stars.

Measurements for stars with significant acceleration			
Name	S0-1 (S1)	S0-2 (S2)	S0-4 (S4)
Radius from Sgr A* (milliparsecs)	4.42 ± 0.05	5.83 ± 0.04	13.15 ± 0.04
Velocity magnitude (km/s)	1350 ± 40	570 ± 20	990 ± 30
Acceleration magnitude (milliarcsec/yr^2)	2.4 ± 0.7	5.4 ± 0.3	3.2 ± 0.5

Table 2.1: Measurements for the most significant accelerated stars in the sample of 90 stars from the work of Ghez et al. (2000).

Stars within the 0.6″ of Sgr A have tangential velocities greater than 1000 km/s; the fastest star is S1, which is located at $\sim 0.1''$ from the compact radio source (Sgr A*) has a tangential of $\sim$ 1470 km/s Genzel (2000). S2 at a distance of 6×10^{-4}pc and has an orbital period of $\sim$ 15.7 yr and an eccentricity of 0.87. With statistical treatments of velocities, the dynamical center was located within $\pm$ 0.1 arcsec (1σ) of the Sgr A* position. Excellent orbital fits were found for S1 and S2 for the entire range of masses within 0.01 arcsec of the nominal position of Sgr A* (Ghez et al., 2000) that suggests the existence of a comparable accurate position measurement to the dynamical center of our Galaxy (Figure 2.4).

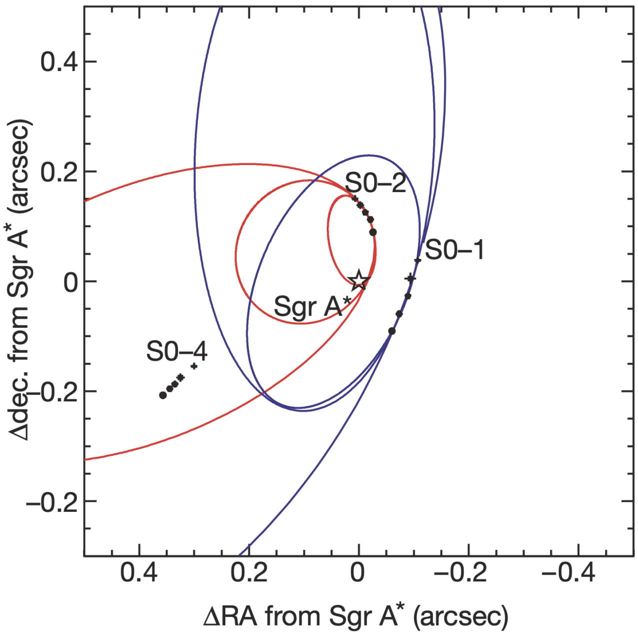

Figure 2.5: *The measured motion of S1, S2 and S4 and several allowed orbital solutions (Ghez et al., 2000).*

.

From the observed kinematics, the enclosed mass can be calculated, and a constant radial mass distribution $M(r)$ at 0.1 pc $\lesssim r \lesssim$ 0.5 pc is observed, that indicates the presence of a point mass of about $M = (3.6 \pm 0.4) \times 10^6 M_\odot$.

At a distance of $\sim$ 8 kpc, the Sgr A* Schwarzschild radius is 10 μas, or 0.1 astronomical units (AU). Very-long baseline interferometry (VLBI) at 7 mm and 3.5 mm wavelength shows the intrinsic size of Sgr A* to have a wavelength dependence. VLBI images with observations at wavelengths longer that 1.3 mm are dominated by interstellar scattering effects that broaden images of Sgr A* (Doeleman et al., 2008). On 10 and 11 april 2007, Sgr A* was robustly detected on the short Arizona Radio Observatory 10-m Submillimetre Telescope (ARO/SMT)-Combined Array for Reasherch in Millimeter-wave Astronomy (CARMA) baseline and the long ARO/SMT-James Clerk Maxwell Telescope (JCMT); the high signal to noise ratio, coupled with the tight gruoping od resifual delays and delay rates, makes the detection robust and unambiguous (Doeleman et al., 2008). These data are presented in Table 2.2.

VLBI detections of Sgr A* with ARO/SMT-JCMT baselines at $\lambda = 1.3$ mm			
Date	Correlated Flux (Jy)	SNR	Projected baseline length ($10^6\lambda$)
10 April 2007 12:20	0.38	5.8	3558
11 April 2007 11:00	0.37	5.0	3443
11 April 2007 11:40	0.34	5.4	3535
11 April 2007 12:00	0.31	5.8	3556

Table 2.2: Each detection was made by incoherently averaging the VLBI signal and searching for a peak in signal to noise ratio over of ± 18 ns in delay. From a total of 15 separate 10 minutes scans, Sgr A* was detected four times on the ARO/SMT-JCMT baseline. A weak detection of the source during the observations could be due to the intrinsic variations of flux density of the source (Doeleman et al., 2008).

The minimum intrinsic brightness temperature derived from the results of 1.3 mm observations on (Doeleman et al., 2008) is 2 $\times 10^{10}$ K. Also these observations, demonstrated that VLBI at 1.3 mm can directly detect structure in Sgr A* on event horizon scales. Evidence of flares from light curves of Sgr A* from the radio to X-ray (Eckart et al. (2006); Yusef-Zadeh et al. (2006); Marrone et al. (2008)) implicates the presence of structure on smaller scales ($\sim 5 - 15 R_{Sch}$), and from these observations. Variability of the source from minutes to hours was found.

The bright core of Sgr A* is one of the primary targets of the EHT, and with the results of previous VLBI observations as mentioned before, the existence of structure on the scale of the shadow in the nucleus of Sgr A* is confirmed. The 1.3 mm emission has been measured to have a size of 3.7 R_{Sch} (Doeleman et al. (2008), Fish et al. (2011b)). With this, the properties used to establish technical goals to observe Sgr A* are presented in Table 2.3.

Sgr A* assumed physical properties for EHT goals		
Property		Sgr A*
Black Hole Mass	M ($M_\odot$)	4.1×10^6
Distance	D (pc)	8.34×10^3
Schwarszchild radius	R_S (μas)	9.7
Shadow diameter	D_{sh} (μas)	47-50
Brightness temperature	T_B	3×10^9
Mass accretion rate	$M_\odot$ yr^{-1}	$10^{-9} - 10^{-7}$

Table 2.3: Assumed properties for the compact source Sgr A* candidate as a SMBH at the center of the Galaxy for the EHT science goals (Event Horizon Telescope Collaboration et al. (2019b)).

Chapter 3

Basics of Interferometry

A single dish radio telescope is an antenna or dish that can receive the signal of a source of monochromatic brightness. Due to an incident wave at the detector, a varying voltage is produced at the terminals of the antenna. This voltage varies with the same frequency as the incident electromagnetic wave. In this case, the angular resolution is given by:

$$\Delta\theta \sim \frac{\lambda}{D} \text{ radians} \tag{3.1}$$

The angular resolution is the capacity of the instrument to distinguish between two objects of a minimum distance of $\Delta\theta$. Based on equation 3.1, where D is the telescope diameter, the Hubble Spatial Telescope (HST) has an angular resolution of 0.5 arcsec due to the observed wavelength of $\lambda \sim 500$ nm and a diameter of 2.4 m. For radio observations in the millimeter regime, an antenna of 5 km diameter will be needed to reach this resolution. Instead of this, arrays of small antennas are used to reach higher angular resolutions. This technique is called interferometry.

Interferometry is a technique that consists in combining signals from an array of single dish elements. In that case, the angular resolution is given by Equation 3.1 but using the maximum distance between any pair of antennas in the array as D, rather than the size of the individual telescopes in the array. The separation between dishes in an interferometer is called baseline, and D in equation 3.1 is the maximum baseline in the array. The signal from the observed object arrives at each single antenna in the array at different times. This provides different travel lengths, which are important for positional information about the emitting object. To measure this slight time difference very accurate clocks are used. The signal of each antenna is combined with the rest of all other antennas in a correlator.

A basic interferometer (Figure 3.1) is composed by a pair of antennas, whose individual voltages are multiplied and averaged to get the final result. Voltages at the output of each antenna:

$$V_1 = V_{01}\cos(2\pi\nu t), \tag{3.2}$$

$$V_2 = V_{02}\cos(2\pi\nu t + \phi), \tag{3.3}$$

are sent to the multiplier that is at the same distance of both. The output of the correlator is

$$V_1V_2 = V^2\cos(\omega t)\cos[\omega(t-\tau_g)] = \frac{V^2}{2}[\cos(2\omega t - \omega\tau_g) + \cos(\omega\tau_g)], \tag{3.4}$$

where $\nu = \omega/(2\pi)$, $\phi = \pi\Delta s/\lambda$, and $|\Delta s| = |r|\cos\theta$ is the distance that radiation must travel to arrive to the second antenna. This extra distance corresponds to a time delay given by $\tau_g = B\lambda\cos\theta/c$. Following by multiplication, the correlator averages the output over a time interval long enough $[\delta t \gg (2\omega)]^{-1}$ to remove the high frequency term. The final output is:

$$R =< V_1V_2 >= \frac{V^2}{2}\cos(\omega\tau_g). \tag{3.5}$$

The first term refers to the amplitude that represents the source intensity, and the argument of the cosine is the phase that depends on location, baseline and observing frequency.

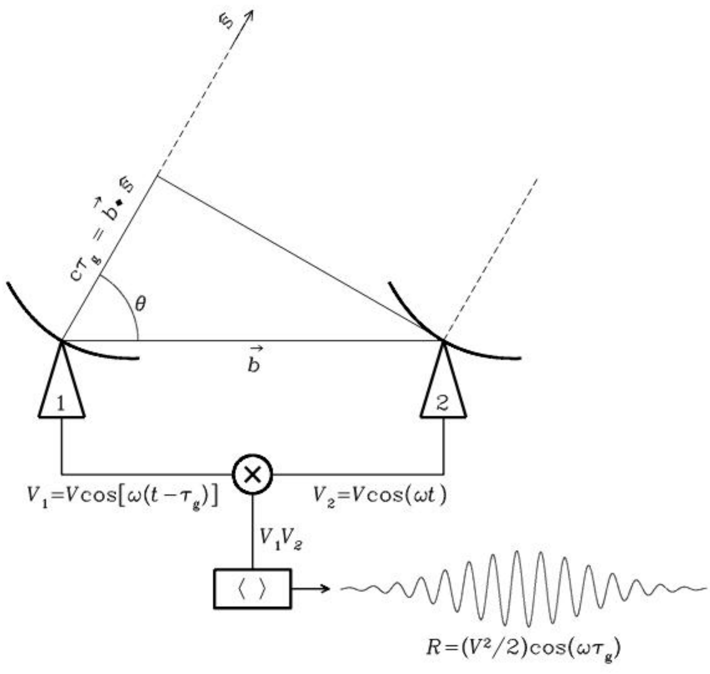

Figure 3.1: *Schematic diagram of a two elements interferometer, where voltages V_1 and V_2 are multiplied and averaged later to produce the output of the interferometer.*

.

3.1 Calibration process

When expressed as a function of the separation between the antennas in the array, the output of the correlator is called a visibility. The visibilities measure the amplitude and phase of the cross-correlated signals between pairs of antennas as a function of time and frequency. An interferometer measures phase differences, so there is no absolute phase reference. The purpose of the calibration process is to remove instrumental effects and atmospheric variations in the data before imaging. We calibrate the data observed by determining the complex gains of amplitude and phase, the frequency responses (bandpass) and flux scale for each antenna. The gain calibration is applied to amplitudes and phases, to remove (time-varying) atmospheric and instrumental contributionduring observations. Bandpass calibration fixes instrumental effects and variations in frequency, and the flux calibration scales relative amplitudes to absolutes values.

The principal step to calibrate data is gain calibration. This requires a source used as calibrator that must be a point source near the target. The calibrator is observed every few minutes during the total observations. This is used to determine variations of phase and amplitude over time.

3.2 The VLBI technique

In 1967, a new technique of interferometry was developed. Consisting in elements not linked between them in real time, Very Long Baseline Interferometry (VLBI) was accomplished by recording the data for cross correlation at a later time at a central processing station. This type of interferometer has been distinguished from other radio-interferometers by the absence of any direct link between stations for received signals. Figure 3.2 summarizes the basis of this technique.

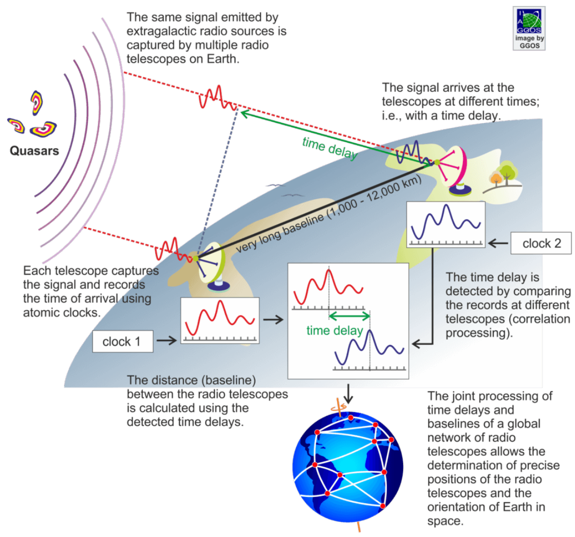

Figure 3.2: *Schematic diagram of a two station VLBI interferometer. Credit:GGOS by Laura Sanchez (ggos.org).*

.

This technique allows the possibility of using elements anywhere reaching baselines nearly as long as the diameter of the Earth or even satellites. The resolution achieved by large VLBI arrays is typically of order of milliarcseconds (mas), giving to VLBI arrays the highest resolution of any telescope and technique. This resolution achieves the principal motivation of developing VLBI, which is to resolve structures of many radio sources that cannot be resolved with conventional radio-interferometer. Such sources include the center of active galactic nuclei (AGNs). The prices to pay for the high resolution reached by such long baselines is low sensitivity and relatively unstable visibility phases.

VLBI can be used only to study objects with non-thermal emission processes. To be detected on a baseline of lenght D, the source must be smaller than the fringe spacing. Since flux density S is given by Equation 3.6, where T_B is the brightness temperature, k is the Boltzmann constant, λ is the wavelength and $\Omega \simeq \pi(\lambda/2D)^2$ is the source solid angle; the minimum detectable T_B is given by Equation 3.7.

$$S = \frac{2kT_B\Omega}{\lambda^2} \tag{3.6}$$

$$(T_B)_{min} \simeq \frac{2}{\pi k} D^2 S_{min} \tag{3.7}$$

Thus, target sources must have brightness temperatures of million degrees or more to be detected. VLBI also uses the next important step in the development of interferometry: Earth Rotation in Synthesis Imaging. This technique uses the variation of the antenna baselines provided by the rotation of the Earth (Figure 3.3). Taking data at different times during a period provides measurements with different telescope separations and angles without the need of additional telescopes or moving them, as the rotation of the Earth moves the telescopes to new baselines.

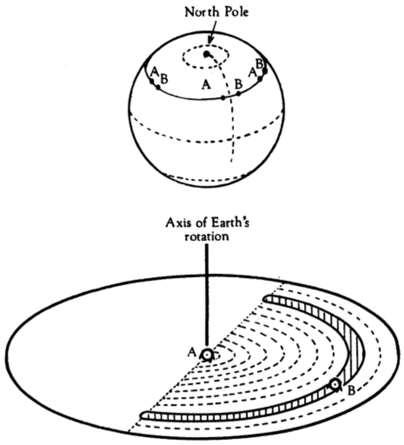

Figure 3.3: *Earth rotation used in synthesis mapping; antennas A and B are spaced on an east-west line, by varying the distance between them and observing during an amount of time, it is possible to fill all the spacing from the origin to the final position. From Nature, Vol. 194, No. 4828, p. 517.*

.

The rotation of the Earth can be used to sample the U-V plane. The baseline vector between two antennas on the Earth is continuously changing because of the Earth's rotation seen from a distant source. From the inverse relationship of Fourier conjugate variables it follows that short baselines are sensitive to large angular structures in the source and that long baselines are sensitive to fine scale structure.

3.3 ALMA phasing system

Since the achievable image angular resolution of an interferometer is expressed by Equation 3.1, the higher frequencies provide the higher resolving power. High frequency (millimeter) VLBI thus provides the highest position angular resolution. It is, however, affected by observational and technical challenges. It requires telescopes with higher surface accuracy than at longer wavelengths; the atmospheric distortion effects on the radio wave are more severe than at lower frequencies; a higher stability is required for atomic clocks. In order to overcome these limitations, a beamformer for ALMA within the ALMA Phasing Project (APP) has been developed (Matthews et al. (2017b)).

ALMA is the most sensitive (sub)mm-wave telescope ever built. The beamformer can aggregate the entire collecting area of ALMA into a single and very large aperture. This requires the alignment in phase of the signals from individual antennas and their summation, turning ALMA into a virtual single dish antenna of 84 meters. This virtual antenna can be incorporated into a bigger array as a giant station in a VLBI experiment.

The ALMA Phasing System (APS) performs a phase correction to the signals coming from every individual antenna of the designated array to create a phased array. This corrections are computed relative to a reference antenna usually chosen near the center of the array. Table 3.1 presents the characteristics of the ALMA Phasing System.

Table 3.1: Sumarize of characteristics of the APS (Matthews et al., 2017b)

Characteristics of ALMA Phasing System	
Feature	Specification
Number of phased antennas	≤ 61
Equivalent collecting area	4185 m^2
Frequencies of operation	ALMA Bands 3 (84-16 GHz) and 6 (211â275 GHz)
Effective bandwidth per quadrant	1.875 GHz
VLBI recording speed	64 Gbps

Motivated by the first detection of event horizon scale structure in Sgr A* at 1.3 mm baselines (Doeleman et al., 2008), the 1.3 mm array Event Horizon Telescope (EHT) was expanded over the following years adding new stations including ALMA. As mentioned earlier, ALMA can be used as a single large-aperture VLBI antenna if the data from its individual antennas are phase-corrected and coherently added.

The ALMA array comprises 66 antennas, 12 of them with 7 m diameter, and 54 with 12 m diameter. Relatively compact configurations are the most desirable for phased array operations, since decorrelations of signals caused by variations in the atmosphere above each of the antennas is minimized (Matthews et al. (2017b)). Some functional requirements for the APS include:

- Ability to phase up and sum up to 61 antennas signals
- Capability for real-time assessment of phasing performance
- Ability to apply rapid phase adjustments based on data from water vapor radiometers
- $\geq 90\%$ phasing efficiency

The beamforming component of the APS analyzes the visibilities from the correlator to compute phase adjustments to the individual antennas, which allows the formation of coherent sum signals. APS is managed by a Phasing Controller, that directs the correlator hardware to make phasing adjustments based on calculations made in the Telescope Calibration System (TelCal), which provides all online observatory calibration process. Figure 3.4 presents a general data flow diagram for VLBI observations with phased ALMA.

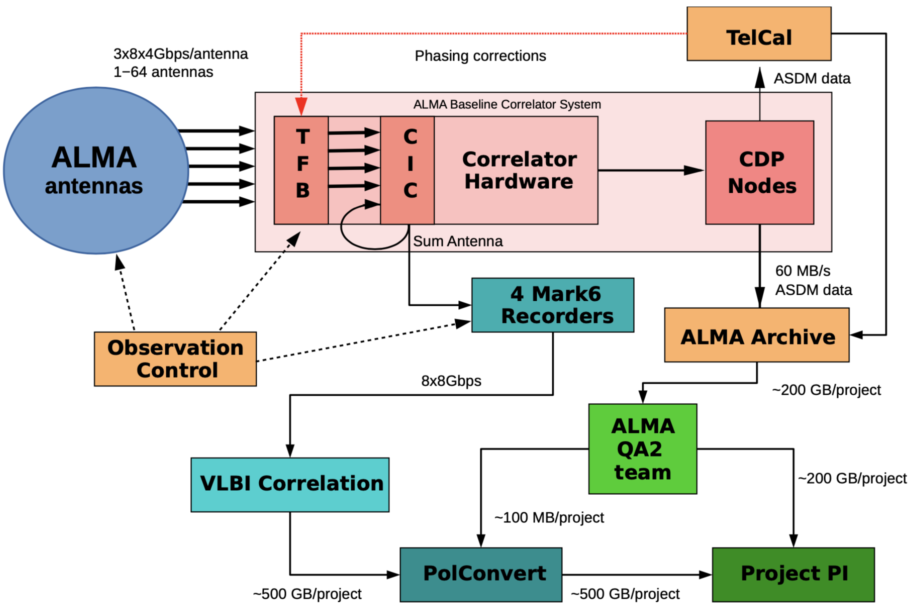

Figure 3.4: *Flow diagram for VLBI observations with phased ALMA. The ALMA correlator receives data from up to 64 antennas, the Correlation Interface Cards (CIC) manufacture the sum antenna signal. At the end of the correlation process, the CDP nodes provide correlated data to the TelCal for calculating the phase adjustments which are then applied and the ALMA correlated data is sent to the ALMA Archive. (Figure from Goddi et al., 2019b).*

Chapter 4

Observations of SgrA* with ALMA

ALMA as a phased array was used during the 2017 campaign of the EHT. The ALMA data alone were used to generate light curves of the target, Sgr A*, and to image it. These image include Sgr A* itself but also the mini-spiral. In this chapter, we will describe the observations made with ALMA as well as the results obtained from these observations.

4.1 Observations

The 2017 EHT observing campaing was scheduled for March and April of 2017. The main targets were M 87* and Sgr A*. Observations of Sgr A* with ALMA were made on April 6, 7 and 11. These observations were made in three different TRACKs that contain the data of each day with durations between 5 and 9 hours each. Every track is also divided in scans of ~ 17 minutes, each containing the visibilities of the object observed. All the data provided for this work were previously calibrated.

In Table 4.1 we present each TRACK and its characteristics individually: the number of scans, elapsed time, and number of antennas used in each observation day. All these observations have 4 spectral windows with central frequencies of 213, 215, 227 and 229 GHz respectively.

Table 4.1:

TRACK description

TRACK	Date	Observation period (UTC)	Number of scans	Total elapsed time (s)	Number of ALMA Antennas (12 m)
B	April 06 - 2017	08:24:04.3 - 14:33:13.7	24	-	24
C	April 07 - 2017	04:02:42.4 - 14:25:11.5	37	37349.1	35
E	April 11 - 2017	09:00:04.3 - 14:03:13.4	18	18189.1	31

We manipulated the data using the software *Common Astronomy Software Applications* (CASA). At a first sight it seemed that the source showed strong variability when amplitude vs time was plotted. However, the original files have bad data in them that had to be flagged to avoid problems with the following processes. The last scan in TRACK E was flagged because the elevation of the source during the observations was very low so this caused that the data had a lot of bad, very scattered points. The result of this flagging process is shown in Figure 4.1 where the three TRACKs are presented.

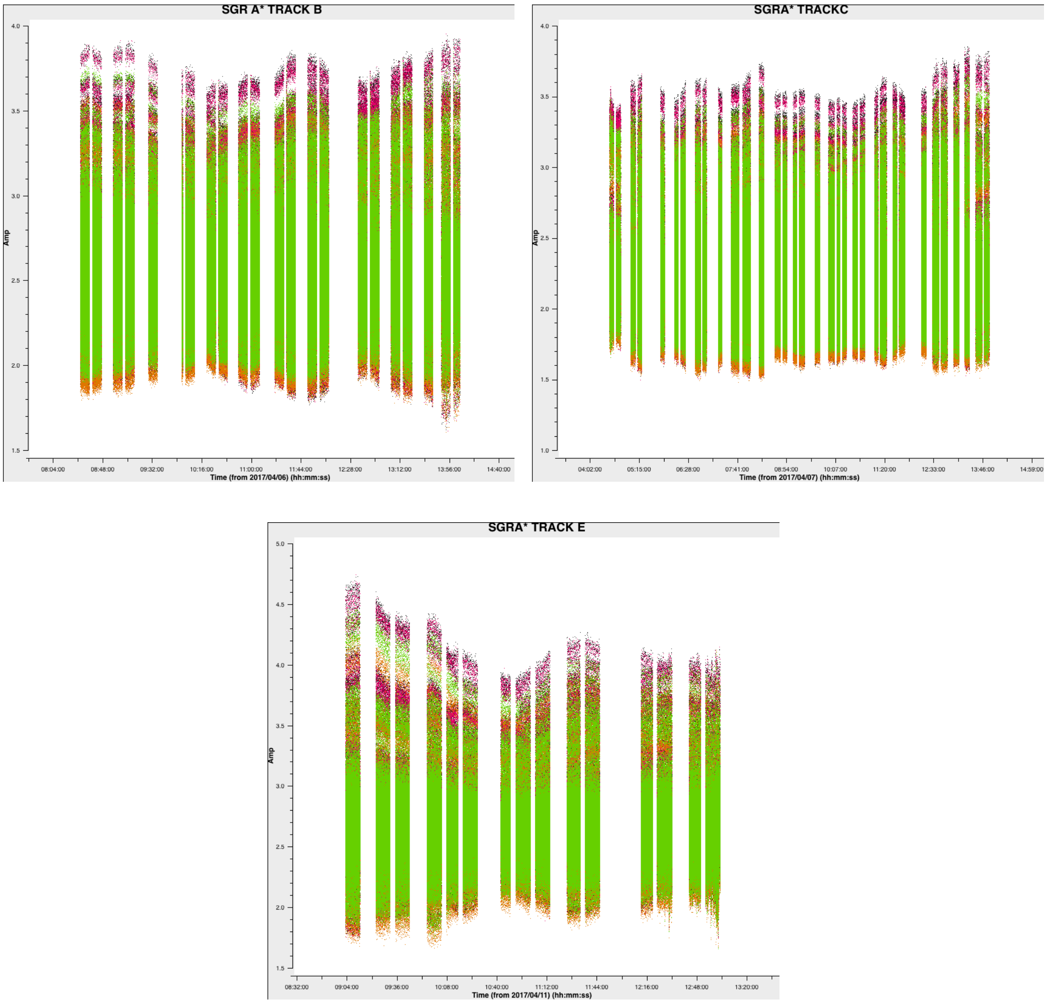

Figure 4.1: *Plots of the amplitude variation in time for each TRACK of observations of SgrA* where we see a first sight of the time variability of the source in a scale of hours. The colors represent the corresponding spectral window. In these plots the data are already flagged.*

More data were flagged in the following process. Figure 4.1 shows the visibilities in different colors to represent each spectral window. We plotted only on the XX and YY correlations (polarizations) because the light of the source is polarized. For practical reasons, we will be rename the scans of each TRACK to analyse the data for light curves later. This re-order in names will be:

- TRACK B: From scan 1 to scan 21
- TRACK C: From scan 22 to scan 53
- TRACK E: From scan 54 to 68

4.2 Imaging compact emission

4.2.1 Extended and compact emission in images

At the spatial scales probed by ALMA, two components contribute to the emission: Sgr A* itself and the mini-spiral. These two components occur at different spatial scales and can be separated in the plot of amplitude versus uv distance.[1] To illustrate this point, consider a source with an intensity that varies with radius as shown in left panel of Figure 4.2. The size of the source is proportional to d. The amplitude vs. uv distance plot is the Fourier conjugate of the intensity vs. radius plot. Thus, the plot showing amplitude vs. uv distance will have the shape shown in the right panel of Figure 4.2, with a width F_d proportional to $1/d$.

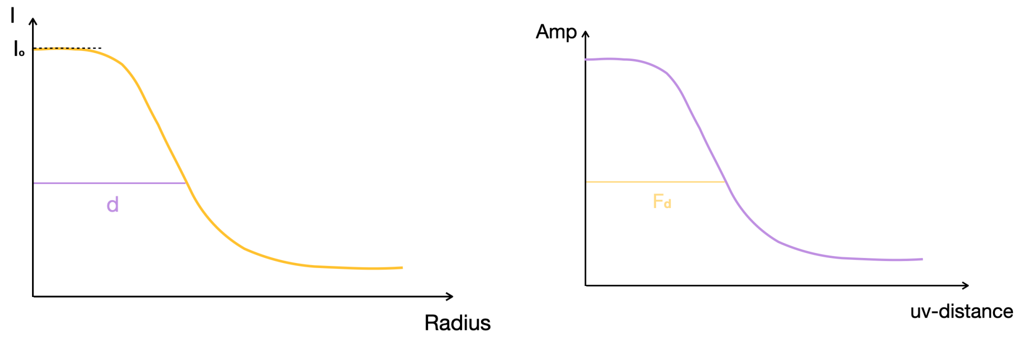

Figure 4.2: *Representation of intensity-radius distribution of the source (left) and amplitude-uv distance relation, it let us to know the range of compact and extended emission from the source.*

If the value of F_d is big, then the source is punctual or has compact emission, and if F_d is small then the source is emission. An extended source will be seen only on short baseline, while a compact source will be detected on all baselines, including long ones. Indeed, a constant amplitude as a function of the uv distance represents a point source, unresolved by the array. Figure 4.2 represents a source that has both types of emission: at long baseline, we see a constant (non-zero) amplitude that corresponds to compact emission. At short baseline, we see an excess of emission due to extended emission. This example shows how extended and compact emission can be separated in a plot of amplitude vs. uv distance.

In the case of Sgr A*, it is knows that the central compact source is variable, whereas the mini-spiral is not. Thus, it is convenient to separate the emission from the two components in order to build the light curve of Sgr A* itself. For this, we used the `tclean` task in CASA to get the image of the compact source alone using an argument that allows us to obtain only the long baselines contribution.

The task `tclean` forms images from visibilities and reconstructs a sky model. The principal arguments used in this task are related to the specifications of the image that is deconvolved. In this case, the arguments used were:

[1] The uv distance is the separation between the antennas in the array in units of wavelengths.

```
tclean(vis, specmode, deconvolver, imsize, cell, weighting, uvrange)
```

The meaning of the arguments is the following. The input visibilities file to apply the task is defined by `vis`; `specmode` is the spectral definition mode; `deconvolver` is the name of the minor cycle algorithm, each of the algorithms operate on residual images and psf's from the gridder and produce output model and restored images; `imsize` is the number of pixels in the image deconvolved; `cell` is the cell size; during gridding of the dirty or residual image, each visibility value is multiplied by a weight before it is accumulated on the uv-grid, the PSFs uv-grid is generated by gridding only the weights (weightgrid), and this scheme is given by `weighting`; and the last one, `uvrange` refers to the process to get only a subset of baselines.

4.2.2 uvrange setting

The selection of the appropriate *uvrange* to select only the compact emission was based on a plot of amplitude vs uvdist, made in CASA (Figure 4.4). With the help of the casa logger and the zoom tool, I looked for the value of the *uv* distance beyond which the flux remains constant. I found that the smooth function started to behave as a constant function at about 86.8 m. From this, I generated test images for different uvdist values (50, 80 and 100 m) to see which enabled me to best recovers only the compact emission. Figure 4.3 shows the comparison of the resulting images for scan 34 (TRACK C) for uvrange=$'> 80\text{m}'$ (left panel) and uvrange=$'> 100\text{m}'$ (right panel).

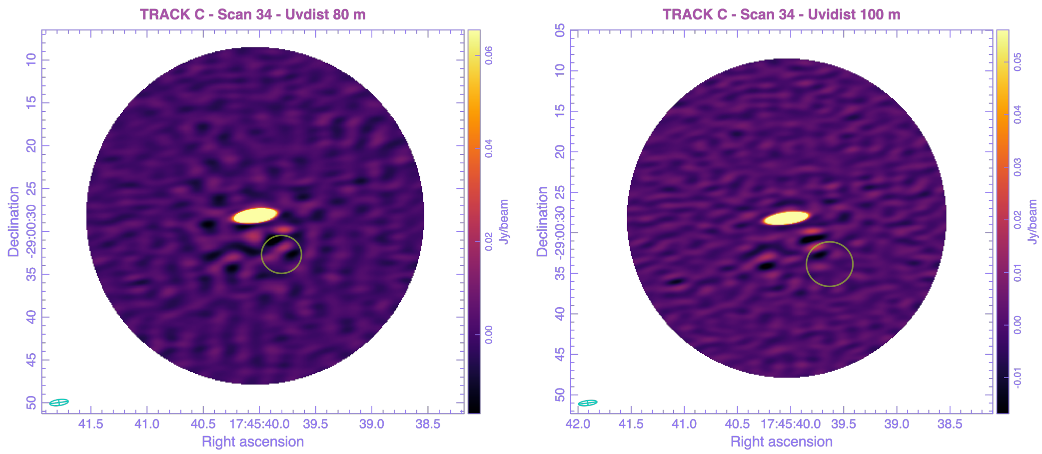

Figure 4.3: *Image of the compact source for scan 34 in TRACK C with two different values for uvrange in the task* `tclean`*: greater than 80 m (left) and greater than 100 m (right panel). The pink circular box is the region where statistics for noise were obtained.*

At first sight in the images, it is seen that the noise is greater in the left panel than the right one. To select the best value all the statistics from both images were taken to compare the peak flux of the compact emission and the RMS value in a region (pink circular box in Figure 4.3) selected in the same position for both images. Table 4.2 present the values obtained for each image.

Table 4.2:

Statistics values for scan 34 TRACK C image			
	Noise		Compact emission
unvrange (m)	Flux Density (mJy)	RMS (mJy)	Peak flux (Jy/beam)
> 80	6.459	10.16	2.251
> 100	1.667	7.25	2.258

Analysing the values in Table 4.2, it is found that the peak flux is greater in the second image, that means that the flux from the compact emission is better recovered with this corresponding uvrange value. But the most important parameter to select the best uvrange value is the RMS. A low value is preferable to obatin a good signal to noise ratio. Comparing both RMS results, the lower is obtained with uvrange='$>$ 100m', this is sustained also with the flux density for this region. As a result of these tests, we decided to use uvdist of 100 for all TRACKs. In Figure 4.4 the red arrow shows the uvdist value selected for the images to calculate the light curves of Sgr A*.

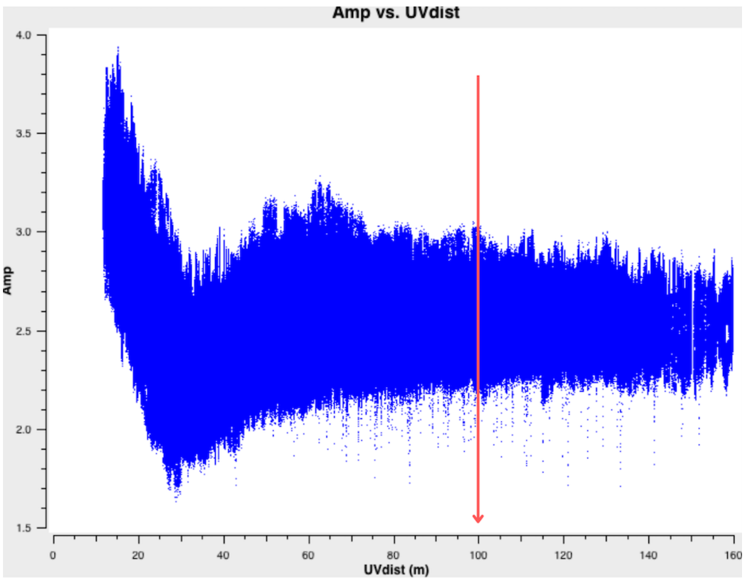

Figure 4.4: *Amplitude vs. uvdist plot for TRACK B, the red arrow shows the uvdist 100 m used to recover only the flux from long baselines. In this plot, we see that at small values of the uv distance, emission associated with extended emission is detected. Starting at $\sim$ 80 m this contribution declines and at 100 m, the emission is due compact emission only.*

4.2.3 Compact emission images

To run `tclean` we used also a mask to specify where clean components should be searched during the deconvolution process. This is justified because it is reasonable to assumed that the compact emission will not change in position during the observations (at the scales probed by ALMA). In Figure 4.5 I show the position of the mask on top of a map of the compact emission.

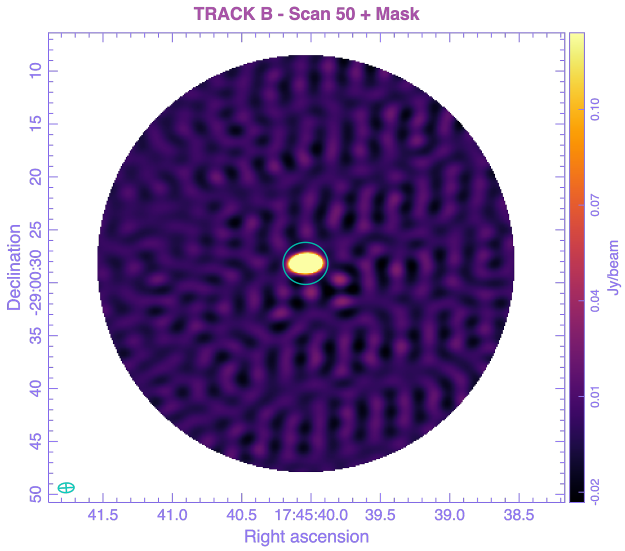

Figure 4.5: *Image of the compact emission in one scan showing the position of the mask used during the tclean process and for the flux measurements.*

.

Once the mask was defined, we created images of the compact emission for each scan in each track. The input parameters used for `tclean` with a mask in a non interactive process were:

- `specmode = 'mfs'`
- `deconvolver = 'hogbom'`
- `imsize = '420'`
- `cell = '0.122 arcsec'`
- `weighting = 'superuniform'`
- `robust = '0.5'`
- `niter = 200`
- `uvrange = '>100'`

Some images of the results from each TRACK are presented in Appendix A. In this section only results from TRACK B are shown in Figure 4.6; there are 6 images from 6 different scans of the complete set of scans. The difference in structure of the images is due to the changing beam, not to the variability of the source.

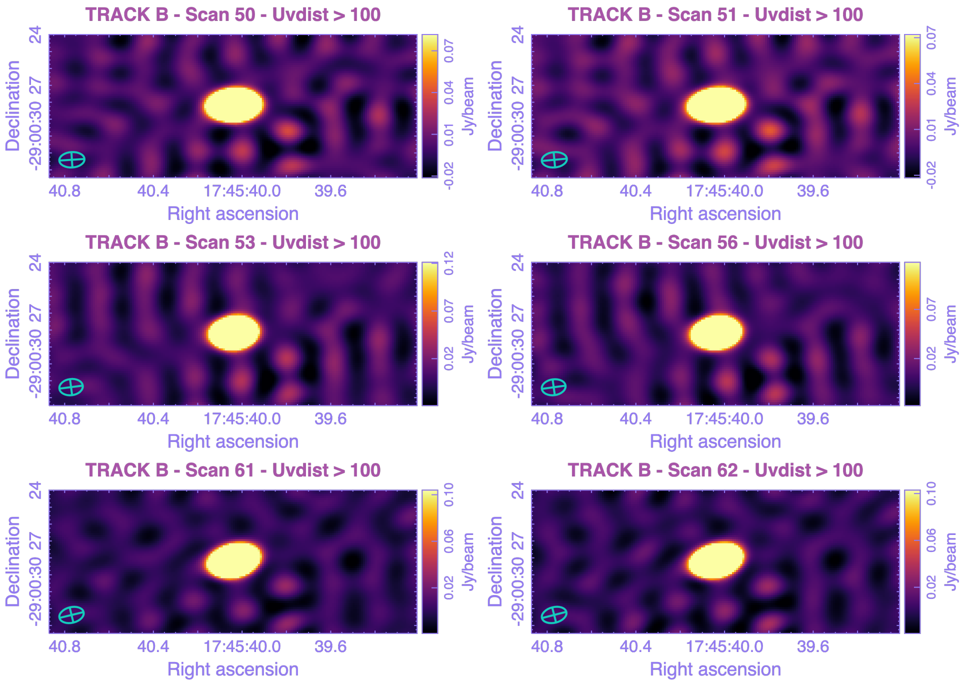

Figure 4.6: *Images of compact emission from scans 50, 51, 53, 56, 61 and 62 from TRACK B*

4.3 Light Curves

A light curve is a graph that shows the flux variation of a source in a period of time; for our purpose this tool is used to analyse the time variability of the compact source structure. This implies to get the peak flux and integrated flux of the source at different times. In all TRACKs of observation the data are divided in scans that represents segments of time. We measured the flux in each scan individually.

Using the mask created for deconvolution process and the 2D Gaussian fitting tool from CASA theses fluxes were computed. With a script written in `phyton` and using the task `imfit`, the peak and integrated flux were computed for each scan. `imfit` also provides errors on the peak and integrated fluxes. The results were stored in a table with the following information: scan, peak flux, peak flux error, integrated flux, integrated flux error, and position. This information allowed us to plot the light curves of Sgr A*. The complete tables with these values are presented in Appendix C.

The following figures correspond to each TRACK light curve. Recall that these observation scans are renamed for the purpose of a better presenting of light curves; they are not the original scan numbers recorded during the observations. Sgr A* was observed every morning in lapses of time of 6, 10.5 and 5 hours on April 6, 7 and 11 (respectively, TRACK B, C and E). Figure 4.10 presents the complete time of observation for Sgr A* as part of the EHT observations.

For TRACK C and E, zoom showing only the maximum values are presented on Figures 4.11 and 4.12, respectively, to reveal more clearly the flux variability in time scales of hours.

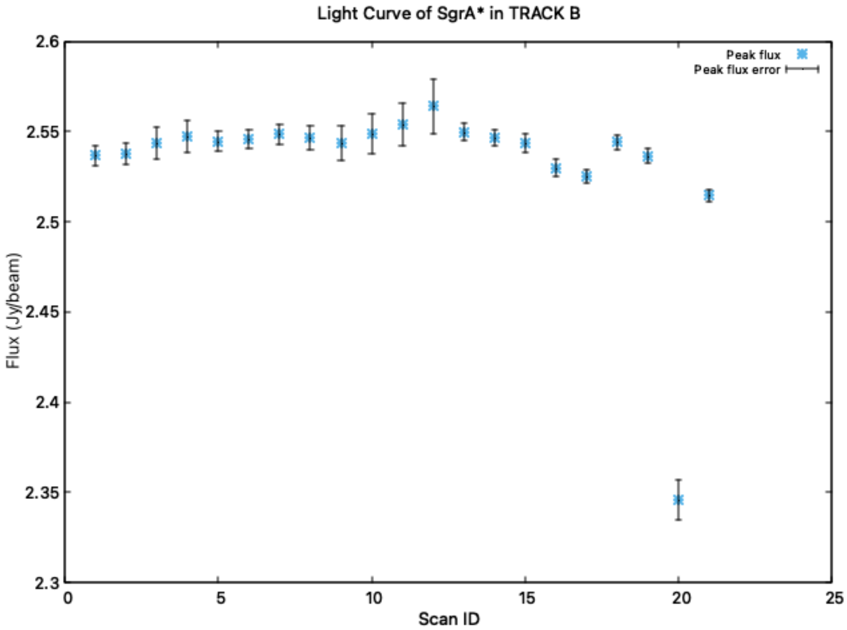

Figure 4.7: *Light curve of Sgr A* compact emission for TRACK B. The total observing time is 6 hours on April 6 2017.*

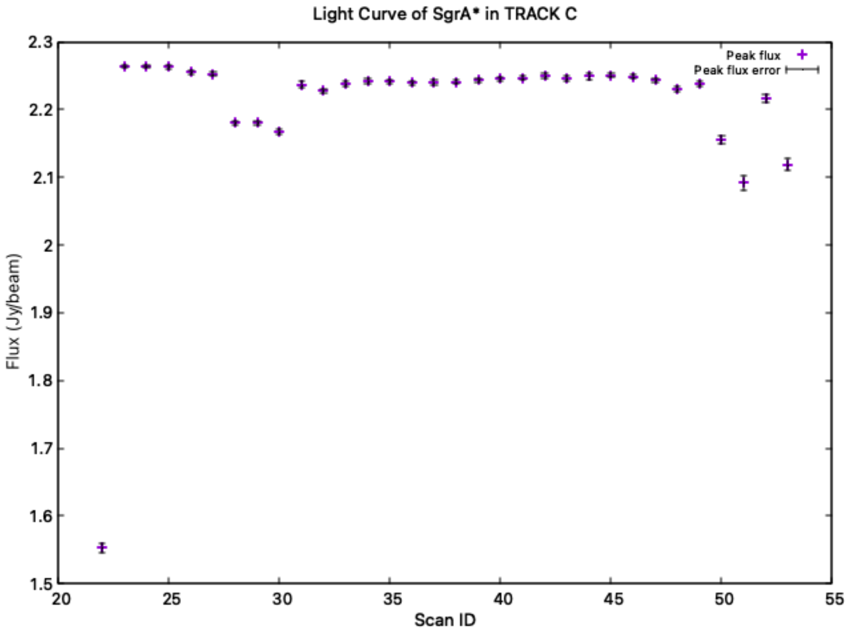

Figure 4.8: *Light curve of Sgr A* compact emission for TRACK C. The total time of observation is 10.5 hours on April 7 2017.*

Only moderate variability is seen during each individual track. The lower fluxes seen at the end and/or the beginning of each track is almost certainly the consequence of atmospheric losses due to the low elevation during these portions of the observations. The lower flux observed during three consecutive scans (28 to 30) of track C is most likely the result instrumental or calibration issues. Aside from these,

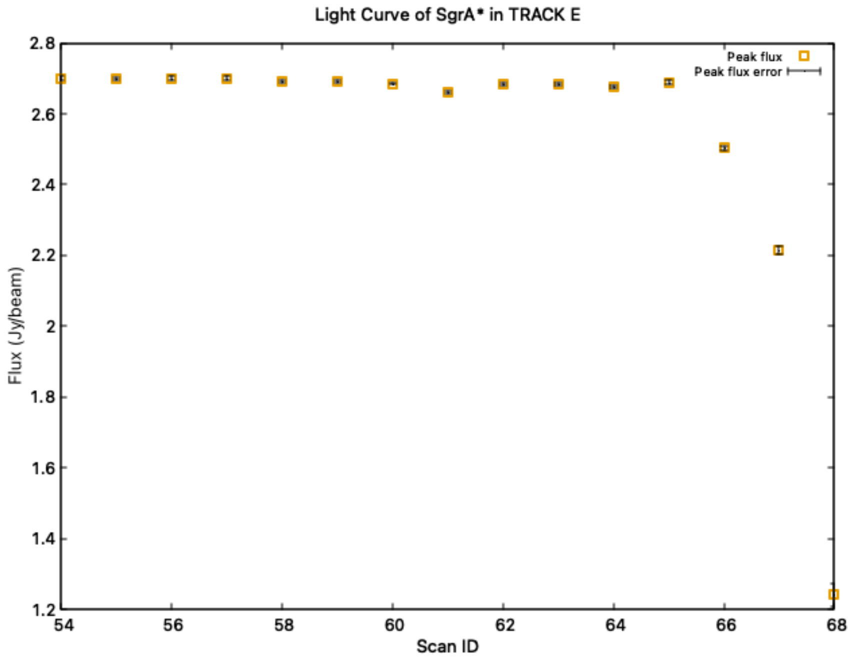

Figure 4.9: *Light curve of Sgr A* compact emission for TRACK E. The total time of observation is 5 hours on April 11 2017.*

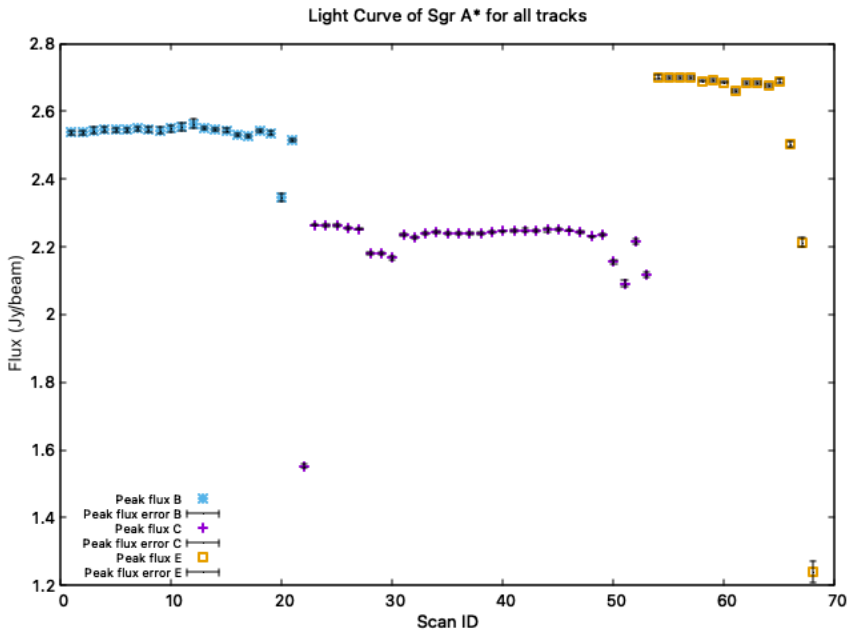

Figure 4.10: *Light curve of Sgr A* compact emission for all TRACKs. The total time of observation is 21.5 hours in 3 different days of observation. Each TRACK is presented in a different color.*

we do see some evidence of intraday variability at the level of a few percent

Figure 4.10 give us a better picture of the complete observation 2017 campaign for Sgr A*. The flux during the first day the flux is clearly greater than during

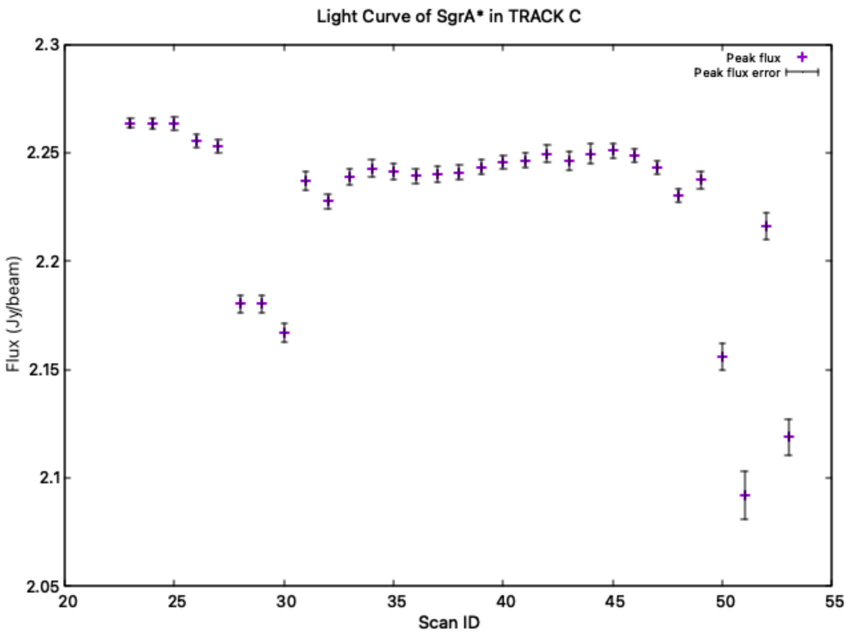

Figure 4.11: *Zoom on maximum values of peak flux for TRACK C.*

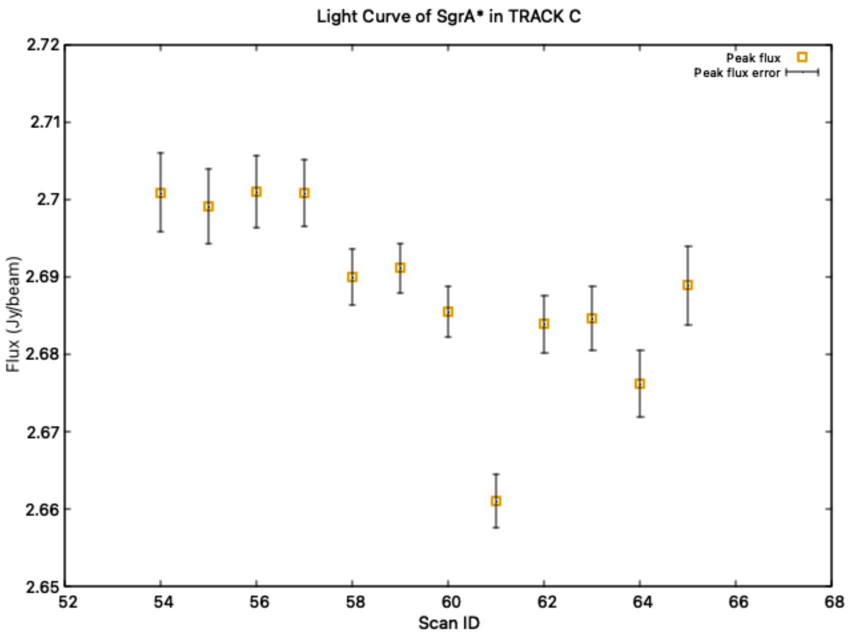

Figure 4.12: *Zoom on maximum values of peak flux for TRACK E.*

the second day while the flux was highest during the last day. Overall, there is variability at the level of about 20% over the entire dataset.

Chapter 5

ALMA as a phased array: phasing efficiency

A phased array is a set of individual antennas, each with an effective area A_{eff}, combined so as to produce a larger effective aperture. This is done by summing coherently the received signals from the individual antennas, adjusting the phase and delay of the signal from each antenna to compensate for the different geometric paths. This procedure turns ALMA into a virtual equivalent single dish antenna of 84-m diameter.

This chapter will briefly describe the fundamental theory of phased arrays and phasing efficiency. It also will describe ALMA as a phased array for the Event Horizon Telescope and how the effect of the extended emission associated with the mini-spiral around Sgr A* on the phasing efficiency was estimated.

5.1 Phased arrays as VLBI elements

Using phased arrays as elements of a bigger interferometer like VLBI is important for two principal reasons. The first is that it reduces the cost by eliminating the need to build a very large dish; instead arrays of smaller antennas are used. The second is that, because of their combined large collecting area, phased arrays increase the signal to noise ratio.

In a phased array, the signals from each antenna are adjusted to compensate for the delay between their arrival time from a specific direction in the sky to each one of the antennas. The corrections are made relative to a reference antenna; the phased signals are summed within the correlator. The better the corrections, the higher the efficiency of the phased array, and the better the sensitivity. This summed signal is recorded on the VLBI recorder, and sent for correlation together with the signals from all the other telescopes in the VLBI array.

To reach the highest sensitivity, the voltages of the individual antennas must be summed coherently:

$$V_{sum} = (V_1 + V_2 + ... + V_{N_A})$$

The output voltage at each antenna is the sum of the signal s_i and noise voltages ϵ_i. Thus, the sum voltage can be written as:

$$V_{sum} = \sum_i (s_i + \epsilon_i) \tag{5.1}$$

The power level of the combined signals over all antenna pair is represented by the average of the squared value in equation 5.1. Expanding the products, we obtain:

$$\langle V_{sum}^2 \rangle = \sum_{i,j} \left[\langle s_i s_j \rangle + \langle s_i \epsilon_i \rangle + \langle s_j \epsilon_i \rangle + \langle \epsilon_i \epsilon_j \rangle \right] \tag{5.2}$$

Let us consider an array of N_A identical antennas distributed each with a system temperature T_{sys} and antenna temperature T_A. For this, we have that $\langle s_i \rangle = \langle \epsilon_i \rangle = 0$ and $\langle s_i^2 \rangle = T_A$ and $\langle \epsilon_i^2 \rangle = T_{sys}$.

If the output signals of the antennas are combined without phasing, then $\langle s_i s_j \rangle = T_A$ for $i = j$ and $\langle s_i s_j \rangle = 0$ for $i \neq j$. This is because the combined signals are not in phase. For the same unphased array we have $\langle \epsilon_i \epsilon_j \rangle = 0$ and $\langle s_i \epsilon_i \rangle = 0$ because $\langle s_i \rangle = \langle \epsilon_i \rangle = 0$. In a phased array, hoever, we have $s_i = s_j$ and we can write $\langle s_i s_j \rangle = T_A$, considering an unresolved source.

Thus, the power levels of a phased and unphased array are, respectively:

$$\langle V_{sum}^2 \rangle = n_a^2 T_A + n_a T_S \quad \text{Phased} \tag{5.3}$$

$$\langle V_{sum}^2 \rangle = n_a T_A + n_a T_S \quad \text{Unphased} \tag{5.4}$$

The corresponding signal-to-noise (snr) with and without phasing are:

$$snr_{phased} = \frac{n_a T_A}{T_S}, \qquad snr_{unphased} = \frac{T_A}{T_S}.$$

From this, we can see that for a phased system the collecting area is equal to the sum of all collecting areas in the array, while for an unphased system the collecting area is equal to that of a single antenna. It is clearly important to phase the signals for array used as a single station in VLBI.

5.2 ALMA as a phased array into the EHT

5.2.1 Self-Calibration process

A very important process into imaging is calibration. This is the process of determining the net complex correction factors that must be applied to each visibility in order to make them as close as possible to what an idealized interferometer would measure, such that when the data is imaged an accurate picture of the sky is obtained. For calibration process a source located near the target (and known as the calibrator) is used as model; this source has well known properties as the flux density, structure, position, etc. Starting from this, we introduce another technique with the same principles: self-calibration.

For a high signal to noise detection, the target itself can be used to calibrate the phases and amplitudes of the visibilities as a function of time. This technique is called self-calibration, and it takes advantage of the fact that, for interferometer with large numbers of antenas, the system of equations to be solved during the caliration processed is over-determined (i.e. there are more equations than unknowns). Once a model image of the target has been reconstructed from initial calibration of the data, one can use the target data themselves to improve the calibration.

This process is iterative. As mentioned above, it starts with a model of the source generated with `tclean` from the initial calibration. This model is used to determine the gains with `gaincal` and the solutions are applied to the data, which are then re-imaged. This process can be repeated as needed. Typically, only the phase is self-calibrated during the first iteration(s). After that, self-calibration of the amplitude is performed.

5.2.2 Phase-only Self-calibration

Using the data set previously calibrated and flagged, I focused first on phase self-calibration on short-timescales. This was applied on the entire uvrange in the data to reconstruct both the compact emission from Sgr A* and the extended emission from the mini-spiral. In Appendix B we present a diagram flux of the calibration and self-calibration process. The self-calibration was performed on the measurement set after flagging each track, using a script written in `python`.

The first step is creating an image of the source with `tclean` to use it as the source model (Figure 5.1). The parameters used are almost the same as in Section 4.2.3 but without using the mask, so the extended emission from the mini-spiral is recovered too. Then the `gaincal` task is applied. This important parameters of this task during this step are the following:

```
gaincal(vis, caltable, field, solint, calmode, refant, gaintype).
```

Here, *caltable* is the output gain calibration table; *solint* the solution interval; *calmode* is the type of solution (phase, amplitude or both); and *refant* is the reference antenna.

The gain calibration table contains the corrections made to the gains for phase in the iteration that is in execution. The reference antennas were selected by plotting the antenna distribution for each TRACK and choosing one near the center of the array. Figure 5.2 shows the antenna positions for TRACK B. To calibrate the phase it is necessary to select a reference antenna from which the phases will be measured. For this example, in TRACK B, the selected antenna to use as reference is DA59 because it is close to the center of the distribution.

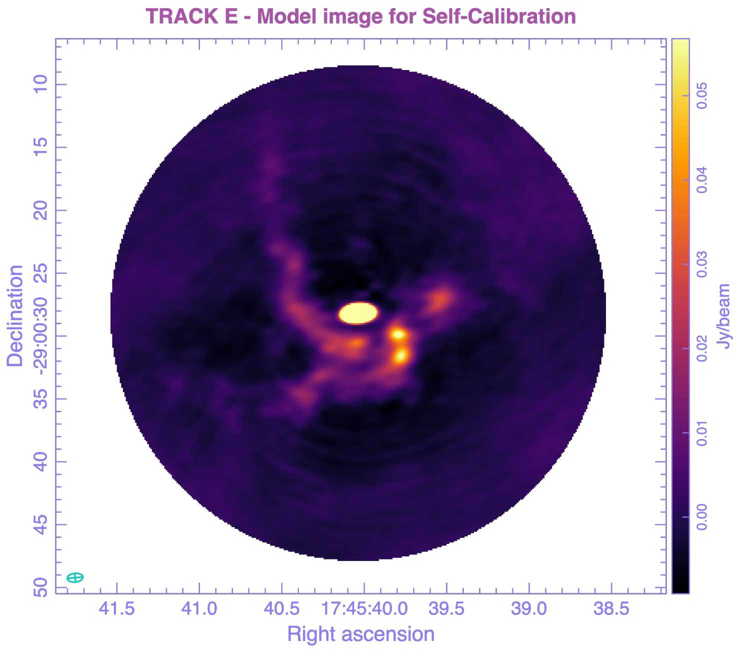

Figure 5.1: *Model image used to self-calibrate the data of TRACK E*

.

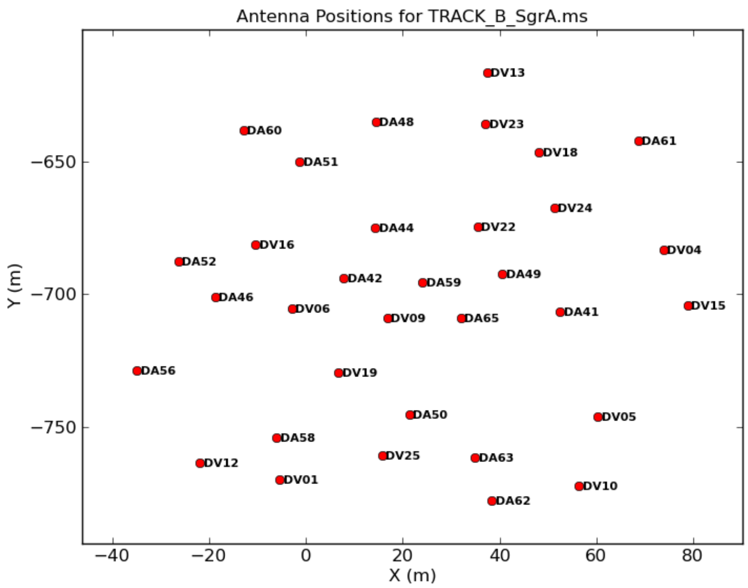

Figure 5.2: *Antennas positions for TRACK B. The reference antenna selected from here is DA59 because it is close to the center of the array*

.

To select the best value for *solint*, we make tests with two different values, 10 s and 20 s. In each case, we measured the flux density of the source and the RMS values. The lower RMS values point to the best solution interval. For this analysis, four iterations of self-calibration were applied to each TRACK with 10 s and 20 s for *solint*. Table 5.1 presents the results obtained from the resulting images.

Table 5.1:

Comparison of the results for solint 10 s and 20 s separated by TRACK				
	solint 10 s		solint 20 s	
TRACK B				
Iteration	Flux density (mJy/beam)	RMS (mJy/beam)	Flux density (Jy/beam)	RMS (mJy/beam)
First	2.439	2.027	2.533	1.909
Second	2.438	1.936	2.533	1.816
Third	2.436	1.948	2.533	1.817
Fourth	2.434	1.949	2.533	1.809
TRACK C				
Iteration	Flux density (mJy/beam)	RMS (mJy/beam)	Flux density (Jy/beam)	RMS (mJy/beam)
First	2.208	1.683	2.228	1.683
Second	2.21	1.629	2.228	1.641
Third	2.211	1.629	2.229	1.636
Fourth	2.211	1.639	2.229	1.638
TRACK E				
Iteration	Flux density (mJy/beam)	RMS (mJy/beam)	Flux density (Jy/beam)	RMS (mJy/beam)
First	2.679	1.312	2.679	1.312
Second	2.679	1.123	2.679	1.125
Third	2.679	1.122	2.679	1.132
Fourth	2.679	1.123	2.679	1.129

From results in Table 5.1 it is noted that the flux density gets higher and quickly reach nearly constant values with *solint* 20 s. Also the RMS values decrease considerably with every iteration for 20 s in comparison with the case where soloint is 10 s. From this analysis, I concluded that the best *solint* value to use in self-calibration data is 20 s (Figure 5.3). In Appendix C all the calibration tables for every TRACK are presented. The reference antennas used for each self-calibration were DA59 for TRACK B and C, and DV23 for TRACK E.

Values for arguments in `gaincal` are:

- `solint = "20s"`
- `calmode = "p" for phase only`
- `refant ="DA59", "DV23"`

5.2.3 Amplitude-phase Self-Calibration

Using the resulting data from the last iteration in phase-only self-calibration, amplitude self-calibration was executed. We only do amplitude calibration at the end of the self-calibration process if there are amplitude-based gain artifacts in the data. Amplitude calibration should be used with caution because it has the potential to change the fluxes in the data.

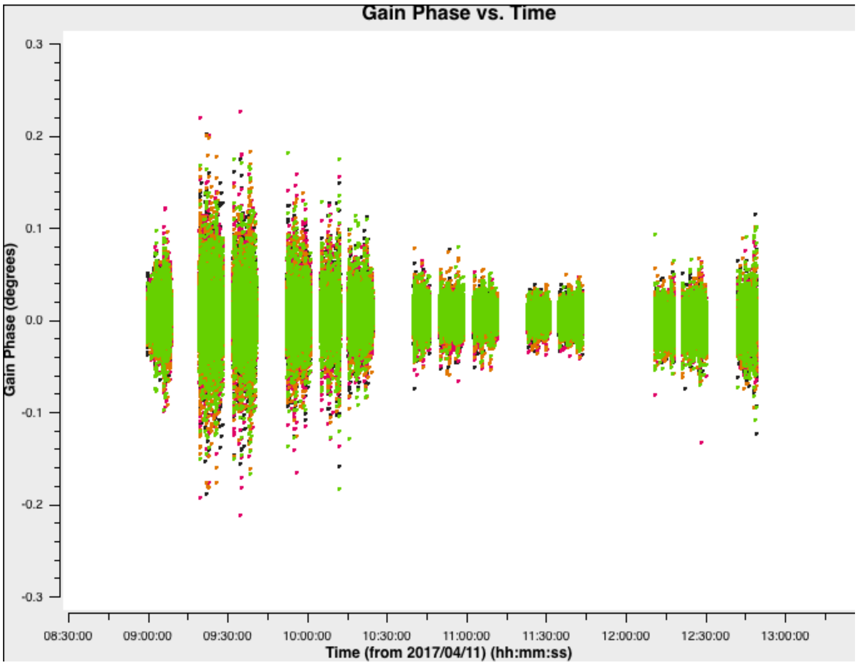

Figure 5.3: *Plot of Gain phase vs. time for the third iteration of phase self-calibration for TRACK E. The phases are centered on zero.*

In this case, I tested with two different solint values for extended emission in amplitude-phase self-calibration. The values for solint used were 60 s and 180 s. Initially, only 60 s iterations were applied but the resulting phases were not centered on zero, and their dispersions were large. For this reason, a test with *solint* = '180s' was used. This showed better results for some iterations in some TRACKs. A discussion for each TRACK is presented below.

TRACK B

Three iterations of amplitude+phase self-calibration were performed for TRACK B, each with a solint of 60 s. Until the second iteration, the phases remained centered on zero (Figure 5.4) but at the third iteration, this phases were compromised. As shown in Figure 5.5, the phase were systematically displaced from zero.

With this solution interval value, the best choice is to use the second iteration to calculate the phasing efficiency.

As seen in both figures, there are some bad data in the scans that show a high dispersion. The last two scans also present bad data because of the low elevation of the source during these observations. These last two scans as well as the other bad data points were flagged before the self-calibration process. These bad data appear in almost every iteration. To solve this, every time a calibration table is applied this table is first opened to flag for bad data points. We then continue with the process of self-calibration.

We encountered a problem, which we beleive to be a bug in CASA, when we tried to repeat the same process with a solution interval of 180 s. The error message

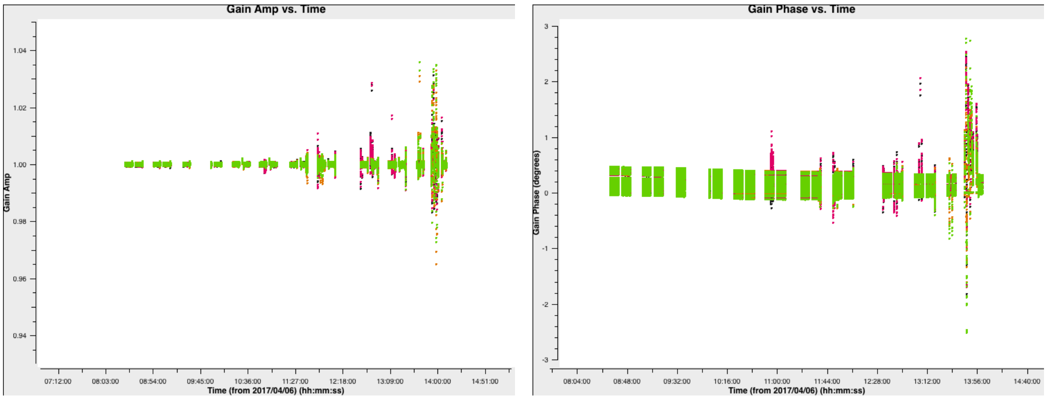

Figure 5.4: *TRACK B second iteration of amplitude+phase self calibration. The left panel shows a plot of amplitude gains vs time; the right panel shows the phase gains vs time.*

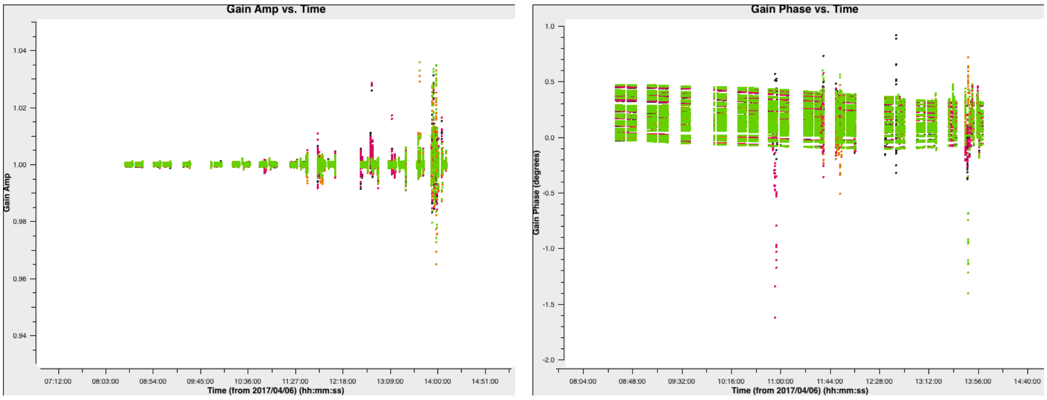

Figure 5.5: *TRACK B third iteration of amplitude+phase self calibration. Plot of amplitude gains vs time (left), and phase gains vs time (right).*

states that the `model_column` cannot be written. As a consequence, for this TRACK there are no results for a longer solint, and the results used for phasing efficiency correspond to `solint = '60 s'`.

TRACK C

For TRACK C, the last 4 scans were flagged because there was a big dispersion in the visibility data. Using calmode ='ap', with solint = '60s' and refant = "DA59", we found 1268 good solutions in the first iteration of self calibration. After the first iteration, I applied a quack flag (task used used to remove data at scan boundaries (`https://casa.nrao.edu`)) to the data for 10 s at the beginning. For scan 15, I flagged the last 3 three timerange because it also showed a high dispersion. For the second iteration, a quack flag of 10 s was applied to the beginning and the end of each scan.

For the second and third iteration we also found 1268 good solutions on the gaincal process. In the last iteration, the third calibration table data looked good, so a few data were flagged with a quack flag for the first and last 20 s. The calibration solutions for the second and third iterations are shown in Figure 5.6 and 5.7.

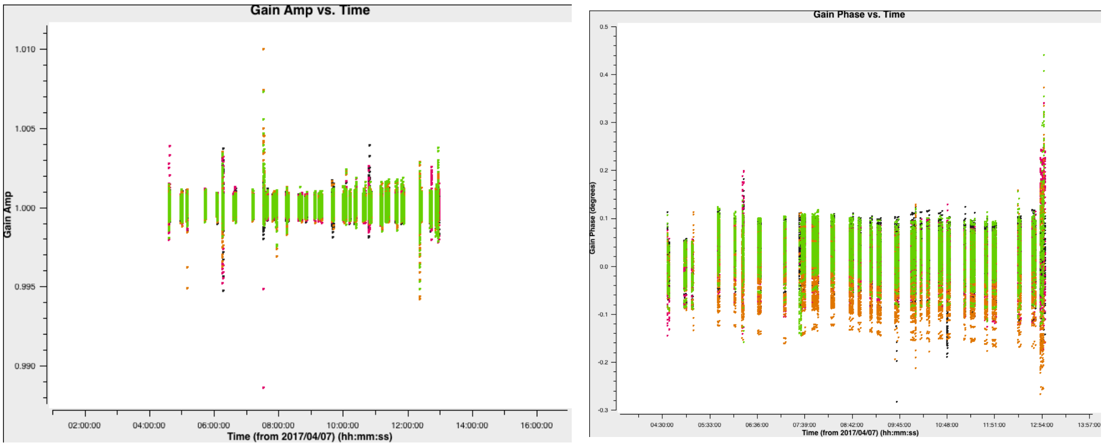

Figure 5.6: *TRACK C second 60-s iteration of amplitude+phase self calibration. Plot of amplitude gains vs time (left) and phase gains vs time (right).*

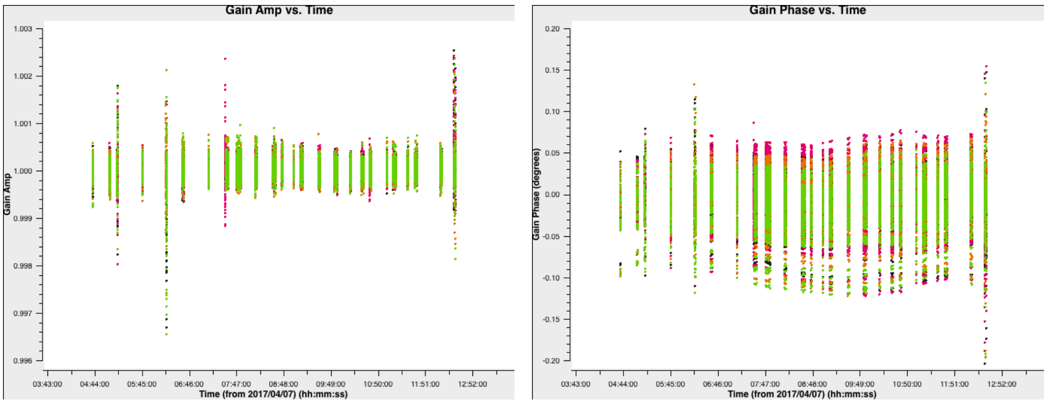

Figure 5.7: *TRACK C third 60-s iteration of amplitude+phase self calibration. Plot of amplitude gains vs time (left) and phase gains vs time (right).*

The third iteration gives really good results with the phase centered on zero. Some bad data are still present, but this is the best version.

The same process was repeated using solint = ’180s’ and the data from phase-only self-calibration with solint 20 s and without the last 4 scans as in the previous amplitude-phase self-calibration. I also used the same values for the antenna reference and calmode. I opened the calibration table obtained at the end of the first iteration and flagged the data in quack mode for the first 10 s of scan 47. For the second iteration, the data were very dirty with high dispersion. As aresult of this, scan 17 was flagged entirely. For the third iteration, I also flagged the first scan. The calibration tables for the second and third iterations are shown in Figure 5.8 and 5.9.

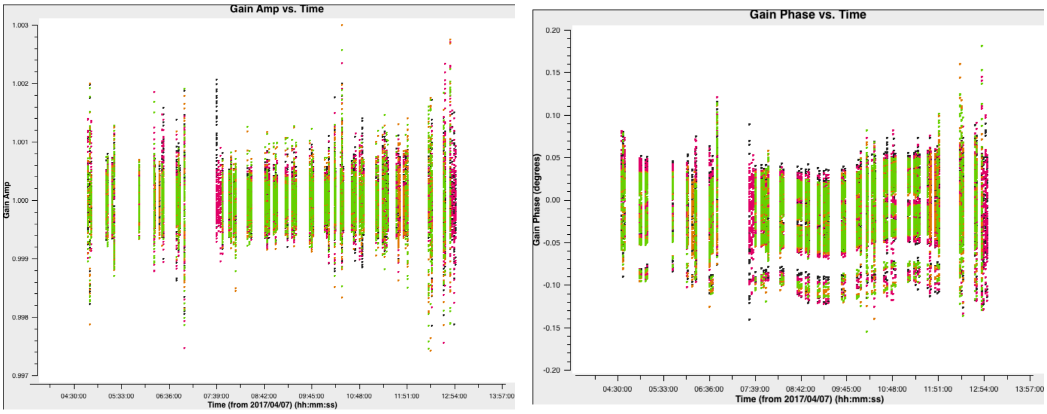

Figure 5.8: *TRACK C second iteration of 180-s amplitude+phase self calibration. Plot of amplitude gains vs time (left) and phase gains vs time (right).*

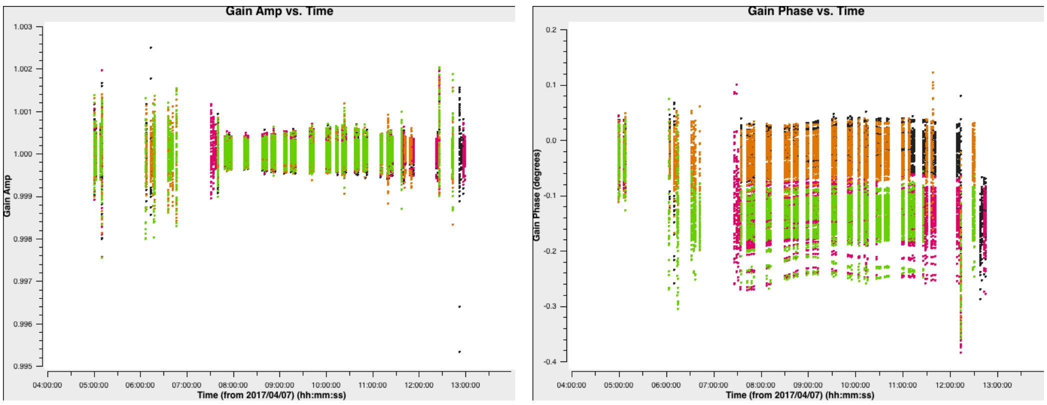

Figure 5.9: *TRACK C third iteration of 180-s amplitude+phase self calibration.Plot of amplitude gains vs time (left) and phase gains vs time (right).*

For this solution interval, the third iteration was very poor, the calibration table for phase gains are systematically displaced from zero, and centered on -0.1 degrees. So the best iteration result for this interval is the second one. And this is the one we will use for the phasing efficiency.

TRACK E

For amplitude-phase self-calibration of the extended emission on TRACK E, we only use solint 180 s because the error about the `model_column` that couldn't be written appeared again. For 18 scans in total, during the first iteration with solint = '180s' and refant = 'DV23', we did not flag data. The output of the casa-logger for gaincal indicated 260 good solution intervals. Were found the same for the second iteration, and for the third iteration some time points were flagged. I flagged also some time ranges because with high dispersion, and scan 76. Results of this calibration tables are presented in Figures 5.10 and 5.11 for the second and third iteration. The second iteration results will be used to compute the phasing efficiency, because the phase in the third iteration is not centered on zero.

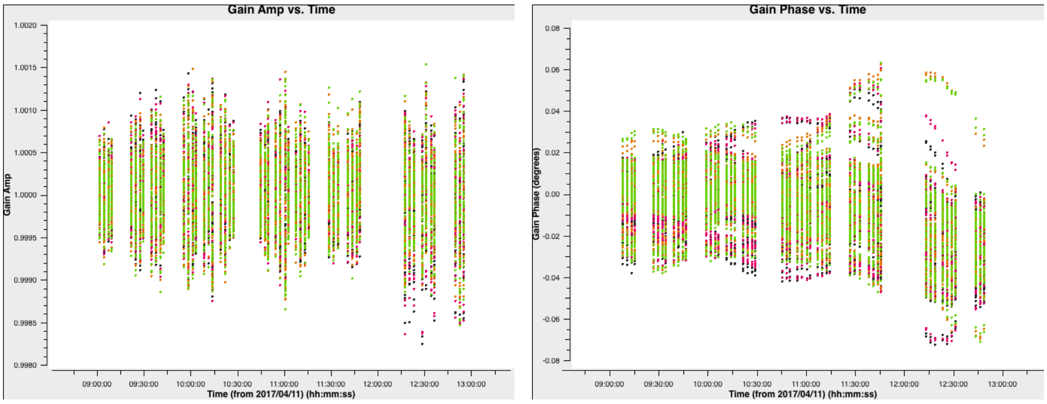

Figure 5.10: *TRACK E solint second iteration of 180-s amplitude-phase self calibration. Plot of amplitude gains vs time (left) and phase gains vs time (right).*

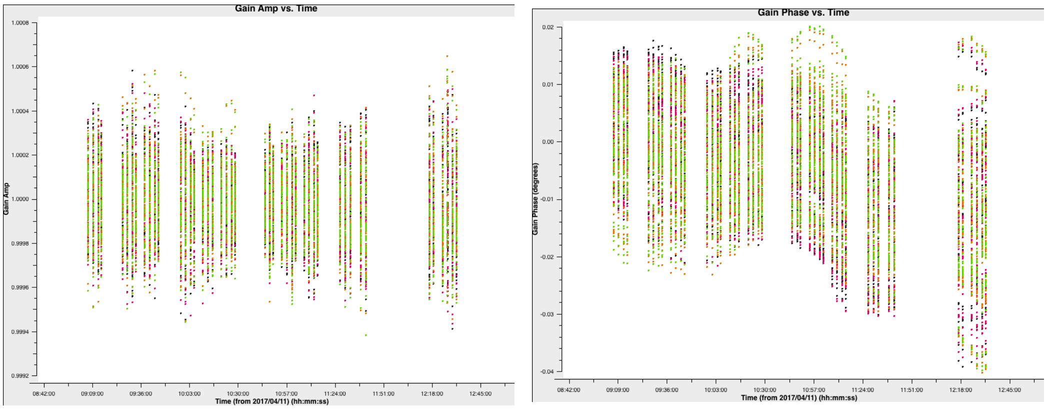

Figure 5.11: *TRACK E third iteration of 180-s amplitude-phase self calibration. Plot of amplitude gains vs time (left) and phase gains vs time (right).*

5.3 Phasing efficiency estimates

The effect of the extended emission on the phasing efficiency will be computed from statistics on the measurement sets before and after self-calibration.

The online ALMA phasing system corrected the phase of the individual antenna signal assuming that Sgr A* is a point source. The existence of extended emission (the mini-spiral) implies that the online corrections were not exactly that should have been applied. The effect of the extended emision on the phasing efficiency can be estimated by comparing the coherent mean of the data immediately after initial calibration to the same mean after self-calibration. Indeed, the initial calibration assumed that Sgr A* is a point source, whereas the images after self-calibration account for the extended emission. Thus, the coherent sum before self-calibration corresponds to what the online ALMA phasing system assumed, whereas the coherent after self-calibration is what should have been used. Their ratio therefore provides a proxy for the effect of the extended emission on the phasing efficiency.

The task `visstats` in CASA returns statistical information about the data in a measurement set. Some arguments have to be defined to specify which data will be statistical analysed. This task returns the results per spectral window so we will have four different data points per scan. The important arguments to be passed on to `visstats` are:

- `axis = 'real', and 'imag'`
- `scan`
- `useflags = True`

All the TRACKs had data flagged during the process of self-calibration, so the number of visibilities at the end is different from that at the beginning. We used argument *useflags* = True to take the flagging into account. Statistical results are computed for two different axes, real and imaginary. From these values, the coherent amplitude sum was calculated using:

$$Amplitude = \sqrt{A^2 + B^2} \tag{5.5}$$

In the following lines I'll present the results for TRACK E, with self-calibrated data from solint 60 s. I ran the task `visstat` in a python script to compute the statistical information per scan in TRACK E, for the four spectral windows defined in Chapter 4, and iterating between real values and imaginary values. This task returns the information as shown in Table 5.2 for each spectral window.

I saved the results of the mean of the values for all the scans per axis. This results are tabulated in a table (Appendix C) that contains: scan, spw, mean value of real part, mean value of imaginary part (both from non self-calibrated data), mean value of real part and mean value of imaginary part for self-calibrated data, which result from equation 5.5 applied to both sets of data.

Plotting the ratio of the coherents sums, I get the effect of the extended emission on the phasing efficiency graph per spectral window for each TRACK (Figure 5.13,

Data Statistics for Scan 68 - TRACK E	
Statistic	Value
Number of points	232308
Mean of the values	-0.00627 Jy
Variance of the values	0.01883 Jy
Standard deviation	0.13737 Jy

Table 5.2: Statistical information about Scan 68 in TRACK E, returned by task visstat applied to self-calibrated data for the imaginary part of the visibility value.

5.14 and 5.15). A value of 1 indicates no loss of efficiency due to the extended emission. Analysing the plots, we see that the phasing efficiency has a low value under 0.98 for TRACK E and reaches up to 1.005. This means that the effect of the extended emission is minimal. Values over 1 are difficult to explain, and we argue that they could be a consequence of the amplitude self-calibration process which, as we mentioned earlier, could affect the absolute flux calibration. Thus, I also plotted the ratio of the coherent sums after the phase-only self-calibration process. The results are shown in Figures 5.16, 5.17 and 5.18.

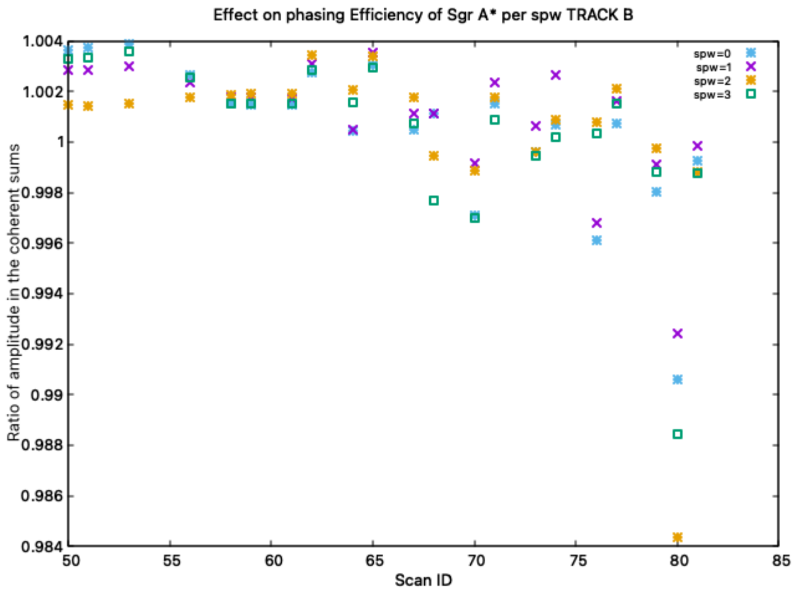

Figure 5.12: *Ratio of coherent sums for TRACK B using solint 60 s in self-calibration process. Each color represents a spectral window.*

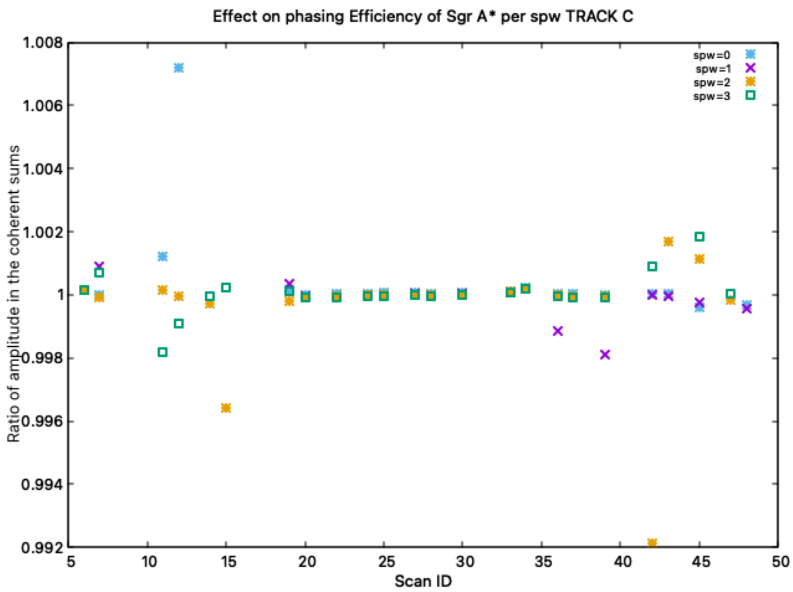

Figure 5.13: *Ratio of coherent sums for TRACK C using solint 180 s in self-calibration process. Each color represents a spectral window.*

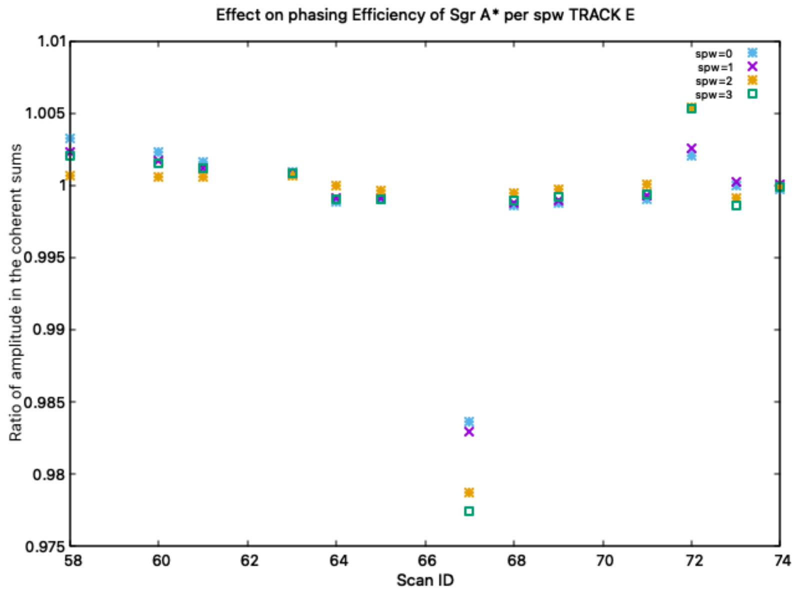

Figure 5.14: *Ratio of coherent sums for TRACK E using solint 60 s in self-calibration process. Each color represents a spectral window.*

In the phase-only plots the ratios of coherent sums are very close to 1. This indicates that the values above one observed after the amplitude+phase self-calibration were indeed likely affected by errors introduced by the amplitude self-calibration. It also shows that the effect of the extended emission around Sgr A* on the phasing efficiency of ALMA during EHT observations is largely negligeable, remaining much below the percent level.

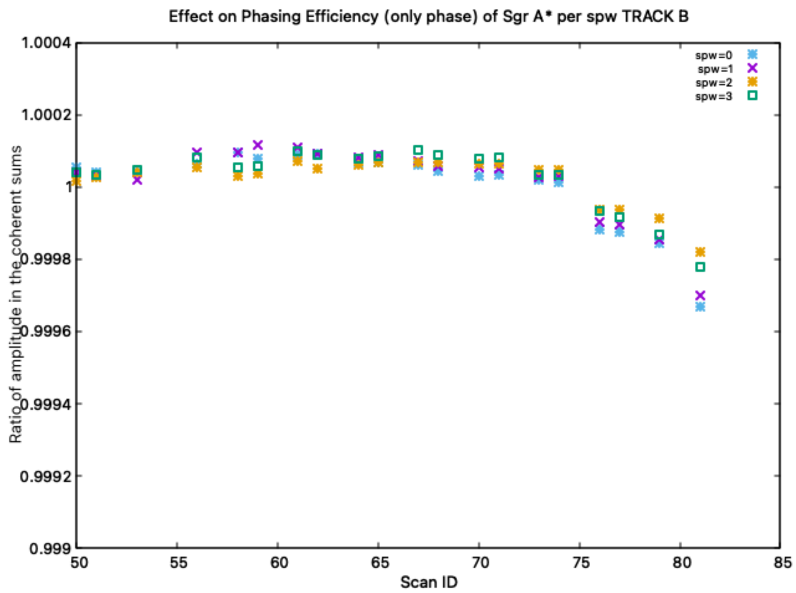

Figure 5.15: *Ratio of coherent sums for TRACK B using solint 20 s in the phase-only self-calibration process. Each color represents a spectral window.*

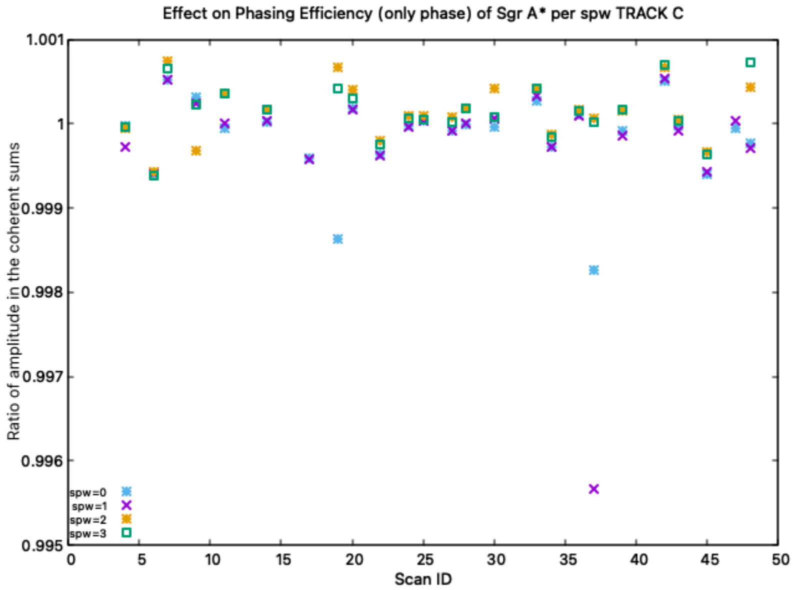

Figure 5.16: *Ratio of coherent sums for TRACK C using solint 20 s in the phase-only self-calibration process. Each color represents a spectral window.*

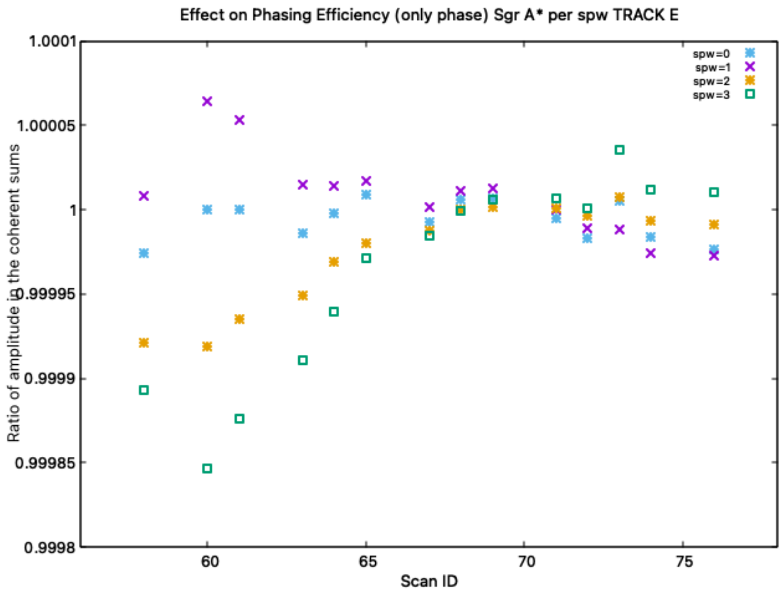

Figure 5.17: *Ratio of coherent sums for TRACK E using solint 20 s in the phase-only self-calibration process. Each color represents a spectral window.*

Chapter 6

Conclusions

This work was based on observations with high angular resolution and sensitivity provided by ALMA as part of 2017 campaign of the Event Horizon Telescope. The combination of high resolution and sensitivity enabled the separation of Sgr A* and the surrounding mini-spiral, as well as the detailed study of the time variability of Sgr A*. Taking advantage of the tools provided by CASA, a very accurate set of images were generated to obtain the light curves of Sgr A*. The light curves obtained in this work confirm the time variability of the source due to the falling of the hot gas into the black hole. This variability is measured on scale from hours to days.

The main goal of this project was to estimate the effect of the (extended) mini-spiral around Sgr A* on the phasing efficiency of ALMA during EHT observations. To achieve this goal, we self-calibrated the observations. The ratio of the amplitudes of the coherent sums of the visibilities before and after self-calibration provides a good proxy for the effect of the extended emission on the phasing efficiency because the former is obtained under the assumption that the emission is punctual, whereas the latter takes the extended emission into account. This works demonstrates that the effect of the extended emission is minimal – well below the percent level.

Appendix A

Images of the extended emission

In this chapter we present the images obtained as a result of the self-calibration process in phase-only and amplitude+phase for Sgr A*.

A.1 Phase-only self-calibration images

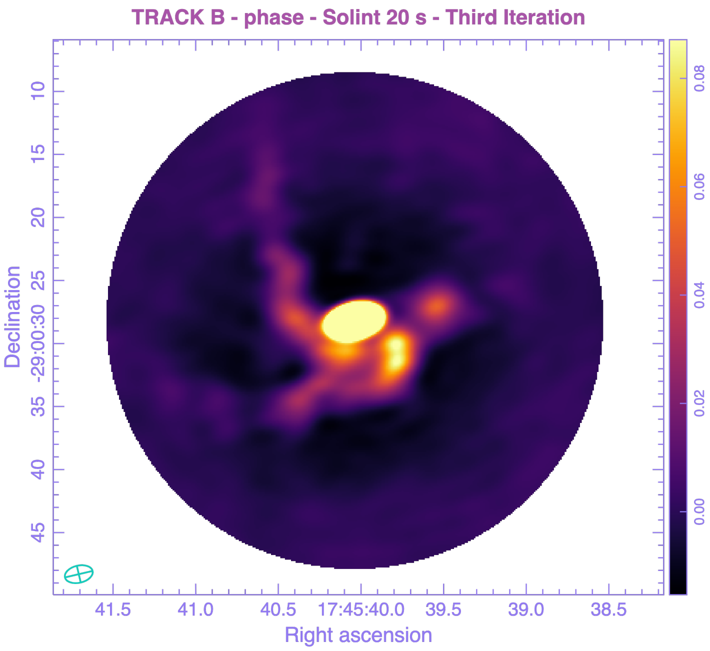

Figure A.1: *Extended emission recovered after three iterations of phase-only self-calibration for TRACK B with a solint of 20 s.*

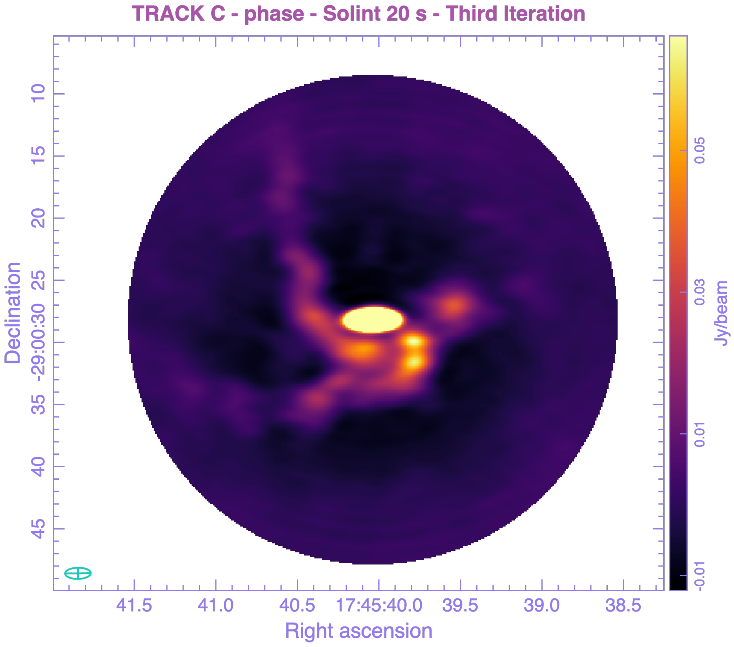

Figure A.2: *Extended emission recovered after three iterations of phase-only self-calibration for TRACK C with a solint of 20 s.*

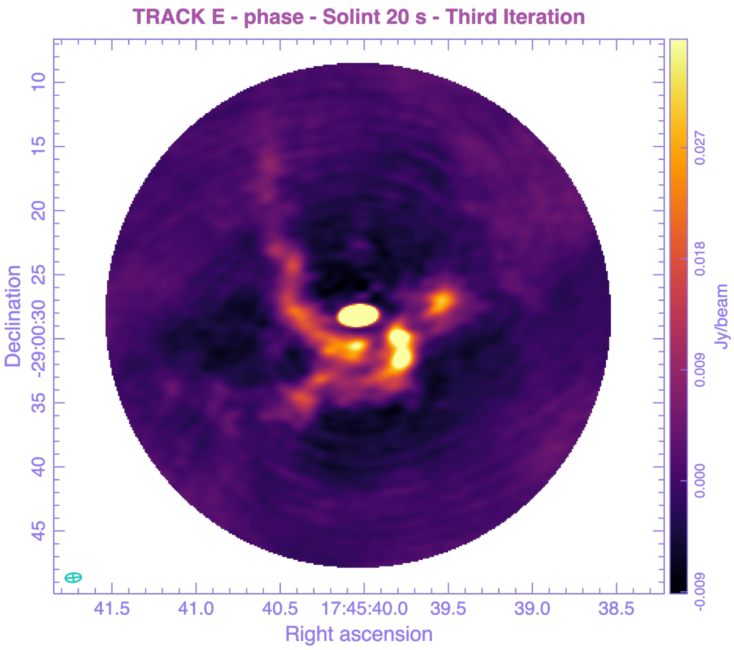

Figure A.3: *Extended emission recovered after three iterations of phase-only self-calibration for TRACK E with a solint of 20 s.*

A.2 Amplitude+phase self-calibration images

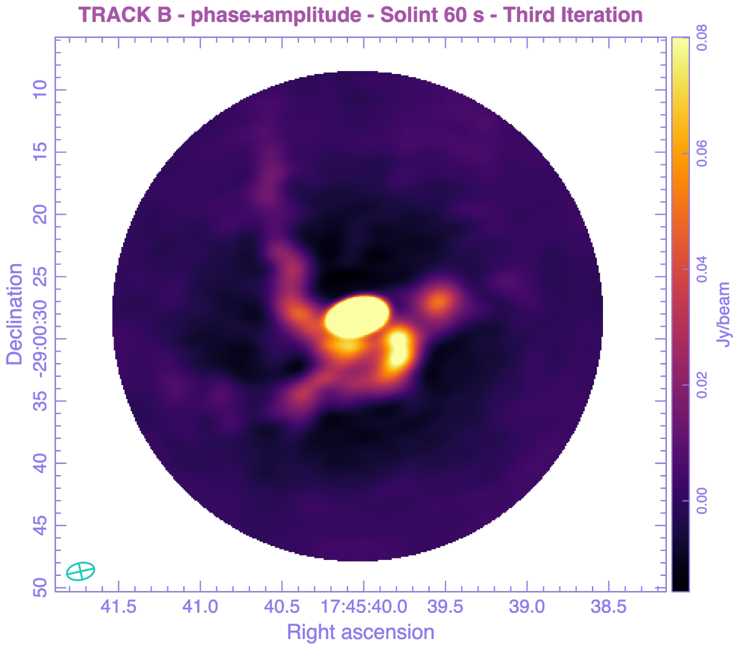

Figure A.4: *Extended emission recovered after three iterations of phase+amplitude self-calibration for TRACK B with a solint of 60 s.*

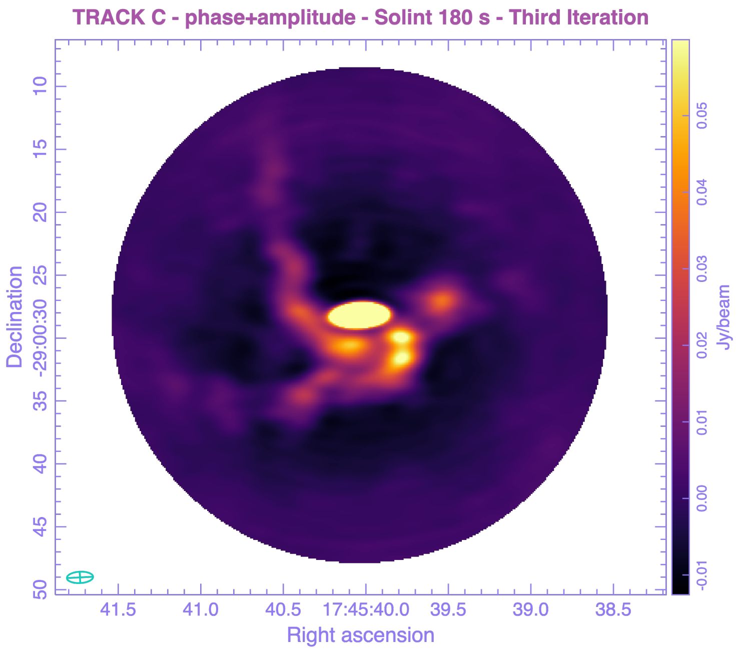

Figure A.5: *Extended emission recovered after three iterations of amplitude+phase self-calibration for TRACK C with a solint 180 s.*

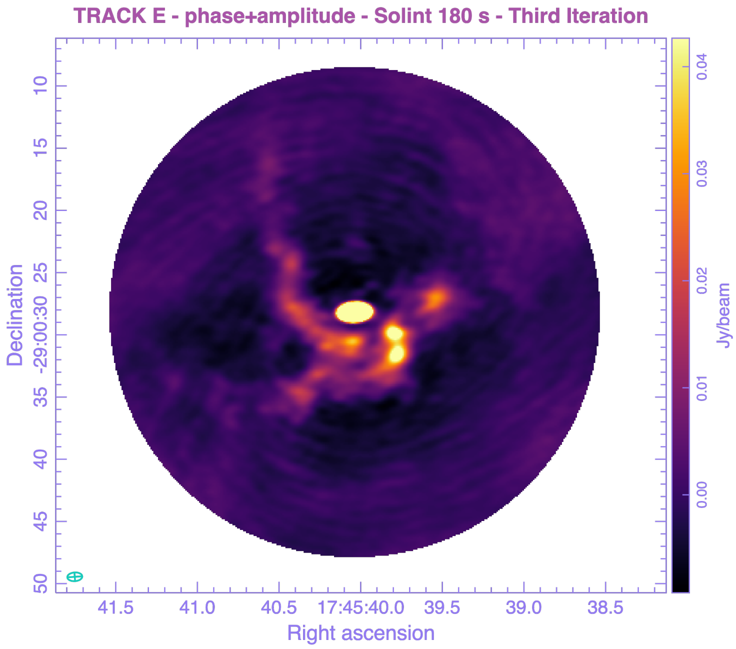

Figure A.6: *Extended emission recovered after three iterations of amplitude+phase self-calibration for TRACK E with a solint of 180 s.*

Appendix B

Scripts

In this section we present the scripts written for the creation of the compact emission images used for light curves and the scripts for phase-only and amplitude+phase self-calibration.

B.1 Script for compact images

In the following, we present the scripts to create the images of the compact emission in Sgr A*. For this, the most important parameters to define were `uvdist` and `weighting`; the values assigned to these arguments were taken by analysis of the plot of amp vs uvdist. This enables us to separate the signal coming from short and long baselines. To recover only the compact emission, this script takes only the long baselines on the array starting at 100 m, and in order to get a smooth cut of the emission the value for `weighting` parameter was taken as superuniform.

B.1.1 TRACK B

```
# Script to create the images of the compact emission for UV dist 100 and using WEIGHTING SUPERUNIFORM
# Corrected in datacolumn, this script uses a mask for the NO interactive process of tclean
#########################################################

import os

# Path to save tables, splits and images
datadir = '/Users/brissa/Documents/SgrAobservations/TRACKB/CompactB/superuniUV100/'

# The mask that will be used for the no interactive step of the tclean process, this is the area for the convolution
Mask = '/Users/brissa/Documents/SgrAobservations/TRACKB/CompactB/superuniUV100/smallermask.crtf'

# MS file flagged for the tclean process
MsName =  '/Users/brissa/Documents/SgrAobservations/TRACKB/CompactB/TRACK_B_SgrA.ms'
```

```
list_of_scans = [50,51,53,53,56,58,59,61,62,64,65,67,68,70,71,73,74,76,77,79,80,81]
for scan in list_of_scans:
        target = 'TRACK_B_SgrA_comp_suniUV'+str(scan)
        TargetField = '0'
        SpecWin = '0,1,2,3'
        TargetSplitFile = datadir+target+'.split'
        TargetImage = datadir+target+'.image'

        # Parameter for tclean process, remember that this script has the goal of smooth the cut so it will be used the superuniform weighting
        CellSize = '0.122arcsec'
        NiterCal = 200
        NiterTarget = 500
        imsizeTarget= 420

        os.system('rm -rf '+TargetSplitFile)
        split(vis=MsName, outputvis=TargetSplitFile, datacolumn='data', field=TargetField, spw=SpecWin, scan=str(scan))

        os.system('rm -rf '+TargetImage+'*')
        tclean(vis=TargetSplitFile, imagename=TargetImage, specmode='mfs', deconvolver='hogbom', imsize=imsizeTarget, cell=[CellSize], weighting='superuniform', interactive=False, niter=NiterCal, mask=Mask, uvrange='>100')
```

B.1.2 TRACK C

```

# Script to create the images of the compact emission for UV dist 100 and using WEIGHTING SUPERUNIFORM
# Corrected in datacolumn, this script uses a mask for the NO interactive process of tclean
#################################################

import os

# Path to save tables, splits and images
datadir = '/Users/brissa/Documents/SgrAobservations/TRACKC/CompactC/superuniUV100C/'

# The mask that will be used for the no interactive step of the tclean process, this is the area for the convolution
Mask = '/Users/brissa/Documents/SgrAobservations/TRACKB/CompactB/superuniUV100/smallermask.crtf'

# MS file flagged for the tclean process
MsName =  '/Users/brissa/Documents/SgrAobservations/TRACKC/CompactC/TRACK_C_SgrA_f.ms'

```

```
list_of_scans = [1,3,4,6,7,9,11,12,14,15,17,19,20,22,24,25,
    27,28,30,32,33,34,36,37,39,40,42,43,45,47,48,50,51,53,54,55,56]
for scan in list_of_scans:
        target = 'TRACK_C_SgrA_comp_suniUV'+str(scan)
        TargetField = '0'
        SpecWin = '0,1,2,3'
        TargetSplitFile = datadir+target+'.split'
        TargetImage = datadir+target+'.image'

        # Parameter for tclean process, remember that this script
    has the goal of smooth the cut so it will be used the
    superuniform weighting
        CellSize = '0.122arcsec'
        NiterCal = 200
        NiterTarget = 500
        imsizeTarget= 420

        os.system('rm -rf '+TargetSplitFile)
        split(vis=MsName, outputvis=TargetSplitFile, datacolumn='
    data', field=TargetField, spw=SpecWin, scan=str(scan))

        os.system('rm -rf '+TargetImage+'*')
        tclean(vis=TargetSplitFile, imagename=TargetImage, specmode
    ='mfs', deconvolver='hogbom', imsize=imsizeTarget, cell=[
    CellSize], weighting='superuniform', interactive=False, niter=
    NiterCal, mask=Mask, uvrange='>100')
```

B.1.3 TRACK E

```
# Script to create the images of the compact emission without UV
    dist and using WEIGHTING SUPERUNIFORM
# Corrected in datacolumn, this script uses a mask for the NO
    interactive process of tclean
#####################################################
import os

# Path to save tables, splits and images
datadir = '/Users/brissa/Documents/SgrAobservations/TRACKE/CompactE
    /superuniUV100E/'

# The mask that will be used for the no interactive step of the
    tclean process, this is the area for the convolution
Mask = '/Users/brissa/Documents/SgrAobservations/TRACKB/CompactB/
    superuniUV100/smallermask.crtf'

# MS file flagged for the tclean process
MsName =  '/Users/brissa/Documents/SgrAobservations/TRACKE/CompactE
    /TRACK_E_SgrA_f.ms'

list_of_scans =
    [58,60,61,63,64,65,67,68,69,71,72,73,74,76,77,79,80,82]
for scan in list_of_scans:
        target = 'TRACK_E_SgrA_comp_suniUV'+str(scan)
        TargetField = '0'
```

```
        SpecWin = '0,1,2,3'
        TargetSplitFile = datadir+target+'.split'
        TargetImage = datadir+target+'.image'

        # Parameter for tclean process, remember that this script has the goal of smooth the cut so it will be used the superuniform weighting
        CellSize = '0.122arcsec'
        NiterCal = 200
        NiterTarget = 500
        imsizeTarget= 420

        os.system('rm -rf '+TargetSplitFile)
        split(vis=MsName, outputvis=TargetSplitFile, datacolumn='data', field=TargetField, spw=SpecWin, scan=str(scan))

        os.system('rm -rf '+TargetImage+'*')
        tclean(vis=TargetSplitFile, imagename=TargetImage, specmode='mfs', deconvolver='hogbom', imsize=imsizeTarget, cell=[CellSize], weighting='superuniform', interactive=False, niter=NiterCal, mask=Mask)
```

B.2 Self-calibration Scripts

The process of self-calibration is iterative. In this work four images were created for 3 iterations of self-calibration. This process is very similar to a initial calibration process that consists in using a calibrator as a model to determine corrections factors (complex gains). In the case of self-calibration, an image of the source itself is used as a model.

A flux diagram helps to understand the process. The first flux diagram represents the initial calibration process and the second one represents self-calibration additions to the first process.

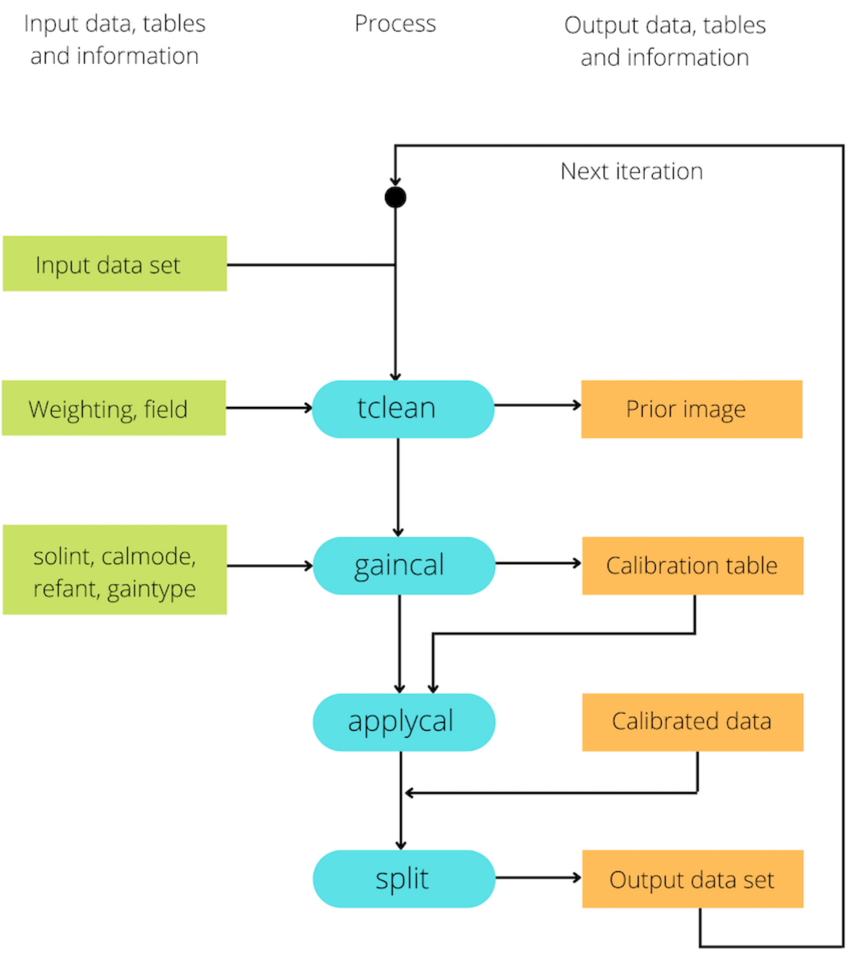

Figure B.1: *initial calibration process, starting with the input data. The calibration process is described as well as and output data and relevant information.*

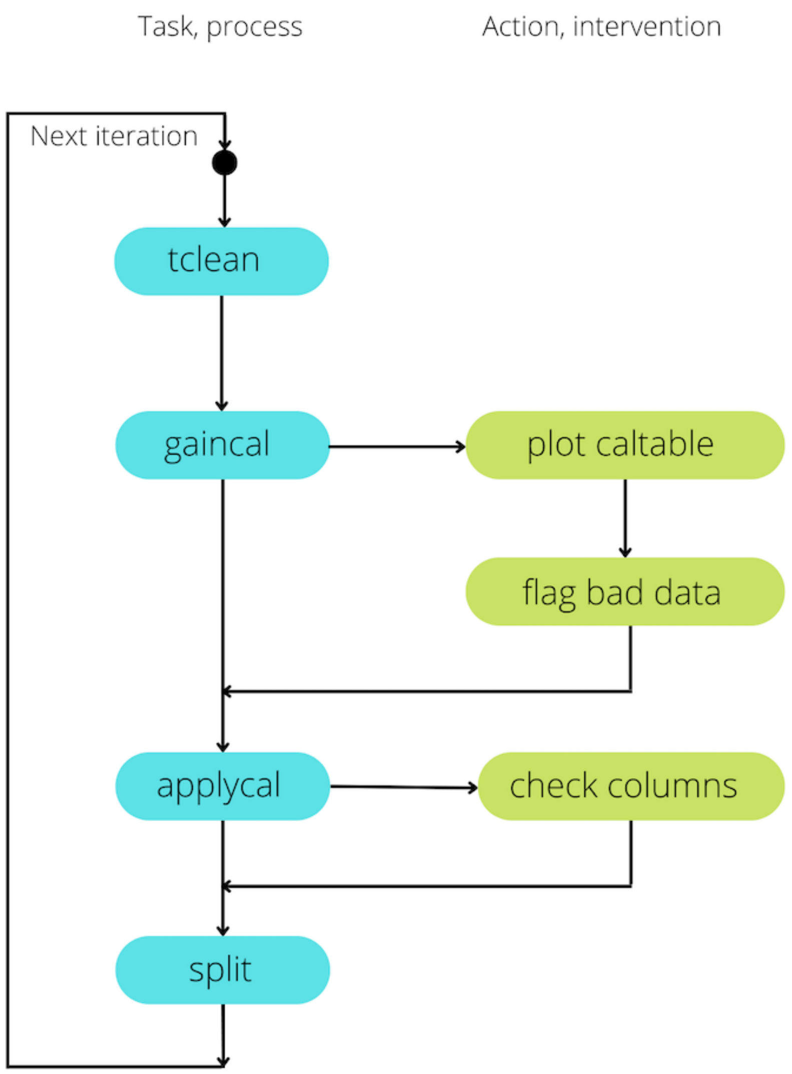

Figure B.2: *This diagram shows additional actions applied to the calibration process to complete the self-calibration process.*

B.2.1 TRACK B self-calibration script

Phase-only

```
# This script was write to do the first self calibration of SgrA
    including the extenden emission for TRACK B
##############################################

listobs("TRACK_B_SgrA.ms")

# FIRST ROUND OF CALIBRATION
tclean(vis='TRACK_B_SgrA.ms', imagename='TRACK_B_ext_s20_first',
    field='0', specmode='mfs', deconvolver='hogbom', imsize
    =[420,420], cell=['0.122arcsec'], weighting='briggs', robust
    =0.5, interactive=True, niter=200, savemodel='modelcolumn')
```

```
tb.open("TRACK_B_SgrA.ms", nomodify=False)
tb.colnames()

os.system("rm -rf phase.cal")
gaincal(vis="TRACK_B_SgrA.ms", caltable="phase.cal", field="0",
    solint="20s", calmode="p", refant="DV23", gaintype="G")

plotms(vis='phase.cal', xaxis='time', yaxis='phase')
plotms(vis='phase.cal', xaxis='time', yaxis='SNR')

applycal(vis="TRACK_B_SgrA.ms",field="0", gaintable=["phase.cal"],
    interp="linear")

tb.open("TRACK_B_SgrA.ms", nomodify=False)
tb.colnames()

os.system("rm -rf TRACK_B_SgrA_selfcal.ms TRACK_B_Sgra_selfcal.ms.
    flagversions")
split(vis="TRACK_B_SgrA.ms", outputvis="TRACK_B_SgrA_selfcal.ms",
    datacolumn="corrected")

# SECOND ROUND OF CALIBRATION
os.system('rm -rf TRACK_B_SgrA_ext_s20_second_image.*')
tclean(vis='TRACK_B_SgrA_selfcal.ms', imagename='
    TRACK_B_SgrA_ext_s20_second_image', field='0', specmode='mfs',
    deconvolver='hogbom', imsize=[420,420], cell=['0.122arcsec'],
    weighting='briggs', robust=0.5, interactive=True, niter=200,
    savemodel='modelcolumn')

os.system("rm -rf phase_second.cal")
gaincal(vis="TRACK_B_SgrA_selfcal.ms", caltable="phase_second.cal",
     field="0", solint="20s", calmode="p", refant="DV23", gaintype="
    G")


applycal(vis="TRACK_B_SgrA_selfcal.ms", field="0", gaintable=["
    phase_second.cal"], interp="linear")

os.system("rm -rf TRACK_B_SgrA_selfcal_2.ms TRACK_B_Sgra_selfcal_2.
    ms.flagversions")
split(vis="TRACK_B_SgrA_selfcal.ms", outputvis="
    TRACK_B_SgrA_selfcal_2.ms", datacolumn="corrected")

# THIRD ROUND OF SELF CALIBRATION
os.system('rm -rf TRACK_B_SgrA_ext_s20_third_image.*')
tclean(vis='TRACK_B_SgrA_selfcal_2.ms', imagename='
    TRACK_B_SgrA_ext_s20_third_image', field='0', specmode='mfs',
    deconvolver='hogbom', imsize=[420,420], cell=['0.122arcsec'],
    weighting='briggs', robust=0.5, interactive=True, niter=200,
    savemodel='modelcolumn')

os.system("rm -rf phase_third.cal")
gaincal(vis="TRACK_B_SgrA_selfcal_2.ms", caltable="phase_third.cal"
    , field="0", solint="20s", calmode="p", refant="DV23", gaintype=
```

```
"G")


applycal(vis="TRACK_B_SgrA_selfcal_2.ms", field="0", gaintable=["phase_third.cal"], interp="linear")

os.system("rm -rf TRACK_B_SgrA_selfcal_3.ms TRACK_B_Sgra_selfcal_3.ms.flagversions")
split(vis="TRACK_B_SgrA_selfcal_2.ms", outputvis="TRACK_B_SgrA_selfcal_3.ms", datacolumn="corrected")

os.system('rm -rf TRACK_B_SgrA_ext_s20_fourth_image.*')
tclean(vis='TRACK_B_SgrA_selfcal_3.ms', imagename='TRACK_B_SgrA_ext_s20_fourth_image', field='0', specmode='mfs', deconvolver='hogbom', imsize=[420,420], cell=['0.122arcsec'], weighting='briggs', robust=0.5, interactive=True, niter=200, savemodel='modelcolumn')
```

Amplitude-phase

```
# Self calibrate the amplitude and phase of the data observations incluiding the extended emission
### Using solint 60 sec and flagging each gain table before the applycal, so this is NOT A SCRIT TO RUN COMPLETELY
############################################

MsFile= "/Users/brissa/Documents/SgrAobservations/TRACKB/msFiles/SelfCalB/apSelfCalB_60s_f_240221/TRACK_B_SgrA_selfcal_3.ms"
listobs(MsFile)

# First iteration
tclean(vis=MsFile, imagename='TRACK_B_amp_ext_s60_1', field='0', specmode='mfs', deconvolver='hogbom', imsize=[420,420], cell=['0.122arcsec'], weighting='briggs', robust=0.5, interactive=True, niter=200, savemodel='modelcolumn')

tb.open(MsFile, nomodify=False)
tb.colnames()

os.system("rm -rf amp.cal")
gaincal(vis = MsFile, caltable = "amp.cal", field="0", solint="60s", calmode="ap", refant="DV23", gaintype="G", solnorm=True)

applycal(vis=MsFile, field='0', gaintable=["amp.cal"], interp="linear")

tb.open(MsFile, nomodify=False)
tb.colnames()

os.system("rm -rf TRACK_B_SgrA_selfcal_amp.ms TRACK_B_Sgra_selfcal_amp.ms.flagversions")
split(vis=MsFile, outputvis="TRACK_B_SgrA_selfcal_amp.ms", datacolumn="corrected")

os.system('rm -rf TRACK_B_amp_ext_s60_2_image.*')
```

```
tclean(vis='TRACK_B_SgrA_selfcal_amp.ms', imagename='TRACK_B_amp_ext_s60_2_image', field='0', specmode='mfs', deconvolver='hogbom', imsize=[420,420], cell=['0.122arcsec'], weighting='briggs', robust=0.5, interactive=True, niter=200, savemodel='modelcolumn')

# Second iteration
os.system("rm -rf amp_second.cal")
gaincal(vis = "TRACK_B_SgrA_selfcal_amp.ms", caltable = "amp_second.cal", field="0", solint="60s", calmode="ap", refant="DV23", gaintype="G", solnorm=True)

applycal(vis="TRACK_B_SgrA_selfcal_amp.ms", field='0', gaintable=["amp_second.cal"], interp="linear")

os.system("rm -rf TRACK_B_SgrA_selfcal_amp_2.ms TRACK_B_Sgra_selfcal_amp_2.ms.flagversions")
split(vis="TRACK_B_SgrA_selfcal_amp.ms", outputvis="TRACK_B_SgrA_selfcal_amp_2.ms", datacolumn="corrected")

os.system('rm -rf TRACK_B_amp_ext_s60_3_image.*')
tclean(vis='TRACK_B_SgrA_selfcal_amp_2.ms', imagename='TRACK_B_amp_ext_s60_3_image', field='0', specmode='mfs', deconvolver='hogbom', imsize=[420,420], cell=['0.122arcsec'], weighting='briggs', robust=0.5, interactive=True, niter=200, savemodel='modelcolumn')

# Third iteration
os.system("rm -rf amp_third.cal")
gaincal(vis = "TRACK_B_SgrA_selfcal_amp_2.ms", caltable = "amp_third.cal", field="0", solint="60s", calmode="ap", refant="DV23", gaintype="G", solnorm=True)

applycal(vis="TRACK_B_SgrA_selfcal_amp_2.ms", field='0', gaintable=["amp_third.cal"], interp="linear")

os.system("rm -rf TRACK_B_SgrA_selfcal_amp_3.ms TRACK_B_Sgra_selfcal_amp_3.ms.flagversions")
split(vis="TRACK_B_SgrA_selfcal_amp_2.ms", outputvis="TRACK_B_SgrA_selfcal_amp_3.ms", datacolumn="corrected")

os.system('rm -rf TRACK_B_amp_ext_s60_4_image.*')
tclean(vis='TRACK_B_SgrA_selfcal_amp_3.ms', imagename='TRACK_B_amp_ext_s60_4_image', field='0', specmode='mfs', deconvolver='hogbom', imsize=[420,420], cell=['0.122arcsec'], weighting='briggs', robust=0.5, interactive=True, niter=200, savemodel='modelcolumn')
```

B.2.2 TRACK C self-calibration script

Phase-only

```
# This script self calibrate the phase of the extended emission in TRACK C of SgrA, using solint 20 sec as I used in past self
```

```
calibrations
##################################################

listobs("TRACK_C_SgrA_f.ms")

# First iteration of calibration
tclean(vis='TRACK_C_SgrA_f.ms', imagename='TRACK_C_ext_s20_first', field='0', specmode='mfs', deconvolver='hogbom', imsize=[420,420], cell=['0.122arcsec'], weighting='briggs', robust=0.5, interactive=True, niter=200, savemodel='modelcolumn')

tb.open("TRACK_C_SgrA_f.ms")
tb.colnames()

os.system("rm -rf phase.cal")
gaincal(vis="TRACK_C_SgrA_f.ms", caltable="phase.cal", field="0", solint="20s", calmode="p", refant="DA59", gaintype="G")


plotms(vis='phase.cal', xaxis='time', yaxis='phase')

plotms(vis='phase.cal', xaxis='time', yaxis='SNR')

applycal(vis="TRACK_C_SgrA_f.ms", field="0",  gaintable=["phase.cal"], interp="linear")

tb.open("TRACK_C_SgrA_f.ms", nomodify=False)
tb.colnames()

os.system("rm -rf TRACK_C_SgrA_pselfcal.ms TRACK_C_SgrA_pselfcal.ms.flagversions")
split(vis="TRACK_C_SgrA_f.ms", outputvis="TRACK_C_SgrA_pselfcal.ms", datacolumn="corrected")


os.system('rm -rf TRACK_C_SgrA_ext_p_s20_second_image.*')
tclean(vis='TRACK_C_SgrA_pselfcal.ms', imagename='TRACK_C_SgrA_ext_p_s20_second_image', field='0', specmode='mfs', deconvolver='hogbom', imsize=[432,432], cell=['0.122arcsec'], weighting='briggs', robust=0.5, interactive=True, niter=200, savemodel='modelcolumn')

# Second Iteration of self calibration
os.system("rm -rf phase_second.cal")
gaincal(vis="TRACK_C_SgrA_pselfcal.ms", caltable="phase_second.cal", field="0", solint="20s", calmode="p", refant="DA59", gaintype="G")

applycal(vis="TRACK_C_SgrA_pselfcal.ms", field="0", gaintable=["phase_second.cal"], interp="linear")

os.system("rm -rf TRACK_C_SgrA_pselfcal_2.ms TRACK_C_SgrA_pselfcal_2.ms.flagversions")
split(vis="TRACK_C_SgrA_pselfcal.ms", outputvis="TRACK_C_SgrA_pselfcal_2.ms", datacolumn="corrected")
```

```

os.system('rm -rf TRACK_C_SgrA_ext_p_s20_third_image.*')
tclean(vis='TRACK_C_SgrA_pselfcal_2.ms', imagename='TRACK_C_SgrA_ext_p_s20_third_image', field='0', specmode='mfs', deconvolver='hogbom', imsize=[432,432], cell=['0.122arcsec'], weighting='briggs', robust=0.5, interactive=True, niter=200, savemodel='modelcolumn')


# Third iteration
os.system("rm -rf phase_third.cal")
gaincal(vis="TRACK_C_SgrA_pselfcal_2.ms", caltable="phase_third.cal", field="0", solint="20s", calmode="p", refant="DA59", gaintype="G")

applycal(vis="TRACK_C_SgrA_pselfcal_2.ms", field="0", gaintable=["phase_third.cal"], interp="linear")
#Using the script with the new table without the scans 50, 51, 53, 54
applycal(vis="TRACK_C_SgrA_pselfcal_2.ms", field="0", gaintable=["phase_third_wolastscans.cal"], interp="linear")


os.system("rm -rf TRACK_C_SgrA_pselfcal_3.ms TRACK_C_SgrA_pselfcal_3.ms.flagversions")
split(vis="TRACK_C_SgrA_pselfcal_2.ms", outputvis="TRACK_C_SgrA_pselfcal_3.ms", datacolumn="corrected")

os.system('rm -rf TRACK_C_SgrA_ext_p_s20_fourth_image.*')
tclean(vis='TRACK_C_SgrA_pselfcal_3.ms', imagename='TRACK_C_SgrA_ext_p_s20_fourth_image', field='0', specmode='mfs', deconvolver='hogbom', imsize=[432,432], cell=['0.122arcsec'], weighting='briggs', robust=0.5, interactive=True, niter=200, savemodel='modelcolumn')
```

Amplitude-phase

```
# Script to selfcalibrate the amplitude of TRACK C extended emission with solint 180 s
###############################################

# First Iteration
MsFile="/Users/brissa/Documents/SgrAobservations/TRACKC/ExtendedC/apselfcal_solint180/TRACK_C_SgrA_pselfcal_3.ms"

tclean(vis=MsFile, imagename='TRACK_C_amp_ext_s180_1', field='0', specmode='mfs', deconvolver='hogbom', imsize=[432,432], cell=['0.122arcsec'], weighting='briggs', robust=0.5, interactive=True, niter=200, savemodel='modelcolumn')

os.system("rm -rf amp_C_ext_s180.cal")
gaincal(vis = MsFile, caltable = "amp_C_ext_s180.cal", field="0", solint="180s", calmode="ap", refant="DA59", gaintype="G", solnorm=True)

```

```
# Open the caltable to flag bad data and then apply next task

applycal(vis=MsFile, field='0', gaintable=["amp_C_ext_s180.cal"],
    interp="linear")

tb.open(MsFile, nomodify=False)
tb.colnames()

os.system("rm -rf TRACK_C_SgrA_selfcal_amp_s180.ms
    TRACK_C_SgrA_selfcal_amp_s180.ms.flagversions")
split(vis=MsFile, outputvis="TRACK_C_SgrA_selfcal_amp_s180.ms",
    datacolumn="corrected")

os.system('rm -rf TRACK_C_amp_ext_s180_2_image.*')
tclean(vis='TRACK_C_SgrA_selfcal_amp_s180.ms', imagename='
    TRACK_B_amp_ext_s180_2_image', field='0', specmode='mfs',
    deconvolver='hogbom', imsize=[432,432], cell=['0.122arcsec'],
    weighting='briggs', robust=0.5, interactive=True, niter=200,
    savemodel='modelcolumn')

#######################################
#### Second iteration
os.system("rm -rf amp_C_ext_s180_second.cal")
gaincal(vis = 'TRACK_C_SgrA_selfcal_amp_s180.ms', caltable = "
    amp_C_ext_s180_second.cal", field="0", solint="180s", calmode="
    ap", refant="DA59", gaintype="G", solnorm=True)

# Open the caltable to flag bad data and then apply next task

applycal(vis='TRACK_C_SgrA_selfcal_amp_s180.ms', field='0',
    gaintable=["amp_C_ext_s180_second.cal"], interp="linear")

tb.open('TRACK_C_SgrA_selfcal_amp_s180.ms', nomodify=False)
tb.colnames()

os.system("rm -rf TRACK_C_SgrA_selfcal_amp_s180_2.ms
    TRACK_C_SgrA_selfcal_amp_s180_2.ms.flagversions")
split(vis='TRACK_C_SgrA_selfcal_amp_s180.ms', outputvis="
    TRACK_C_SgrA_selfcal_amp_s180_2.ms", datacolumn="corrected")

os.system('rm -rf TRACK_C_amp_ext_s180_3_image.*')
tclean(vis='TRACK_C_SgrA_selfcal_amp_s180_2.ms', imagename='
    TRACK_B_amp_ext_s180_3_image', field='0', specmode='mfs',
    deconvolver='hogbom', imsize=[432,432], cell=['0.122arcsec'],
    weighting='briggs', robust=0.5, interactive=True, niter=200,
    savemodel='modelcolumn')

##################
# Third iteration
os.system("rm -rf amp_C_ext_s180_third.cal")
gaincal(vis = 'TRACK_C_SgrA_selfcal_amp_s180_2.ms', caltable = "
    amp_C_ext_s180_third.cal", field="0", solint="180s", calmode="ap
    ", refant="DA59", gaintype="G", solnorm=True)

# Open the caltable to flag bad data and then apply next task
```

```
applycal(vis='TRACK_C_SgrA_selfcal_amp_s180_2.ms', field='0', gaintable=["amp_C_ext_s180_third.cal"], interp="linear")

tb.open('TRACK_C_SgrA_selfcal_amp_s180_2.ms', nomodify=False)
tb.colnames()

os.system("rm -rf TRACK_C_SgrA_selfcal_amp_s180_3.ms TRACK_C_SgrA_selfcal_amp_s180_3.ms.flagversions")
split(vis='TRACK_C_SgrA_selfcal_amp_s180_2.ms', outputvis="TRACK_C_SgrA_selfcal_amp_s180_3.ms", datacolumn="corrected")

os.system('rm -rf TRACK_C_amp_ext_s180_4_image.*')
tclean(vis='TRACK_C_SgrA_selfcal_amp_s180_3.ms', imagename='TRACK_B_amp_ext_s180_4_image', field='0', specmode='mfs', deconvolver='hogbom', imsize=[432,432], cell=['0.122arcsec'], weighting='briggs', robust=0.5, interactive=True, niter=200, savemodel='modelcolumn')
```

B.2.3 TRACK E self-calibration script

Phase-only

```
# This script was write to do the first self calibration of SgrA including the extenden emission without scan 77 and solint 20s
########################################
listobs("TRACK_E_SgrA_f.ms")

# FIRST ROUND OF CALIBRATION
tclean(vis='TRACK_E_SgrA_f.ms', imagename='TRACK_E_extended_first', field='0', specmode='mfs', deconvolver='hogbom', imsize=[420,420], cell=['0.122arcsec'], weighting='briggs', robust=0.5, interactive=True, niter=200, savemodel='modelcolumn')

tb.open("TRACK_E_SgrA_f.ms", nomodify=False)
tb.colnames()

os.system("rm -rf phase.cal")
gaincal(vis="TRACK_E_SgrA_f.ms", caltable="phase.cal", field="0", solint="20s", calmode="p", refant="DV23", gaintype="G")

plotms(vis='phase.cal', xaxis='time', yaxis='phase')

plotms(vis='phase.cal', xaxis='time', yaxis='SNR')

applycal(vis="TRACK_E_SgrA_f.ms",field="0", gaintable=["phase.cal"], interp="linear")

tb.open("TRACK_E_SgrA_f.ms", nomodify=False)
tb.colnames()

os.system("rm -rf TRACK_E_SgrA_selfcal.ms TRACK_E_Sgra_selfcal.ms.flagversions")
```

```
split(vis="TRACK_E_SgrA_f.ms", outputvis="TRACK_E_SgrA_selfcal.ms",
     datacolumn="corrected")

# SECOND ROUND OF CALIBRATION
os.system('rm -rf TRACK_E_SgrA_extended_second_image.*')
tclean(vis='TRACK_E_SgrA_selfcal.ms', imagename='
    TRACK_E_SgrA_extended_second_image', field='0', specmode='mfs',
    deconvolver='hogbom', imsize=[420,420], cell=['0.122arcsec'],
    weighting='briggs', robust=0.5, interactive=True, niter=200,
    savemodel='modelcolumn')

os.system("rm -rf phase_second.cal")
gaincal(vis="TRACK_E_SgrA_selfcal.ms", caltable="phase_second.cal",
     field="0", solint="20s", calmode="p", refant="DV23", gaintype="
    G")

applycal(vis="TRACK_E_SgrA_selfcal.ms", field="0", gaintable=["
    phase_second.cal"], interp="linear")

os.system("rm -rf TRACK_E_SgrA_selfcal_2.ms TRACK_E_Sgra_selfcal_2.
    ms.flagversions")
split(vis="TRACK_E_SgrA_selfcal.ms", outputvis="
    TRACK_E_SgrA_selfcal_2.ms", datacolumn="corrected")

# THIRD ROUND OF SELF CALIBRATION
os.system('rm -rf TRACK_E_SgrA_extended_third_image.*')
tclean(vis='TRACK_E_SgrA_selfcal_2.ms', imagename='
    TRACK_E_SgrA_extended_third_image', field='0', specmode='mfs',
    deconvolver='hogbom', imsize=[420,420], cell=['0.122arcsec'],
    weighting='briggs', robust=0.5, interactive=True, niter=200,
    savemodel='modelcolumn')

os.system("rm -rf phase_third.cal")
gaincal(vis="TRACK_E_SgrA_selfcal_2.ms", caltable="phase_third.cal"
    , field="0", solint="20s", calmode="p", refant="DV23", gaintype=
    "G")

applycal(vis="TRACK_E_SgrA_selfcal_2.ms", field="0", gaintable=["
    phase_third.cal"], interp="linear")

os.system("rm -rf TRACK_E_SgrA_selfcal_3.ms TRACK_E_Sgra_selfcal_3.
    ms.flagversions")
split(vis="TRACK_E_SgrA_selfcal_2.ms", outputvis="
    TRACK_E_SgrA_selfcal_3.ms", datacolumn="corrected")

os.system('rm -rf TRACK_E_SgrA_extended_fourth_image.*')
tclean(vis='TRACK_E_SgrA_selfcal_3.ms', imagename='
    TRACK_E_SgrA_extended_fourth_image', field='0', specmode='mfs',
    deconvolver='hogbom', imsize=[420,420], cell=['0.122arcsec'],
    weighting='briggs', robust=0.5, interactive=True, niter=200,
    savemodel='modelcolumn')
```

Amplitude-phase

```
# # Script to selfcalibrate the amplitude of TRACK E extended emission with solint 180 s
###########################################

# First Iteration
MsFile="/Users/brissa/Documents/SgrAobservations/TRACKE/ExtendedE/apSelfCal_solint180/TRACK_E_SgrA_selfcal_3.ms"

tclean(vis=MsFile, imagename='TRACK_E_amp_ext_s180_1', field='0', specmode='mfs', deconvolver='hogbom', imsize=[432,432], cell=['0.122arcsec'], weighting='briggs', robust=0.5, interactive=True, niter=200, savemodel='modelcolumn')

os.system("rm -rf amp_E_ext_s180.cal")
gaincal(vis = MsFile, caltable = "amp_E_ext_s180.cal", field="0", solint="180s", calmode="ap", refant="DV23", gaintype="G", solnorm=True)

# Open the caltable to flag bad data and then apply next task

applycal(vis=MsFile, field='0', gaintable=["amp_E_ext_s180.cal"], interp="linear")

tb.open(MsFile, nomodify=False)
tb.colnames()

os.system("rm -rf TRACK_E_SgrA_selfcal_amp_s180.ms TRACK_E_SgrA_selfcal_amp_s180.ms.flagversions")
split(vis=MsFile, outputvis="TRACK_E_SgrA_selfcal_amp_s180.ms", datacolumn="corrected")

os.system('rm -rf TRACK_E_amp_ext_s180_2_image.*')

tclean(vis='TRACK_E_SgrA_selfcal_amp_s180.ms', imagename='TRACK_E_amp_ext_s180_2_image', field='0', specmode='mfs', deconvolver='hogbom', imsize=[432,432], cell=['0.122arcsec'], weighting='briggs', robust=0.5, interactive=True, niter=200, savemodel='modelcolumn')


############################################
## Second Iteration

os.system("rm -rf amp_E_ext_s180_second.cal")
gaincal(vis = 'TRACK_E_SgrA_selfcal_amp_s180.ms', caltable = "amp_E_ext_s180_second.cal", field="0", solint="180s", calmode="ap", refant="DV23", gaintype="G", solnorm=True)

# Open the caltable to flag bad data and then apply next task

applycal(vis='TRACK_E_SgrA_selfcal_amp_s180.ms', field='0', gaintable=["amp_E_ext_s180_second.cal"], interp="linear")

tb.open('TRACK_E_SgrA_selfcal_amp_s180.ms', nomodify=False)
tb.colnames()
```

```
os.system("rm -rf TRACK_E_SgrA_selfcal_amp_s180_2.ms
    TRACK_E_SgrA_selfcal_amp_s180_2.ms.flagversions")
split(vis='TRACK_E_SgrA_selfcal_amp_s180.ms', outputvis="
    TRACK_E_SgrA_selfcal_amp_s180_2.ms", datacolumn="corrected")

os.system('rm -rf TRACK_E_amp_ext_s180_3_image.*')
tclean(vis='TRACK_E_SgrA_selfcal_amp_s180_2.ms', imagename='
    TRACK_E_amp_ext_s180_3_image', field='0', specmode='mfs',
    deconvolver='hogbom', imsize=[432,432], cell=['0.122arcsec'],
    weighting='briggs', robust=0.5, interactive=True, niter=200,
    savemodel='modelcolumn')

############################################
## Third Iteration

os.system("rm -rf amp_E_ext_s180_third.cal")
gaincal(vis = 'TRACK_E_SgrA_selfcal_amp_s180_2.ms', caltable = "
    amp_E_ext_s180_third.cal", field="0", solint="180s", calmode="ap
    ", refant="DV23", gaintype="G", solnorm=True)

# Open the caltable to flag bad data and then apply next task

applycal(vis='TRACK_E_SgrA_selfcal_amp_s180_2.ms', field='0',
    gaintable=["amp_E_ext_s180_third.cal"], interp="linear")

tb.open('TRACK_E_SgrA_selfcal_amp_s180_2.ms', nomodify=False)
tb.colnames()

os.system("rm -rf TRACK_E_SgrA_selfcal_amp_s180_3.ms
    TRACK_E_SgrA_selfcal_amp_s180_3.ms.flagversions")
split(vis='TRACK_E_SgrA_selfcal_amp_s180_2.ms', outputvis="
    TRACK_E_SgrA_selfcal_amp_s180_3.ms", datacolumn="corrected")

os.system('rm -rf TRACK_E_amp_ext_s180_4_image.*')
tclean(vis='TRACK_E_SgrA_selfcal_amp_s180_3.ms', imagename='
    TRACK_E_amp_ext_s180_4_image', field='0', specmode='mfs',
    deconvolver='hogbom', imsize=[432,432], cell=['0.122arcsec'],
    weighting='briggs', robust=0.5, interactive=True, niter=200,
    savemodel='modelcolumn')
```

Appendix C

Tables of values for plots

C.1 Fluxes for Light Curves

In order to get the light curves plots, fluxes per scan were measured with their corresponding errors. This was obtained using the same mask for the images and using the task imfit in CASA. The data were saved in the following tables presented per TRACK. All the plots in Section 4.3 are produced from these tables.

Table C.1:

Fluxes per scan for TRACK B					
Scan	Peak Flux (Jy/beam)	Peak error flux (Jy/beam)	Integrated Flux (mJy/beam)	Integrated flux error (mJy/beam)	Renamed Scan
50	2.5367	0.0058	2.583	0.011	1
51	2.5377	0.0058	2.582	0.011	2
53	2.5436	0.0092	2.587	0.017	3
56	2.5471	0.0087	2.585	0.016	4
58	2.5447	0.0053	2.5825	0.0096	5
59	2.5457	0.0052	2.5833	0.0093	6
61	2.5486	0.0055	2.5885	0.0099	7
62	2.5468	0.0066	2.592	0.012	8
64	2.5435	0.0097	2.594	0.018	9
65	2.549	0.011	2.598	0.021	10
67	2.554	0.012	2.599	0.023	11
68	2.564	0.015	2.616	0.028	12
70	2.5496	0.0048	2.6090	0.0096	13
71	2.5464	0.0043	2.6070	0.0086	14
73	2.5439	0.0051	2.590	0.011	15
74	2.5298	0.0048	2.568	0.011	16
76	2.5253	0.0036	2.5652	0.0082	17
77	2.5440	0.0039	2.5937	0.0092	18
79	2.5365	0.0042	2.572	0.012	19
80	2.346	0.011	2.551	0.037	20
81	2.5145	0.0036	2.500	0.012	21

Table C.2:

Fluxes per scan for TRACK C

Scan	Peak Flux (Jy/beam)	Peak error flux (Jy/beam)	Integrated Flux (mJy/beam)	Integrated flux error (mJy/beam)	Renamed Scan
3	1.5528	0.0070	1.989	0.022	22
4	2.2636	0.0021	2.2665	0.0066	23
6	2.2635	0.0027	2.2698	0.0081	24
7	2.2634	0.0031	2.2699	0.0087	25
9	2.2555	0.0031	2.2694	0.0080	26
11	2.2528	0.003	2.2651	0.0085	27
12	2.1802	0.0038	2.2300	0.0094	28
14	2.1802	0.0038	2.2300	0.0094	29
15	2.1671	0.0044	2.238	0.010	30
17	2.2370	0.0043	2.2552	0.0095	31
19	2.2275	0.0036	2.2543	0.0079	32
20	2.2388	0.0037	2.2665	0.0080	33
22	2.2428	0.0041	2.2689	0.0089	34
24	2.2412	0.0036	2.2691	0.0076	35
25	2.2392	0.0036	2.2714	0.0077	36
27	2.2401	0.0035	2.2734	0.0073	37
28	2.2408	0.0034	2.2731	0.0072	38
30	2.2434	0.0033	2.2748	0.0070	39
33	2.2455	0.0032	2.2719	0.0068	40
34	2.2465	0.0033	2.2731	0.0071	41
36	2.2494	0.0040	2.2777	0.0088	42
37	2.2461	0.0044	2.2749	0.0096	43
39	2.2496	0.0046	2.274	0.010	44
42	2.2509	0.0034	2.2767	0.0080	45
43	2.2488	0.0031	2.2738	0.0075	46
45	2.2433	0.0032	2.2733	0.0079	47
47	2.2301	0.0032	2.2661	0.0085	48
48	2.2374	0.0038	2.265	0.010	49
50	2.1558	0.0060	2.244	0.017	50
51	2.092	0.011	2.116	0.033	51
53	2.2161	0.0062	2.231	0.021	52
54	2.1188	0.0084	2.161	0.032	53

Table C.3:

Fluxes per scan for TRACK E					
Scan	Peak Flux (Jy/beam)	Peak error flux (Jy/beam)	Integrated Flux (mJy/beam)	Integrated flux error (mJy/beam)	Renamed Scan
58	2.7009	0.0051	2.6764	0.0092	54
60	2.6991	0.0048	2.6733	0.0087	55
61	2.7010	0.0046	2.6724	0.0083	56
63	2.7009	0.0043	2.6698	0.0078	57
64	2.6900	0.0036	2.6624	0.0065	58
65	2.6911	0.0032	2.6662	0.0059	59
67	2.6855	0.0033	2.6680	0.0060	60
68	2.6611	0.0034	2.6624	0.0063	61
69	2.6839	0.0037	2.6696	0.0068	62
71	2.6846	0.0041	2.6723	0.0078	63
72	2.6762	0.0043	2.6731	0.0082	64
73	2.6889	0.0051	2.670	0.010	65
74	2.5030	0.0071	2.646	0.014	66
76	2.214	0.012	2.545	0.025	67
77	1.241	0.032	2.176	0.085	68

C.2 Phasing efficiency values tables

Using `visstats` in CASA the mean values for the visibilities were computed. This allows to get the real and imaginary part of the amplitude final value to estimate the effect of extended emission on the phasing efficiency per scan and spectral window (spw). In the following tables *Mean Real* and *Mean Imag* correspond to the mean values only for the real and imaginary parts of the complex number in Jy units. Original column is the data before self-calibration.

Scan	spw	Mean Real Self-Cal (Jy)	Mean Imag Self-Cal (Jy)	Mean Real Original (Jy)	Mean Imag Original (Jy)	Total Self-Cal (Jy)	Total Original (Jy)	Efficiency
50	0	1.2966	-0.0079	1.3013	-0.0083	1.2966	1.3013	1.0036
51	0	1.2933	-0.0075	1.2981	-0.0080	1.2933	1.2981	1.0037
53	0	1.2576	-0.0072	1.2625	-0.0078	1.2576	1.2625	1.0039
56	0	1.2325	-0.0055	1.2358	-0.0062	1.2325	1.2358	1.0027
58	0	1.2312	-0.0044	1.2330	-0.0052	1.2312	1.2330	1.0015
59	0	1.2326	-0.0040	1.2344	-0.0049	1.2326	1.2344	1.0015
61	0	1.2166	-0.0029	1.2184	-0.0038	1.2166	1.2184	1.0015
62	0	1.2228	-0.0023	1.2262	-0.0032	1.2228	1.2262	1.0027
64	0	1.2303	-0.0020	1.2308	-0.0030	1.2303	1.2308	1.0005
65	0	1.2294	-0.0007	1.2331	-0.0016	1.2294	1.2331	1.0031
67	0	1.1879	0.0010	1.1885	0.0002	1.1879	1.1885	1.0005
68	0	1.1654	0.0023	1.1667	0.0013	1.1654	1.1667	1.0011

Table C.4: *Values for phasing efficiency amplitude-phase TRACK B. Continue in next page.*

Scan	spw	Mean Real Original (Jy)	Mean Imag Original (Jy)	Mean Real Self-Cal (Jy)	Mean Imag Self-Cal (Jy)	Total Original (Jy)	Total Self-Cal (Jy)	Efficiency
70	0	1.1685	0.0036	1.1651	0.0027	1.1685	1.1651	0.9971
71	0	1.1815	0.0043	1.1833	0.0034	1.1815	1.1833	1.0015
73	0	1.2032	0.0048	1.2028	0.0041	1.2033	1.2028	0.9996
74	0	1.1887	0.0048	1.1895	0.0047	1.1887	1.1895	1.0007
76	0	1.1849	0.0066	1.1803	0.0040	1.1849	1.1803	0.9961
77	0	1.1688	0.0052	1.1697	0.0040	1.1688	1.1697	1.0008
79	0	1.1691	0.0046	1.1667	0.0065	1.1691	1.1668	0.9980
80	0	1.1615	0.0056	1.1506	0.0050	1.1615	1.1506	0.9906
81	0	1.1548	0.0012	1.1540	0.0019	1.1548	1.1540	0.9993
50	1	1.2942	-0.0076	1.2979	-0.0079	1.2942	1.2979	1.0028
51	1	1.2905	-0.0071	1.2942	-0.0076	1.2905	1.2942	1.0029
53	1	1.2545	-0.0065	1.2583	-0.0070	1.2545	1.2583	1.0030

Table C.4: *Values for phasing efficiency amplitude-phase TRACK B. Continue in next page.*

Scan	spw	Mean Real Original (Jy)	Mean Imag Original (Jy)	Mean Real Self-Cal (Jy)	Mean Imag Self-Cal (Jy)	Total Original (Jy)	Total Self-Cal (Jy)	Efficiency
56	1	1.2312	-0.0056	1.2341	-0.0063	1.2312	1.2341	1.0024
58	1	1.2296	-0.0040	1.2318	-0.0048	1.2296	1.2318	1.0018
59	1	1.2306	-0.0037	1.2328	-0.0045	1.2306	1.2328	1.0018
61	1	1.2151	-0.0025	1.2172	-0.0034	1.2151	1.2172	1.0017
62	1	1.2213	-0.0020	1.2251	-0.0029	1.2213	1.2251	1.0031
64	1	1.2286	-0.0016	1.2291	-0.0025	1.2286	1.2291	1.0005
65	1	1.2278	-0.0006	1.2321	-0.0015	1.2278	1.2321	1.0035
67	1	1.1860	0.0012	1.1873	0.0005	1.1860	1.1873	1.0011
68	1	1.1637	0.0016	1.1650	0.0015	1.1637	1.1650	1.0011
70	1	1.1649	0.0035	1.1640	0.0031	1.1649	1.1640	0.9992
71	1	1.1797	0.0044	1.1825	0.0036	1.1797	1.1825	1.0024
73	1	1.2019	0.0061	1.2026	0.0046	1.2019	1.2026	1.0006

Table C.4: *Values for phasing efficiency amplitude-phase TRACK B. Continue in next page.*

Scan	spw	Mean Real Original (Jy)	Mean Imag Original (Jy)	Mean Real Self-Cal (Jy)	Mean Imag Self-Cal (Jy)	Total Original (Jy)	Total Self-Cal (Jy)	Efficiency
74	1	1.1861	0.0051	1.1893	0.0052	1.1861	1.1893	1.0027
76	1	1.1831	0.0064	1.1793	0.0042	1.1831	1.1793	0.9968
77	1	1.1664	0.0054	1.1683	0.0044	1.1664	1.1683	1.0016
79	1	1.1669	0.0046	1.1658	0.0065	1.1669	1.1659	0.9991
80	1	1.1561	-0.0001	1.1473	0.0060	1.1561	1.1473	0.9924
81	1	1.1524	0.0020	1.1522	0.0028	1.1524	1.1522	0.9998
50	2	1.2271	-0.0060	1.2289	-0.0065	1.2271	1.2289	1.0014
51	2	1.2234	-0.0057	1.2251	-0.0062	1.2234	1.2251	1.0014
53	2	1.1897	-0.0055	1.1916	-0.0061	1.1898	1.1916	1.0015
56	2	1.1743	-0.0048	1.1763	-0.0055	1.1743	1.1764	1.0017
58	2	1.1709	-0.0038	1.1730	-0.0046	1.1709	1.1730	1.0019
59	2	1.1719	-0.0035	1.1741	-0.0044	1.1719	1.1741	1.0019

Table C.4: *Values for phasing efficiency amplitude-phase TRACK B. Continue in next page.*

Scan	spw	Mean Real Original (Jy)	Mean Imag Original (Jy)	Mean Real Self-Cal (Jy)	Mean Imag Self-Cal (Jy)	Total Original (Jy)	Total Self-Cal (Jy)	Efficiency
61	2	1.1564	-0.0028	1.1586	-0.0037	1.1564	1.1586	1.0019
62	2	1.1628	-0.0023	1.1667	-0.0033	1.1628	1.1667	1.0034
64	2	1.1641	-0.0016	1.1665	-0.0024	1.1641	1.1665	1.0021
65	2	1.1666	-0.0009	1.1705	-0.0018	1.1666	1.1706	1.0034
67	2	1.1231	0.0009	1.1251	0.0001	1.1231	1.1251	1.0018
68	2	1.1031	0.0014	1.1025	0.0017	1.1031	1.1025	0.9995
70	2	1.1042	0.0003	1.1029	0.0027	1.1042	1.1029	0.9989
71	2	1.1238	0.0037	1.1257	0.0029	1.1238	1.1257	1.0017
73	2	1.1506	0.0057	1.1502	0.0039	1.1506	1.1502	0.9996
74	2	1.1371	0.0049	1.1381	0.0035	1.1371	1.1381	1.0009
76	2	1.1207	0.0046	1.1216	0.0031	1.1207	1.1216	1.0008
77	2	1.1091	0.0035	1.1114	0.0021	1.1091	1.1114	1.0021

Table C.4: *Values for phasing efficiency amplitude-phase TRACK B. Continue in next page.*

Scan	spw	Mean Real Original (Jy)	Mean Imag Original (Jy)	Mean Real Self-Cal (Jy)	Mean Imag Self-Cal (Jy)	Total Original (Jy)	Total Self-Cal (Jy)	Efficiency
79	2	1.1107	0.0012	1.1105	0.0026	1.1107	1.1105	0.9998
80	2	1.1068	0.0061	1.0896	0.0016	1.1068	1.0896	0.9844
81	2	1.0966	0.0023	1.0953	0.0025	1.0966	1.0953	0.9988
50	3	1.2670	-0.0061	1.2711	-0.0065	1.2670	1.2712	1.0033
51	3	1.2634	-0.0059	1.2677	-0.0064	1.2634	1.2677	1.0034
53	3	1.2300	-0.0058	1.2344	-0.0064	1.2300	1.2344	1.0036
56	3	1.2163	-0.0054	1.2194	-0.0061	1.2163	1.2194	1.0026
58	3	1.2106	-0.0040	1.2124	-0.0048	1.2106	1.2124	1.0015
59	3	1.2116	-0.0037	1.2135	-0.0046	1.2116	1.2135	1.0015
61	3	1.1948	-0.0028	1.1966	-0.0038	1.1948	1.1966	1.0015
62	3	1.2013	-0.0023	1.2047	-0.0033	1.2013	1.2047	1.0029
64	3	1.2024	-0.0016	1.2042	-0.0025	1.2024	1.2042	1.0016

Table C.4: *Values for phasing efficiency amplitude-phase TRACK B. Continue in next page.*

Scan	spw	Mean Real Original (Jy)	Mean Imag Original (Jy)	Mean Real Self-Cal (Jy)	Mean Imag Self-Cal (Jy)	Total Original (Jy)	Total Self-Cal (Jy)	Efficiency
65	3	1.2049	-0.0012	1.2085	-0.0021	1.2049	1.2085	1.0029
67	3	1.1594	0.0006	1.1603	-0.0003	1.1594	1.1603	1.0007
68	3	1.1384	0.0015	1.1358	0.0014	1.1384	1.1358	0.9977
70	3	1.1412	0.0022	1.1378	0.0031	1.1412	1.1378	0.9970
71	3	1.1614	0.0041	1.1625	0.0032	1.1614	1.1625	1.0009
73	3	1.1909	0.0062	1.1903	0.0044	1.1909	1.1903	0.9995
74	3	1.1769	0.0055	1.1771	0.0042	1.1769	1.1771	1.0002
76	3	1.1597	0.0060	1.1602	0.0046	1.1598	1.1602	1.0004
77	3	1.1475	0.0051	1.1492	0.0038	1.1475	1.1492	1.0015
79	3	1.1493	0.0030	1.1480	0.0045	1.1493	1.1480	0.9988
80	3	1.1431	0.0038	1.1298	0.0043	1.1431	1.1298	0.9884
81	3	1.1368	0.0029	1.1354	0.0031	1.1368	1.1354	0.9988

Table C.4: Values for phasing efficiency amplitude-phase TRACK B.

Scan	spw	Mean Real Original (Jy)	Mean Imag Original (Jy)	Mean Real Self-Cal (Jy)	Mean Imag Self-Cal (Jy)	Total Original (Jy)	Total Self-Cal (Jy)	Efficiency
6	0	1.0738	-0.0069	1.0737	-0.0071	1.0739	1.0737	1.0002
7	0	1.0719	-0.0077	1.0719	-0.0080	1.0719	1.0719	1.0000
11	0	1.0733	-0.0111	1.0720	-0.0094	1.0733	1.0721	1.0012
12	0	1.0743	-0.0129	1.0667	-0.0037	1.0744	1.0668	1.0072
19	0	1.0630	-0.0112	1.0629	-0.0113	1.0631	1.0629	1.0001
20	0	1.0739	-0.0113	1.0739	-0.0114	1.0740	1.0740	1.0000
22	0	1.0856	-0.0117	1.0856	-0.0119	1.0857	1.0857	1.0000
24	0	1.0969	-0.0106	1.0968	-0.0108	1.0969	1.0969	1.0000
25	0	1.0948	-0.0105	1.0947	-0.0106	1.0948	1.0948	1.0001
27	0	1.0736	-0.0097	1.0735	-0.0098	1.0736	1.0735	1.0001
28	0	1.0660	-0.0093	1.0660	-0.0095	1.0661	1.0660	1.0001
30	0	1.0728	-0.0086	1.0727	-0.0087	1.0728	1.0727	1.0001

Table C.5: *Values for phasing efficiency amplitude-phase TRACK C. Continue in next page.*

Scan	spw	Mean Real Original (Jy)	Mean Imag Original (Jy)	Mean Real Self-Cal (Jy)	Mean Imag Self-Cal (Jy)	Total Original (Jy)	Total Self-Cal (Jy)	Efficiency
33	0	1.0670	-0.0058	1.0669	-0.0060	1.0670	1.0669	1.0001
34	0	1.0558	-0.0055	1.0556	-0.0056	1.0558	1.0556	1.0002
36	0	1.0662	-0.0046	1.0662	-0.0047	1.0662	1.0662	1.0000
37	0	1.0594	-0.0041	1.0593	-0.0042	1.0594	1.0593	1.0000
39	0	1.0367	-0.0023	1.0366	-0.0025	1.0367	1.0367	1.0000
42	0	1.1063	0.0001	1.1062	-0.0000	1.1063	1.1062	1.0000
43	0	1.1262	0.0010	1.1262	0.0009	1.1262	1.1262	1.0000
45	0	1.1134	0.0017	1.1139	0.0014	1.1134	1.1139	0.9996
48	0	1.0994	0.0011	1.0998	0.0011	1.0994	1.0998	0.9997
6	1	1.0664	-0.0070	1.0662	-0.0073	1.0664	1.0662	1.0002
7	1	1.0643	-0.0076	1.0633	-0.0077	1.0643	1.0634	1.0009
19	1	1.0555	-0.0112	1.0551	-0.0146	1.0556	1.0552	1.0004

Table C.5: *Values for phasing efficiency amplitude-phase TRACK C. Continue in next page.*

Scan	spw	Mean Real Original (Jy)	Mean Imag Original (Jy)	Mean Real Self-Cal (Jy)	Mean Imag Self-Cal (Jy)	Total Original (Jy)	Total Self-Cal (Jy)	Efficiency
20	1	1.0681	-0.0110	1.0681	-0.0112	1.0681	1.0682	1.0000
22	1	1.0793	-0.0114	1.0793	-0.0115	1.0794	1.0794	1.0000
24	1	1.0914	-0.0104	1.0914	-0.0105	1.0915	1.0915	1.0000
25	1	1.0890	-0.0101	1.0890	-0.0103	1.0891	1.0891	1.0000
27	1	1.0665	-0.0092	1.0664	-0.0093	1.0665	1.0665	1.0000
28	1	1.0584	-0.0091	1.0584	-0.0092	1.0584	1.0584	1.0000
30	1	1.0658	-0.0082	1.0658	-0.0084	1.0658	1.0658	1.0000
33	1	1.0603	-0.0058	1.0602	-0.0059	1.0603	1.0603	1.0001
34	1	1.0495	-0.0053	1.0493	-0.0054	1.0495	1.0493	1.0002
36	1	1.0595	-0.0045	1.0607	-0.0049	1.0595	1.0608	0.9988
39	1	1.0311	-0.0022	1.0330	-0.0024	1.0311	1.0330	0.9981
42	1	1.1022	0.0001	1.1022	0.0000	1.1022	1.1022	1.0000

Table C.5: *Values for phasing efficiency amplitude-phase TRACK C. Continue in next page.*

Scan	spw	Mean Real Original (Jy)	Mean Imag Original (Jy)	Mean Real Self-Cal (Jy)	Mean Imag Self-Cal (Jy)	Total Original (Jy)	Total Self-Cal (Jy)	Efficiency
43	1	1.1230	0.0010	1.1231	0.0009	1.1230	1.1231	1.0000
45	1	1.1086	0.0017	1.1089	0.0017	1.1086	1.1089	0.9997
48	1	1.0928	0.0017	1.0932	0.0022	1.0928	1.0932	0.9996
6	2	1.0108	-0.0060	1.0107	-0.0063	1.0109	1.0107	1.0002
7	2	1.0063	-0.0065	1.0064	-0.0067	1.0063	1.0064	0.9999
11	2	1.0162	-0.0083	1.0161	-0.0084	1.0163	1.0161	1.0002
12	2	1.0143	-0.0093	1.0143	-0.0094	1.0143	1.0144	0.9999
14	2	1.0372	-0.0091	1.0374	-0.0106	1.0372	1.0375	0.9997
15	2	1.0367	-0.0097	1.0404	-0.0189	1.0368	1.0405	0.9964
19	2	0.9956	-0.0079	0.9957	-0.0105	0.9956	0.9958	0.9998
20	2	1.0115	-0.0086	1.0116	-0.0086	1.0116	1.0116	0.9999
22	2	1.0200	-0.0092	1.0201	-0.0093	1.0201	1.0202	0.9999

Table C.5: *Values for phasing efficiency amplitude-phase TRACK C. Continue in next page.*

Scan	spw	Mean Real Original (Jy)	Mean Imag Original (Jy)	Mean Real Self-Cal (Jy)	Mean Imag Self-Cal (Jy)	Total Original (Jy)	Total Self-Cal (Jy)	Efficiency
24	2	1.0378	-0.0086	1.0378	-0.0087	1.0379	1.0379	1.0000
25	2	1.0357	-0.0085	1.0357	-0.0087	1.0357	1.0357	1.0000
27	2	1.0075	-0.0080	1.0075	-0.0081	1.0075	1.0075	1.0000
28	2	0.9965	-0.0078	0.9965	-0.0080	0.9965	0.9965	1.0000
30	2	1.0062	-0.0073	1.0062	-0.0074	1.0062	1.0062	1.0000
33	2	1.0022	-0.0054	1.0021	-0.0055	1.0022	1.0021	1.0001
34	2	0.9939	-0.0050	0.9937	-0.0051	0.9939	0.9937	1.0002
36	2	1.0071	-0.0044	1.0071	-0.0045	1.0071	1.0071	1.0000
37	2	1.0049	-0.0039	1.0049	-0.0041	1.0049	1.0049	1.0000
39	2	0.9790	-0.0027	0.9791	-0.0028	0.9790	0.9791	1.0000
42	2	1.0619	-0.0004	1.0702	-0.0200	1.0619	1.0704	0.9921
43	2	1.0809	0.0000	1.0791	-0.0001	1.0809	1.0791	1.0017

Table C.5: *Values for phasing efficiency amplitude-phase TRACK C. Continue in next page.*

Scan	spw	Mean Real Original (Jy)	Mean Imag Original (Jy)	Mean Real Self-Cal (Jy)	Mean Imag Self-Cal (Jy)	Total Original (Jy)	Total Self-Cal (Jy)	Efficiency
45	2	1.0618	0.0001	1.0606	0.0012	1.0618	1.0606	1.0011
47	2	1.0348	0.0009	1.0350	0.0007	1.0348	1.0350	0.9998
6	3	1.0503	-0.0070	1.0502	-0.0072	1.0504	1.0502	1.0002
7	3	1.0451	-0.0073	1.0443	-0.0082	1.0451	1.0443	1.0007
11	3	1.0544	-0.0090	1.0563	-0.0142	1.0544	1.0563	0.9982
12	3	1.0553	-0.0098	1.0562	-0.0135	1.0554	1.0563	0.9991
14	3	1.0742	-0.0093	1.0742	-0.0097	1.0742	1.0743	1.0000
15	3	1.0742	-0.0091	1.0740	-0.0094	1.0743	1.0740	1.0002
19	3	1.0289	-0.0083	1.0288	-0.0086	1.0290	1.0289	1.0001
20	3	1.0462	-0.0090	1.0463	-0.0090	1.0462	1.0463	0.9999
22	3	1.0545	-0.0097	1.0546	-0.0097	1.0545	1.0546	0.9999
24	3	1.0740	-0.0090	1.0740	-0.0091	1.0740	1.0740	1.0000

Table C.5: *Values for phasing efficiency amplitude-phase TRACK C. Continue in next page.*

Scan	spw	Mean Real Original (Jy)	Mean Imag Original (Jy)	Mean Real Self-Cal (Jy)	Mean Imag Self-Cal (Jy)	Total Original (Jy)	Total Self-Cal (Jy)	Efficiency
25	3	1.0718	-0.0089	1.0719	-0.0091	1.0719	1.0719	1.0000
27	3	1.0426	-0.0084	1.0426	-0.0086	1.0426	1.0427	1.0000
28	3	1.0308	-0.0083	1.0309	-0.0084	1.0309	1.0309	1.0000
30	3	1.0407	-0.0077	1.0407	-0.0078	1.0407	1.0407	1.0000
33	3	1.0363	-0.0057	1.0362	-0.0058	1.0363	1.0362	1.0001
34	3	1.0279	-0.0053	1.0278	-0.0054	1.0280	1.0278	1.0002
36	3	1.0423	-0.0045	1.0423	-0.0046	1.0423	1.0423	1.0000
37	3	1.0405	-0.0040	1.0406	-0.0042	1.0405	1.0406	0.9999
39	3	1.0134	-0.0026	1.0135	-0.0027	1.0134	1.0135	0.9999
42	3	1.0857	-0.0010	1.0847	-0.0014	1.0857	1.0847	1.0009
45	3	1.1017	0.0014	1.0997	0.0003	1.1017	1.0997	1.0019
47	3	1.0729	0.0011	1.0728	0.0010	1.0729	1.0728	1.0000

Table C.5: Values for phasing efficiency amplitude-phase TRACK C.

Scan	spw	Mean Real Original (Jy)	Mean Imag Original (Jy)	Mean Real Self-Cal (Jy)	Mean Imag Self-Cal (Jy)	Total Original (Jy)	Total Self-Cal (Jy)	Efficiency
58	0	1.28478	-0.01447	1.28063	-0.01481	1.2849	1.2807	1.0032
60	0	1.28527	-0.01410	1.28236	-0.01444	1.2854	1.2824	1.0023
61	0	1.26806	-0.01339	1.26607	-0.01369	1.2681	1.2661	1.0016
63	0	1.24009	-0.01256	1.23897	-0.01279	1.2402	1.2390	1.0009
64	0	1.20052	-0.00996	1.20198	-0.01016	1.2006	1.2020	0.9988
65	0	1.25847	-0.00901	1.25975	-0.00917	1.2586	1.2598	0.9990
67	0	1.25847	-0.00708	1.27951	-0.00717	1.2586	1.2795	0.9836
68	0	1.25453	-0.00620	1.25632	-0.00627	1.2546	1.2563	0.9986
69	0	1.25547	-0.00524	1.25711	-0.00530	1.2556	1.2571	0.9988
71	0	1.24934	-0.00382	1.25064	-0.00390	1.2494	1.2506	0.9990
72	0	1.25176	-0.00269	1.24926	-0.00244	1.2518	1.2493	0.0021
73	0	1.27915	-0.00352	1.27930	-0.00382	1.2792	1.2793	0.9999
74	0	1.28006	-0.00407	1.28052	-0.00398	1.2801	1.2805	0.9997
58	1	1.27751	-0.01455	1.27459	-0.01491	1.2776	1.2747	1.0023
60	1	1.28113	-0.01421	1.27897	-0.01458	1.2812	1.2791	1.0017
61	1	1.26447	-0.01340	1.26296	-0.01372	1.2645	1.26303	1.0012
63	1	1.23692	-0.01220	1.23603	-0.01244	1.2370	1.2361	1.0007
64	1	1.19698	-0.01022	1.19804	-0.01042	1.1971	1.1981	0.9992
65	1	1.25508	-0.00883	1.25621	-0.00899	1.2552	1.2562	0.9991
67	1	1.25508	-0.00694	1.27698	-0.00705	1.2552	1.2770	0.9829
68	1	1.25171	-0.00560	1.25331	-0.00571	1.2518	1.2533	0.9988
69	1	1.25267	-0.00479	1.25405	-0.00485	1.2528	1.2541	0.9990
71	1	1.24583	-0.00318	1.24683	-0.00326	1.2459	1.2468	0.9993
72	1	1.24933	-0.00251	1.24622	-0.00281	1.2494	1.2462	1.0026

Table C.6: *Values for phasing efficiency amplitude-phase TRACK E. Continue in next page.*

Scan	spw	Mean Real Original (Jy)	Mean Imag Original (Jy)	Mean Real Self-Cal (Jy)	Mean Imag Self-Cal (Jy)	Total Original (Jy)	Total Self-Cal (Jy)	Efficiency
73	1	1.27637	-0.00307	1.27620	-0.00325	1.2765	1.2762	1.0002
74	1	1.27749	-0.00388	1.27751	-0.00383	1.2776	1.2775	1.0000
58	2	1.20529	-0.01273	1.20454	-0.01302	1.2054	1.2046	1.0006
60	2	1.21364	-0.01222	1.21291	-0.01253	1.2137	1.2130	1.0006
61	2	1.19695	-0.01133	1.19628	-0.01162	1.1970	1.1963	1.0006
63	2	1.17160	-0.01120	1.17089	-0.01144	1.1717	1.1709	1.0006
64	2	1.12783	-0.00986	1.12789	-0.01002	1.1279	1.1279	1.0000
65	2	1.18512	-0.00847	1.18558	-0.00862	1.1852	1.1856	0.9997
67	2	1.18512	-0.00675	1.21092	-0.00689	1.1852	1.2109	0.9788
68	2	1.18520	-0.00560	1.18587	-0.00571	1.1853	1.1859	0.9995
69	2	1.18491	-0.00467	1.18528	-0.00475	1.1850	1.1853	0.9998
71	2	1.17457	-0.00356	1.17454	-0.00366	1.1747	1.1745	1.0001
72	2	1.18442	-0.00276	1.17818	-0.00322	1.1845	1.1782	1.0054
73	2	1.20874	-0.00298	1.20984	-0.00321	1.2088	1.2098	0.9992
74	2	1.21460	-0.00341	1.21477	-0.00323	1.2147	1.2148	0.9999
58	3	1.25938	-0.01386	1.25680	-0.01430	1.2595	1.2569	1.0021
60	3	1.26651	-0.01339	1.26456	-0.01384	1.2666	1.2646	1.0015
61	3	1.24748	-0.01255	1.24606	-0.01296	1.2476	1.2461	1.0012
63	3	1.21981	-0.01219	1.21885	-0.01256	1.2199	1.2189	1.0008
64	3	1.17143	-0.01070	1.17256	-0.01096	1.1715	1.1726	0.9991
65	3	1.23173	-0.00961	1.23293	-0.00984	1.2318	1.2330	0.9991
67	3	1.23173	-0.00782	1.26019	-0.00801	1.2318	1.2602	0.9775
68	3	1.23241	-0.00650	1.23373	-0.00665	1.2325	1.2337	0.9990
69	3	1.23175	-0.00591	1.23284	-0.00603	1.2318	1.2329	0.9992

Table C.6: *Values for phasing efficiency amplitude-phase TRACK E. Continue in next page.*

Scan	spw	Mean Real Original (Jy)	Mean Imag Original (Jy)	Mean Real Self-Cal (Jy)	Mean Imag Self-Cal (Jy)	Total Original (Jy)	Total Self-Cal (Jy)	Efficiency
71	3	1.22031	-0.00499	1.22113	-0.00511	1.2204	1.2211	0.9994
72	3	1.23227	-0.00358	1.22587	-0.00383	1.2324	1.2259	1.0053
73	3	1.25844	-0.00361	1.26027	-0.00381	1.2585	1.2603	0.9986
74	3	1.26604	-0.00422	1.26626	-0.00392	1.2661	1.2662	0.9999

Table C.6: Values for phasing efficiency amplitude-phase TRACK E.

Bibliography

Abbott, R., Abbott, T. D., Abraham, S., et al. 2020, , 125, 101102, doi: 10.1103/PhysRevLett.125.101102

Balick, B., & Brown, R. L. 1974, , 194, 265, doi: 10.1086/153242

Becklin, E. E., & Neugebauer, G. 1975, ApJ, 200, L71, doi: 10.1086/181899

Bolton, C. T. 1972, Nature Physical Science, 240, 124, doi: 10.1038/physci240124a0

Brown, R. L. 1982, in American Institute of Physics Conference Series, Vol. 83, The Galactic Center, ed. G. R. Riegler & R. D. Blandford, 204–207, doi: 10.1063/1.33478

Carroll, B., & Ostlie, D. 2014, An Introduction to Modern Astrophysics, Pearson custom library (Pearson). https://books.google.com.mx/books?id=RLwangEACAAJ

Doeleman, S. S., Weintroub, J., Rogers, A. E. E., et al. 2008, Nature, 455, 78, doi: 10.1038/nature07245

Eckart, A., SchÂdel, R., & Straubmeier, C. 2005, The Black Hole at the Center of the Milky Way (Imperial College Press). https://books.google.com.mx/books?id=-mFXKO6wd1gC

Eckart, A., Schödel, R., Meyer, L., et al. 2006, The Messenger, 125, 2

Event Horizon Telescope Collaboration, Akiyama, K., Alberdi, A., et al. 2019a, ApJ, 875, L1, doi: 10.3847/2041-8213/ab0ec7

—. 2019b, ApJ, 875, L2, doi: 10.3847/2041-8213/ab0c96

—. 2019c, ApJ, 875, L3, doi: 10.3847/2041-8213/ab0c57

—. 2019d, ApJ, 875, L4, doi: 10.3847/2041-8213/ab0e85

—. 2019e, ApJ, 875, L5, doi: 10.3847/2041-8213/ab0f43

—. 2019f, ApJ, 875, L6, doi: 10.3847/2041-8213/ab1141

Event Horizon Telescope Collaboration, Akiyama, K., Algaba, J. C., et al. 2021a, ApJ, 910, L12, doi: 10.3847/2041-8213/abe71d

—. 2021b, ApJ, 910, L13, doi: 10.3847/2041-8213/abe4de

Event Horizon Telescope Collaboration, Akiyama, K., Alberdi, A., et al. 2022a, ApJ, 930, L12, doi: 10.3847/2041-8213/ac6674

—. 2022b, ApJ, 930, L13, doi: 10.3847/2041-8213/ac6675

—. 2022c, ApJ, 930, L14, doi: 10.3847/2041-8213/ac6429

—. 2022d, ApJ, 930, L15, doi: 10.3847/2041-8213/ac6736

—. 2022e, ApJ, 930, L16, doi: 10.3847/2041-8213/ac6672

—. 2022f, ApJ, 930, L17, doi: 10.3847/2041-8213/ac6756

Fish, V. L., Doeleman, S. S., Beaudoin, C., et al. 2011a, The Astrophysical Journal Letters, 727, L36

—. 2011b, The Astrophysical Journal, 727, L36, doi: 10.1088/2041-8205/727/2/l36

Genzel, R. 2000, The Nuclear Star Cluster of the Milky Way: Star Formation, Dynamics and Central Black Hole. https://arxiv.org/abs/astro-ph/0008119

Ghez, A. M., Klein, B. L., Morris, M., & Becklin, E. E. 1998, , 509, 678, doi: 10.1086/306528

Ghez, A. M., Morris, M., Becklin, E. E., Tanner, A., & Kremenek, T. 2000, , 407, 349, doi: 10.1038/35030032

Goddi, C., Marti-Vidal, I., Messias, H., et al. 2019a, Publications of the Astronomical Society of the Pacific, 131, 075003

Goddi, C., Martí -Vidal, I., Messias, H., et al. 2019b, Publications of the Astronomical Society of the Pacific, 131, 075003, doi: 10.1088/1538-3873/ab136a

GRAVITY Collaboration, Abuter, R., Amorim, A., et al. 2018, A&A, 618, L10, doi: 10.1051/0004-6361/201834294

Ho, L. C. 2008, ARA&A, 46, 475, doi: 10.1146/annurev.astro.45.051806.110546

Johnson, M. D., Fish, V. L., Doeleman, S. S., et al. 2015, Science, 350, 1242, doi: 10.1126/science.aac7087

Killeen, N. E. B., & Lo, K. Y. 1989, in The Center of the Galaxy, ed. M. Morris (Dordrecht: Springer Netherlands), 453–455

Lacy, J. H., Townes, C. H., Geballe, T. R., & Hollenbach, D. J. 1980, , 241, 132, doi: 10.1086/158324

Lo, K. Y., Schilizzi, R. T., Cohen, M. H., & Ross, H. N. 1975, ApJ, 202, L63, doi: 10.1086/181982

Marrone, D. P., Baganoff, F. K., Morris, M. R., et al. 2008, , 682, 373, doi: 10.1086/588806

Matthews, L., Crew, G., Doeleman, S., et al. 2017a, Publications of the Astronomical Society of the Pacific, 130, 015002

Matthews, L. D., Crew, G. B., Doeleman, S. S., et al. 2017b, Publications of the Astronomical Society of the Pacific, 130, 015002, doi: 10.1088/1538-3873/aa9c3d

Miller-Jones, J. C. A., Bahramian, A., Orosz, J. A., et al. 2021, Science, 371, 1046, doi: 10.1126/science.abb3363

Oppenheimer, J. R., & Snyder, H. 1939, Phys. Rev., 56, 455, doi: 10.1103/PhysRev.56.455

Orosz, J. A., McClintock, J. E., Aufdenberg, J. P., et al. 2011, , 742, 84, doi: 10.1088/0004-637X/742/2/84

Reid, M. J., & Brunthaler, A. 2020, , 892, 39, doi: 10.3847/1538-4357/ab76cd

Reid, M. J., Menten, K. M., Brunthaler, A., et al. 2014, , 783, 130, doi: 10.1088/0004-637X/783/2/130

Schneider, P. 2016, Extragalactic Astronomy and Cosmology: An Introduction (Springer Berlin Heidelberg). https://books.google.com.mx/books?id=ckjvvQAACAAJ

Taylor, J. 2005, Classical Mechanics, G - Reference,Information and Interdisciplinary Subjects Series (University Science Books). https://books.google.com.mx/books?id=P1kCtNr-pJsC

Thompson, A. R., Moran, J. M., & Swenson, George W., J. 2017, Interferometry and Synthesis in Radio Astronomy, 3rd Edition, doi: 10.1007/978-3-319-44431-4

Walborn, N. R. 1973, ApJ, 179, L123, doi: 10.1086/181131

Webster, B. L., & Murdin, P. 1972, , 235, 37, doi: 10.1038/235037a0

Yusef-Zadeh, F., Bushouse, H., Dowell, C. D., et al. 2006, , 644, 198, doi: 10.1086/503287

Zhao, J.-H., Morris, M. R., & Goss, W. M. 2016, The Astrophysical Journal, 817, 171, doi: 10.3847/0004-637X/817/2/171